

กลาสเซรามิกกันรั่วอุณหภูมิสูงจากระบบแก้ว $R_2O-RO-Al_2O_3-SiO_2$

นายอภิรัฐ ธีรภาพพิเศษพงษ์

วิทยานิพนธ์นี้เป็นส่วนหนึ่งของการศึกษาตามหลักสูตรปริญญาวิทยาศาสตรดุษฎีบัณฑิต

สาขาวิชาวัสดุศาสตร์ ภาควิชาวัสดุศาสตร์

คณะวิทยาศาสตร์ จุฬาลงกรณ์มหาวิทยาลัย

ปีการศึกษา 2554

ลิขสิทธิ์ของจุฬาลงกรณ์มหาวิทยาลัย

บทคัดย่อและแฟ้มข้อมูลฉบับเต็มของวิทยานิพนธ์ตั้งแต่ปีการศึกษา 2554 ที่ให้บริการในคลังปัญญาจุฬาฯ (CUIR)

เป็นแฟ้มข้อมูลของนิสิตเจ้าของวิทยานิพนธ์ที่ส่งผ่านทางบัณฑิตวิทยาลัย

The abstract and full text of theses from the academic year 2011 in Chulalongkorn University Intellectual Repository(CUIR)

are the thesis authors' files submitted through the Graduate School.

HIGH TEMPERATURE GLASS CERAMIC SEALANTS FROM R_2O - RO - Al_2O_3 - SiO_2

Mr. Apirat Theerapapvisetpong

A Dissertation Submitted in Partial Fulfillment of the Requirements
for the Degree of Doctor of Philosophy Program in Materials Science

Department of Materials Science

Faculty of Science

Chulalongkorn University

Academic Year 2011

Copyright of Chulalongkorn University

อภิรัฐ ธีรภาพพิเศษพงษ์ : กลาสเซรามิกกันรั่วอุณหภูมิสูงจากระบบแก้ว $R_2O-RO-Al_2O_3-SiO_2$ (HIGH TEMPERATURE GLASS CERAMIC SEALANTS FROM $R_2O-RO-Al_2O_3-SiO_2$)
 อ.ที่ปรึกษาวิทยานิพนธ์หลัก : ผศ.ดร.ศิริฉวี เจียมศิริเลิศ, อ. ที่ปรึกษาวิทยานิพนธ์ร่วม ดร.ปาจริย
 ถาวรนิติ, ศ.ดร. ไนน์ฮาร์ด คอนราดท์ , 131 หน้า.

กลาสเซรามิกกันรั่วที่ปราศจากแบเรียมสำหรับเซลล์เชื้อเพลิงออกไซด์ของแข็งแบบแผ่น จากระบบ $R_2O-RO-Al_2O_3-SiO_2$ ($R=Na, K, Mg, Ca$) ถูกพัฒนาขึ้น และได้ทำการตรวจสอบสมบัติต่างๆ ขึ้นตอนการทดลองแบ่งเป็นสองส่วน ส่วนแรกคือการตรวจสอบลักษณะและทดสอบการยึดติดของกลาสเซรามิกแต่ละสูตรในระบบ $MgO-CaO-Al_2O_3-SiO_2$ โดยแปรปริมาณส่วนผสม Na_2O และ K_2O ตั้งแต่ 0-10 เปอร์เซ็นต์โดยโมล ในส่วนที่สองเป็นการออกแบบส่วนผสมกลาสเซรามิกในระบบ $MgO-CaO-Al_2O_3-SiO_2$ และแปรส่วนผสม B_2O_3 จาก 0-20 เปอร์เซ็นต์โดยน้ำหนัก สูตรแก้วจากทั้งสองส่วนถูกเตรียมโดยการหลอมที่อุณหภูมิ 1450 องศาเซลเซียส และ 1500 องศาเซลเซียสก่อนที่จะทำการตรวจสอบสมบัติทางความร้อน ได้แก่ อุณหภูมิการเปลี่ยนสภาพแก้ว อุณหภูมิการเกิดผลึก อุณหภูมิการอ่อนตัว และ สัมประสิทธิ์การขยายตัวเชิงความร้อน ทำการทดสอบการยึดติดของกลาสเซรามิกและเหล็กกล้าไร้สนิม ได้แก่ AISI430 และ Crofer22 APU ที่อุณหภูมิ 900 องศาเซลเซียส เป็นเวลา 2 ชั่วโมง แล้วผ่านกระบวนการความร้อนที่อุณหภูมิ 800 องศาเซลเซียส เป็นเวลา 100 ชั่วโมง และตรวจสอบด้วย SEM/EDX กลาสเซรามิกที่ผ่านกระบวนการความร้อนเป็นเวลานานถูกตรวจสอบความมีเสถียรภาพด้วยการศึกษาการเปลี่ยนแปลงการเกิดผลึก และการเปลี่ยนแปลงสัมประสิทธิ์การขยายตัวเชิงความร้อน ด้วยเครื่อง XRD และไดลาโทมิเตอร์ ผลการทดลองในส่วนแรกแสดงให้เห็นว่ากลาสเซรามิกที่มีส่วนผสมของ Na_2O และ K_2O สามารถยึดติดกับเหล็กกล้าไร้สนิม AISI430 ได้ หลังจากผ่านกระบวนการความร้อนที่ 900 องศาเซลเซียส เป็นเวลา 2 ชั่วโมง อย่างไรก็ตามไม่สามารถยึดติดกับ YSZ ได้ เนื่องจากค่าสัมประสิทธิ์การขยายตัวเชิงความร้อนของกลาสเซรามิกสูงเกินไป การผ่านกระบวนการความร้อนเป็นเวลานานที่อุณหภูมิ 800 องศาเซลเซียส เป็นสาเหตุให้ค่าสัมประสิทธิ์การขยายตัวเชิงความร้อนสูงขึ้น อันเนื่องมาจากการเกิดผลึก เนฟิไลน์ ($NaAlSi_3O_8$) และ kaliophilite ($KAlSi_3O_8$) ในส่วนที่สองพบว่ากลาสเซรามิกที่สามารถยึดติดได้ดีกับเหล็กกล้าไร้สนิม Crofer22 APU และ YSZ คือสูตรที่มีส่วนผสมของ B_2O_3 5 เปอร์เซ็นต์โดยน้ำหนัก เป็นอย่างน้อย การลดลงของค่าสัมประสิทธิ์การขยายตัวเชิงความร้อนแปรผกผันกับปริมาณ B_2O_3 ในส่วนผสมกลาสเซรามิก ซึ่งมีผลในการเพิ่มการเกิดเฟส ไดออกไซด์ และอะนอร์ไทต์ ที่มีค่าสัมประสิทธิ์การขยายตัวเชิงความร้อนต่ำ

ภาควิชา.....วัสดุศาสตร์..... ลายมือชื่อ.....
 สาขาวิชา.....วัสดุศาสตร์..... ลายมือชื่อ อ.ที่ปรึกษาวิทยานิพนธ์หลัก.....
 ปีการศึกษา.....2554..... ลายมือชื่อ อ.ที่ปรึกษาวิทยานิพนธ์ร่วม.....
 ลายมือชื่อ อ.ที่ปรึกษาวิทยานิพนธ์ร่วม.....

4973897623 : MAJOR MATERIALS SCIENCE

KEY WORD: GLASS / GLASS-CERAMIC / SEALANT / SOFC / FUEL CELL

APIRAT THEERAPAPVISETPONG : HIGH TEMPERATURE GLASS CERAMIC SEALANTS FROM R_2O -RO- Al_2O_3 - SiO_2 . ADVISOR : ASST.PROF.SIRITHAN JIEMSIRILERS, Ph.D., CO-ADVISORS : PAJAREE THAVORNITI, Ph.D., PROF. REINHARD CONRADT, Ph.D., 131 pp.

Barium-free glass-ceramic sealants for the planar solid oxide fuel cell from the system R_2O -RO- Al_2O_3 - SiO_2 (R=Na, K, Mg, Ca) were developed and their properties were investigated. The experimental procedure was divided into two parts. The first part consisted in the characterization and performance of joining tests between glass-ceramics in the system MgO-CaO- Al_2O_3 - SiO_2 with additional amounts of Na_2O and K_2O varying from 0 to 10 mol%. The second part was devoted to glass-ceramics in the system MgO-CaO- Al_2O_3 - SiO_2 with additional amounts of B_2O_3 varying from 0 to 20 wt.%. Both types of glass compositions were prepared by melting at 1450 °C and 1500 °C. Their thermal properties including glass transition temperature, crystallization temperature, dilatometric softening temperature, and coefficient of thermal expansion (CTE) were determined. The joins of glass-ceramics and ferritic stainless steel, including AISI430 and Crofer22 APU, were established at 900 °C, 2 h, thermally treated at 800 °C for 100 h and observed by SEM/EDX. The stability of the glass-ceramics after long term heat treatment was assessed through the crystallization of the mineral phases and the change in CTE using XRD and dilatometry, respectively. The results in the first part showed that glass-ceramics containing Na_2O and K_2O could be joined with AISI430 stainless steel after thermal treatment at 900 °C for 2 h. However, they did not tightly bond to YSZ because their CTEs were too high. Long-time exposure at 800 °C of these glass-ceramics caused a large increase in the CTE, which can be explained by increased formation of nepheline ($NaAlSi_3O_8$) and kaliophilite ($KAlSi_3O_8$). In the second part, good bonding between glass-ceramics and other components including Crofer 22 APU stainless steel and YSZ was found only in case of glass-ceramics containing at least 5 wt.% B_2O_3 . The decrease of CTE is related to the increase of the boron oxide content in glass-ceramics, which leads to an increase in the formation of low-CTE phases diopside and anorthite.

Department : Materials Science

Student's Signature

Field of Study : Materials Science

Advisor's Signature

Academic Year : 2011

Co-advisor's Signature

Co-advisor's Signature

ACKNOWLEDGEMENTS

I could not have reached to this education point without the encouragement of many persons who have given me assistance, and guidance during study and research period whom I would like to express my gratitude and thanks.

Firstly, I would like to thank my thesis advisor, Asst.Prof.Dr. Sirithan Jiemsirilers, who has kindly given me opportunity and inspiration to study for Ph.D. course and supported all research necessities. Next, I wish to thank Dr. Pajaree Thavorniti, who has recommended me for a Ph.D. scholarship from NSTDA, and given me the constant guidance. I would like to acknowledge Prof.Dr. Reinhard Conrardt, who has kindly given me very useful suggestion and valuable opportunity to use necessary research facilities in his laboratory at the Institut für Gesteinshüttenkunde (GHI), RWTH Aachen, Germany.

I would like to acknowledge the Thailand Graduate Institute of Science and Technology (TGIST) Program, NSTDA, for granting me a Ph.D. scholarship. I also would like to gratefully acknowledge the German Academic Exchange Service (DAAD) for short term research grant in GHI, RWTH Aachen, Germany. I am gratefully to this scholarship, which made it possible for me to fulfill my research work.

I would like to thank Dr. Sumittra Charojrochkul and her assistants for their suggestion and help in gas leak testing at the National Metal and Materials Technology Center (MTEC).

I would like to extend my sincerest thank to my friends at GHI, Mr. Widiya jatmiko, Ms. Anna Kasper, Ms. Tanja Mund, Ms. Beatriz Cela, Mr. Supoj Silpawattana, and other people, who kindly assisted me with warmly welcome during my research at GHI.

I would like to thank all my colleagues and staff members in the Department of Materials Science, Chulalongkorn University for their friendship and mind fullness and I am happy to be among them.

Finally, I wish to dedicate this thesis to my parents, who have given me the lasting encouragement and support to make this thesis possible.

CONTENTS

	Page
ABSTRACT (THAI)	iv
ABSTRACT (ENGLISH)	v
ACKNOWLEDGMENTS.....	vi
CONTENTS.....	vii
LIST OF TABLES.....	xi
LIST OF FIGURES.....	xiii
CHAPTER 1 INTRODUCTION.....	1
CHAPTER 2 LITERATURE REVIEW.....	3
2.1 Solid oxide fuel cells.....	3
2.2 Current materials in SOFC.....	5
2.2.1. Anode.....	5
2.2.2. Electrolyte.....	5
2.2.3. Cathode.....	6
2.2.4. Interconnect	6
2.2.5. Sealant for planar SOFC.....	7
2.3 Glass and glass-ceramic sealant for pSOFC	9
2.4 Literature survey of recently developed glass-ceramics sealant	12
2.5 Effect of glass composition on properties of glass and glass-ceramic sealants	17
2.5.1. Thermal expansion.....	17
2.5.2. Chemical stability	18
2.5.2.1. Chemical stability of bulk glass	19

2.5.2.2. Chemical stability of interface.....	20
2.5.3. Mechanical properties.....	21
2.5.3.1. Bonding strength.....	21
2.5.3.2. Thermal cycling stability.....	21
2.5.3.3. Sealing ability.....	22
2.5.4. Electrical resistivity.....	23
CHAPTER 3 EXPERIMENTAL PROCEDURE.....	25
3.1 Part I: Development of glass-ceramics seal in a system of R_2O [R = Na, K]– MgO–CaO–Al ₂ O ₃ –SiO ₂	26
3.1.1. Glass formula selection.....	26
3.1.2. Glass preparation.....	28
3.1.3. Determination of glass transition temperature and crystallization temperature.....	28
3.1.4. Microstructure and crystallization observation.....	30
3.1.5. Dilatometric measurement.....	30
3.1.6. Joining test.....	31
3.1.7. Electrical resistivity measurement.....	31
3.2 Part II: Development of glass-ceramics seal in system MgO–CaO–B ₂ O ₃ – Al ₂ O ₃ –SiO ₂	32
3.2.1. Glass formula selection.....	32
3.2.2. Glass preparation.....	36
3.2.3. DTA and dilatometric measurement of glass and glass - ceramics....	37
3.2.4. Hot - stage microscopy experiment.....	38
3.2.5. Joining test.....	39

	Page
3.2.6. Thermal cycle and leak test	40
3.2.7. Electrical resistivity measurement	41
CHAPTER 4 RESULTS AND DISCUSSION	42
4.1 Part I: Development of glass-ceramics sealant in system R_2O -MgO-CaO- Al_2O_3 - Si_2O	42
4.1.1. Glass selection	42
4.1.2. Preparation of glasses in CM1 and CM2 series	48
4.1.3. Thermal properties of glass and glass-ceramics in CM1 and CM2 series	49
4.1.4. Dilatometric result and crystallization behavior of heat treated glass- ceramics in CM1 and CM2 series	52
4.1.4.1. Dilatometric result of glass-ceramics after heat treatments	52
4.1.4.2. Crystallization Behavior	55
4.1.5. Electrical properties	56
4.1.6. Joining test between glass-ceramics and AISI430 stainless steel	62
4.1.7. Joining test between glass-ceramics and YSZ ceramic	67
4.2 Part II: Development of glass-ceramics seal in system MgO-CaO- B_2O_3 - Al_2O_3 - SiO_2	69
4.2.1. Glass selection and preparation	69
4.2.2. Thermal properties of glass 34, 35 and 37 series	70
4.2.1. Hot-stage microscope	73
4.2.2. Joining test between glass-ceramics/ Crofer 22 APU stainless steel and glass-ceramics/YSZ ceramics	78

4.2.2.1. Joining test between glass–ceramics and Crofer22 APU stainless steel	78
4.2.2.2. Joining test between glass–ceramics and YSZ ceramic	82
4.2.3. Thermal cycle and leak test	86
4.2.4. Crystallization behavior and thermal expansion stability.....	88
4.2.5. Electrical resistivity of glass- ceramics in 34 and 35 series	93
CHAPTER 5 CONCLUSION AND FUTURE WORK	96
5.1 Conclusion.....	96
5.2 Future work.....	97
REFERENCES	98
APPENDICES.....	111
APPENDIX A.....	112
APPENDIX B.....	113
APPENDIX C	117
APPENDIX D	118
APPENDIX E.....	119
BIOGRAPHY	131

LIST OF TABLES

	Page
Table 2.1 Composition of metallic alloy interconnects for SOFC.....	7
Table 2.2 Function of different oxide constituents in a seal glass	12
Table 2.3 Developed glass compositions for SOFC sealants from many authors.....	14
Table 2.4 Selected properties of some glass composition for SOFC sealants.....	16
Table 2.5 CTE of crystalline phases in glass-ceramics sealants.....	18
Table 3.1 Starting glass compositions	26
Table 3.2 Crystalline phases and CTEs of glass compositions and constitutional compound calculation (CIPW norm) of glass-ceramics.	27
Table 3.3 List of glass compositions	28
Table 3.4 Designed glass compositions	33
Table 3.5 Constitutional Compound Calculations (CIPW norm), and FactSage calculations of glass designed glass composition	34
Table 3.6 Glass compositions in system Mg–Ca–B ₂ O ₃ – Al ₂ O ₃ –SiO ₂	36
Table 4.1 Constitutional compound calculation of selected glass composition.....	44
Table 4.2 Differential thermal analysis of as–melted glasses.....	47
Table 4.3 Detected crystalline phases in glass–ceramics after sintered at 900 °C, 2 h, obtained by XRD.	47
Table 4.4 Thermal expansion of sintered glass at 900 °C for 2 h using dilatometer comparison of AISI430 stainless steel.....	48
Table 4.5 Particle size distribution of glass powder	48
Table 4.6 Thermal properties including T _g , T _c , T _d (°C) and CTE (x10 ⁻⁶ K ⁻¹) of bulk glass and glass-ceramics (after sintered at 900 °C, 2h) in CM1 and CM2 series.	49

Table 4.7	CTE of glass and heat treated glass–ceramics with different condition ($\times 10^{-6} \text{ K}^{-1}$, range 100 – 600 °C)	53
Table 4.8	Crystalline phases of glass–ceramics after sintered at 900°C for 2 h obtained by XRD pattern	55
Table 4.9	Electrical resistivity of glass–ceramics at 600–800 °C.....	59
Table 4.10	Activation energy of glass-ceramics at temperature 600 – 800 °C	60
Table 4.11	Joining test between glass–ceramics and AISI430 stainless steel at 900 °C, 2 h compare with CTE of glass and glass–ceramics.....	63
Table 4.12	Particle size distribution of glass powders for properties characterization and joining test	70
Table 4.13	T_g , T_c and crystallization peak temperature (T_p) obtained by DTA.....	71
Table 4.14	Thermal parameters obtained by hot stage microscope (temperature in °C) and calculated constants A B and T_0 in VFT equations.....	74
Table 4.15	Joining test results compare with the CTE of glass ceramics.	79
Table 4.16	Leak rate of sandwich sample of Crofer 22 APU/glass-ceramics/ Crofer22 APU after thermal cycle test ($\text{cm}^3 \cdot \text{min}^{-1} \cdot \text{cm}^{-1}$)	87
Table 4.17	Crystalline phases found in glass-ceramics after heat treated at 900 °C, 2 h obtained by XRD	89
Table 4.18	CTE of glass-ceramics after heat treated at 900 °C, 2 h and continue heat treated at 800 °C, 100 h	91
Table 4.19	Electrical resistivity of glass-ceramics at 800 °C	93

LIST OF FIGURES

	Page
Fig. 2.1 Schematic of electrochemical energy conversion to electricity in a SOFC device.....	4
Fig. 2.2 Schematic of (a) tubular, (b) flat planar, (c) monolithic and (d) Serial configuration of solid oxide fuel cells	4
Fig. 2.3 Schematic of edge seal of pSOFC	8
Fig. 2.4 Glass network structure.....	11
Fig. 3.1 Glass transition region measured temperatures.....	29
Fig. 3.2 T_g and T_c determined using computer software.	30
Fig. 3.3 Experimental setup of impedance analysis.....	32
Fig. 3.4 Phase diagram (Acer. Fig. 5473-A) with positions of glass 31 - 37 compositions	34
Fig. 3.5 Equilibrium plot of Constitutional Compounds of glass 31 - 37 calculated by FactSage	35
Fig. 3.6 Equilibrium plot of Constitutional Compounds of glass 31 composition calculated by FactSage.....	35
Fig. 3.7 Flow chart of overall experimental procedure in part II from starting glass powders	37
Fig. 3.8 Hot - stage microscopy experimental setup.....	39
Fig. 3.9 Illustration of (a) test sample assemble of glass-ceramics (GC) sealant and Crofer 22 APU stainless steel plates, (b) gas leak test experimental setup.....	41
Fig. 4.1 As-melted glass from different crucible and temperature	43
Fig. 4.2 As-melted glass after melted at 1500 °C, 2 h in platinum crucible.....	45

Fig. 4.3	X-ray diffraction pattern of containing crystalline phase glass piece S1	45
Fig. 4.4	X-ray diffraction pattern of containing crystalline phase glass piece S2	46
Fig. 4.5	X-ray diffraction pattern of containing crystalline phase glass piece S3	46
Fig. 4.6	Dilatometric curves of glasses in CM1 and CM2 series	49
Fig. 4.7	Comparison of T_g and T_d of bulk glass CM1 obtained by dilatometer	50
Fig. 4.8	Comparison of T_g and T_d of bulk glass CM2 obtained by dilatometer	50
Fig. 4.9	Comparison of CTE of bulk glass CM1 obtained by dilatometer	51
Fig. 4.10	Comparison of CTE of bulk glass CM2 obtained by dilatometer	52
Fig. 4.11	Comparison of dilatometric curves of glass and glass-ceramics with different heat treatment condition	54
Fig. 4.12	Impedance spectra , in Nyquist diagram form, of all glass-ceramics in CM1 series at different temperature.	57
Fig. 4.13	Impedance spectra, in Nyquist diagram form, of glass-ceramics in CM2 series at different temperature.	58
Fig. 4.14	Arrhenius plots of log resistivity vs. $1000/T$ of glass-ceramics in CM1 series at temperature between 600–800 °C.	59
Fig. 4.15	Arrhenius plots of log resistivity vs. $1000/T$ of glass-ceramics in CM2 series at temperature between 600–800 °C.	60
Fig. 4.16	XRD-patterns of glass-ceramics after heat treated by different condition	61
Fig. 4.17	Cross section of glass-ceramics and AISI430 stainless steel after joining at 900 °C, 2 h	64
Fig. 4.18	EDX line scan across interface between CM13 glass-ceramics and AISI430 stainless steel	64

Fig. 4.19 EDX line scan across interface between CM14 glass–ceramics and AISI430 stainless steel.....	65
Fig. 4.20 EDX line scan across interface between CM22 glass–ceramics and AISI430 stainless steel.....	65
Fig. 4.21 EDX line scan across interface between CM23 glass–ceramics and AISI430 stainless steel.....	66
Fig. 4.22 EDX line scan across interface between CM24 glass–ceramics and AISI430 stainless steel.....	66
Fig. 4.23 Comparison of dilatometric curves of selected bulk glass, glass–ceramics, AISI430 SS and YSZ ceramics	68
Fig. 4.24 Cross section of Glass–ceramics and YSZ ceramic after heat treated at 900 °C, 2 h.....	69
Fig. 4.25 DTA curves of glass 34 series	71
Fig. 4.26 DTA curves of glass 35 series	72
Fig. 4.27 DTA curves of glass 37 series	73
Fig. 4.28 (a) Variation in area and height of powder sample of 34 – 10B during hot stage microscope measurement (b) Geometric shapes of the sample associated to (a).....	75
Fig. 4.29 Plot of viscosity data of glass 34 series obtained from hot-stage microscope compared with viscometer curves calculated from VFT equation (solid line)	76
Fig. 4.30 Plot of viscosity data of glass 35 series obtained from hot-stage microscope compared with viscometer curves calculated from VFT equation (solid line)	77

Fig. 4.31 Plot of viscosity data of glass 37 series obtained from hot-stage microscope compared with viscometer curves calculated from VFT equation (solid line) .	78
Fig. 4.32 SEM and EDX mapping of cross-section pictures of joined glass-ceramics in 34 series and Crofer 22 APU at 900 °C, 2 h and dwelling at 800 h,100 h.....	80
Fig. 4.33 SEM and EDX mapping of cross-section pictures of joined glass-ceramics in 35 series and Crofer 22 APU at 900 °C, 2 h and dwelling at 800 h,100 h.....	81
Fig. 4.34 SEM and EDX mapping of cross-section pictures of joined glass-ceramics in 37 series and Crofer 22 APU at 900 °C, 2 h and dwelling at 800 h,100 h.....	82
Fig. 4.35 SEM of cross-section pictures of joined glass-ceramics in 34 series and YSZ ceramics.....	83
Fig. 4.36 SEM/EDS quantitative results of glass-ceramics 34-15B joined with YSZ	84
Fig. 4.37 SEM/EDS quantitative results of glass-ceramics 34-20B joined with YSZ	84
Fig. 4.38 SEM of cross-section pictures of joined glass-ceramics in 35 series and YSZ ceramics.....	85
Fig. 4.39 SEM of cross-section pictures of joined glass-ceramics in 37 series and YSZ ceramics.....	86
Fig. 4.40 Comparison of leak rate of Crofer 22 APU stainless steel and glass-ceramic sealant after each thermal cycle (800 °C, 12 h)	88
Fig. 4.41 XRD-patterns of glass-ceramics 34, 35 and 37 after heat treated at 900 °C, 2 h	89
Fig. 4.42 XRD-patterns of glass-ceramics 34 series after heat treated at 900 °C, 2 h and continue heat treated at 800 °C, 100 h.....	90
Fig. 4.43 XRD-patterns of glass-ceramics 35 series after heat treated at 900 °C, 2 h and continue heat treated at 800 °C, 100 h.....	90

Fig. 4.44 Dilatometric curve of glass-ceramics 34 and 35 series after heat treated at 900 °C for 2 h and continue heat treated at 800 °C for 2h.....	92
Fig. 4.45 Impedance spectra, in Nyquist diagram form, of glass-ceramics in 34 series at 800 °C	94
Fig. 4.46 Impedance spectra, in Nyquist diagram form, of glass-ceramics in 35 series at 800 °C	95

CHAPTER 1

INTRODUCTION

At present, crude oil price is climbing up by increasing of demand, while its resources are declining to empty within this century. Many candidate energy resources are being researched and evaluated their efficiency to use as reliable and inexpensive resources. One of them is planar designed solid oxide fuel cells (pSOFC), which is the best design generating high electric power with cost efficiently among other designs.

Solid oxide fuel cell (SOFC) is a device for the electrochemical production of electricity from fuel gas and air at high temperatures, 750 °C - 1000 °C, in moderate to high levels of moisture environment. This environment is the reason of many problems for component materials especially interconnect (or bipolar) plate and sealant in planar stack of pSOFC. A gas leak can happen if the component part damages during operation. It leads to decrease of performance and low power generation. This leak is also the reason of local hot spots and internal combustions inside the stack. The device, consequently, is rapidly degraded and broken [1-2].

In order to select the proper seal materials for pSOFC, glass [3-6] and glass-ceramics [7-10] are good candidate materials when their coefficients of thermal expansion (CTE) matches to the adjoining components (typically should be in the range of $9-13 \times 10^{-6} \text{ K}^{-1}$). Nevertheless, they are brittleness materials and rigid bonding to the metallic interconnects in pSOFC. Compressive sealants are the other types of the sealant materials were developed. For example, metallic gaskets [11] and mica [12] are more flexible and higher to thermal shock resistance. Unfortunately, the compressive sealants are harmed by deformation at every loading, and a very high loading pressure is needed to inhibit high leak rates, which leads to damage the cells.

In efforts to develop glass-ceramics sealants for SOFCs, many glass systems have been studied, such as alkali and alkaline-earth silicates, aluminosilicate, borosilicate, and aluminophosphate glasses [9, 13]. A number of potential problems, which are coefficient of thermal expansion mismatch, poor thermo chemical stability,

and worsen interfacial reactions with other cell components, have been considered for designing a suitable sealing system. For example, the formation of a BaCrO_4 reaction product at the interface between barium-containing glass-ceramic sealants and Cr-steel interconnects (such as Crofer 22 and AISI 430 stainless steel) decreases the long-term mechanical stability of the sealant [6].

Most of the invention of glass and glass-ceramic sealants contained B_2O_3 . Boron oxide is interesting due to its suitable effect on the viscosity of glass, which is important for the joining process. In contrast, the volatilization of boron-containing species restricts its application as a main component for SOFC sealing applications. Such as, glasses with B_2O_3 as the only glass former experienced up to a 20% weight loss and extensive interaction with SOFC components, in both air and fuel gas atmospheres [14-15].

In this work, barium free compositions were designed and prepared from base glasses in a system of $\text{R}_2\text{O}-\text{CaO}-\text{MgO}-\text{Al}_2\text{O}_3-\text{SiO}_2$ ($\text{R}=\text{Na}, \text{K}$) and non alkali system of $\text{CaO}-\text{MgO}-\text{B}_2\text{O}_3-\text{Al}_2\text{O}_3-\text{SiO}_2$. The primary requirements of pSOFC's glass-ceramic sealant were investigated which is T_g , T_c , coefficient of thermal expansion and joining ability with AISI 430 stainless steel. The Na_2O , K_2O and B_2O_3 components were varied in the compositions, measured their thermal properties and investigated phase transformation in glass-ceramic sealants after thermal treatment at joining temperature, 900 °C and working temperature of pSOFC, 800 °C.

The objectives of this study are described as follows;

- To develop the suitable glass and glass-ceramic composition for planar solid oxide fuel cell sealant application
- To study the capability of the developed sealants to seal metal to metal, metal to ceramic and ceramic to ceramic application.

CHAPTER 2

LITERATURE REVIEW

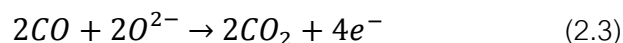
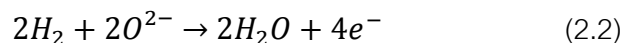
2.1 Solid oxide fuel cells

A solid oxide fuel cell (SOFC) is one type of fuel cell device. The principle compositions of this device are composed of porous electrodes, which are cathode and anode, interpolated by an electrolyte made of solid oxide ceramic. The system was originally proposed by Nernst in 19th century [16]. Bauer and Preis proposed their first ceramic fuel cell working at 1000 °C called "Nernst Mass" 85% ZrO₂ and 15% Y₂O₃ and other ZrO₂ based ceramics with a proper ionic conductivity at temperature 600-1000 °C [17]. In basic function of SOFC, the electrical energy is obtained as a product from reaction between oxygen and a fuel gas through a ceramic electrolyte membrane as illustrated in Fig. 2.1.

At cathode, the reaction of oxygen gas, O₂ from air with porous cathode layer (Sr_x La_{1-x} MnO_{3-δ}) occurs via



Only O²⁻ ions could migrate through dense solid oxide electrolyte layer (8 mol% Y₂O₃ – ZrO₂, YSZ) and react with hydrogen gas, H₂ or carbon monoxide, CO from fuel gas at anode layer (Ni-YSZ cermet). The electrons are released from anode, and an electric current was generated through external electric circuit to cathode side. The reaction products are also water H₂O and/or carbon dioxide CO₂ depend on input fuel gas from equations below:



The overall reaction from (2.1) and (2.2) is:



and (2.1) and (2.3) is:

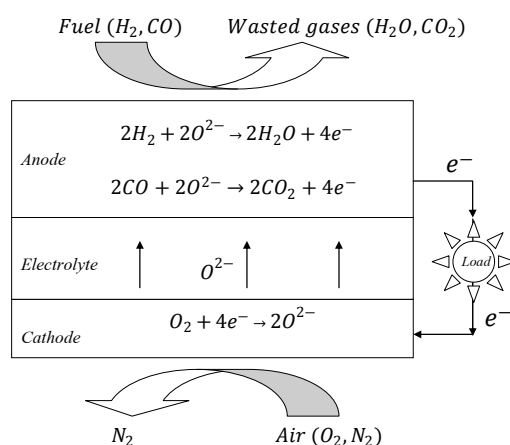


Fig. 2.1 Schematic of electrochemical energy conversion to electricity in a SOFC device

There are three major developed designs of SOFC, which are flat-plate type cells, tubular and monolithic [18]. In general, the planar stack concept (pSOFC) is attractive among the SOFC designs because it can be produced in compact size with high volumetric power density, and utilized in transportation applications.

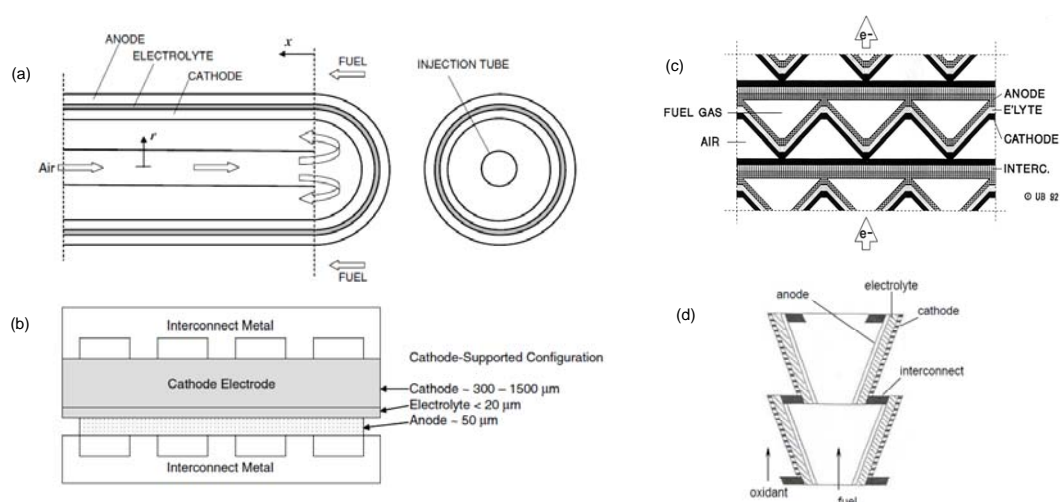


Fig. 2.2 Schematic of (a) tubular, (b) flat planar, (c) monolithic and (d) Serial configuration of solid oxide fuel cells [18-19]

2.2 Current materials in SOFC

2.2.1. Anode

Early development of SOFCs, precious metals like platinum and gold were used as anode, due to their stability. Currently, Ni/8YSZ (Ni with 8 mol% of YSZ) is widely used because it can provide high electrical conductivity and competent ionic conductivity and high activity for electrochemical reactions and reforming. Furthermore, itself mechanical strength is high enough to support structure of entire cell as “anode support”[20-21]. It prepared from 30 vol% nickel oxide powder and YSZ powder followed by sintering at 1300 °C to obtain a porous anode layer in reduction hydrogen gas. The expansion coefficient of this “nickel cermet” anode is about $12.5 \times 10^{-6} \text{ K}^{-1}$.

2.2.2. Electrolyte

Yttria-stabilized zirconia (YSZ) is currently employed materials to be utilized as electrolyte. Brown Boveri [22] and Westing house [23], in Germany and United State respectively, have proved that YSZ electrolyte gives the SOFC to reach high power density. YSZ has a good ionic conductivity and slight electronic conductivity at temperature above 700 °C. Although, many production companies, such as Siemens-Westinghouse and Mitsubishi Heavy Industries-Chubu Electric Power Company keep the operation temperature of their system at 1000 °C, many scientists have tried to find the other way to reduce working temperature to below 800 °C [18-20, 24], however, only Minh [19] is acceptable. The advantages of lower operating temperature are mainly connected to inexpensive metallic interconnects, such as ferritic stainless steel, instead of expensive ceramic interconnects. The other reasons are about chemical stability and reduced the thermal expansion mismatch components. ZrO_2 doped with 8 mol% Y_2O_3 is general used as the electrolyte with CTE of $10.8 \times 10^{-6} \text{ K}^{-1}$.

Furthermore, new materials with higher oxygen ion conductivity were developed and reported, for example gadolinium and Samaria doped ceria (GDC

and SDC) and LaGaO_3 (in particular the lanthanum gallate with the strontium doping on the A site of the perovskite and magnesium on the B-site (LSGM), (LSGM) [25].

2.2.3. Cathode

Because of operating in a highly oxidizing environment, it is unable to use metals, and precious metals because of their cost prohibitive. Porous layer of strontium doped LaMnO_3 (LSM) is widely used as cathode as $\text{Sr}_x \text{La}_{1-x} \text{MnO}_{3-\delta}$. LSM performs a good electrochemical activity for oxygen reduction, a good stability at working temperature around 1000 °C and its CTE is close to YSZ about $11.2 \times 10^{-6} \text{ K}^{-1}$.

Some other materials are also being considered such as $\text{La}_{1-x} \text{Sr}_x \text{FeO}_{3-\delta}$ (LSF) and $\text{La}_{1-x} \text{Sr}_x \text{Co}_y \text{FeO}_{3-\delta}$ (LSCF). They show much better ionic conductivity than LSM. However some problems related to the compatibility with YSZ can arise, the use of these materials with alternative electrolyte materials is being investigated [26-28].

2.2.4. Interconnect

Interconnect materials for SOFC are divided into two types depend on working temperature of SOFC. The first one is ceramic interconnect, which is able to work at high temperature. The second one is metallic alloy interconnect, which is cheaper and work at lower temperature for intermediate temperature SOFC. Ceramic interconnects are made of doped lanthanum and yttrium chromites, which perform high electrical conductivity at high temperature, while their conductivity decrease at lower temperature [19, 29-31]. Various inexpensive metals commonly employed to replace the ceramic interconnects working at lower working temperature SOFC, which include various austenitic and ferritic stainless steels such as AISI430, Crofer22 APU. The Ni-based superalloys also included. The developed metal alloy interconnects in recently works are summarized in Table 2.1.

Table 2.1 Composition of metallic alloy interconnects for SOFC

Alloy	Element (mass%)														
	Fe	Ni	Cr	Co	Ti/Zr	Al	Nb/Ta	Mo	Cu	Si	Mn	C	P	Y/La	Others
Crofer22	B/L	-	20-24	-	0.03-0.2	0.12	-	-	0.5	0.5	0.3-	0.03	0.05	0.04-	-
APU											0.8			0.2	
AISI430	B/L	0.75	16-18	-	-	-	-	-	-	0.75	1	0.12	-	-	-
JS-3	B/L	-	23.1	-	0.05	0.01	-	-	-	0.01	0.39	0.007	-	0.09	-
AISI446	B/L	-	25	-	-	-	-	-	-	1	1.5	0.2	0.04	-	0.25N, 0.03S
AISI441	80.68	0.2	17.6	-	0.18	0.045	0.46	-	-	0.47	0.33	0.01	0.024	-	0.001S
AISI1040	B/L	-	0.028	-	-	-	-	0.019	-	0.2	0.74	0.41	0.024	-	0.032S, 0.001V
Fecralloy	B/L	-	22	-	0.1	5	-	-	-	-	-	-	-	0.1	-
Nicrofer 6025HT	9.5	B/L	25	-	-	-	-	-	-	0.5	0.1	0.2	-	-	2.1B
Ferritic T1	B/L	0.2	22.6	-	0.06	0.1	-	-	-	0.1	0.4	-	-	0.1	-
Hastelloy- XR	17.8	49.5	22	-	-	-	-	8.7	-	0.33	0.88	-	-	-	-
Nimonic	1	B/L	19-22	-	0.15- 0.35	0.15	-	-	0.07	0.8	0.7	0.12	0.015	-	0.10S
AE435															
E-brite	B/L	-	26.5	-	-	-	-	1	-	-	-	-	-	-	-
TIMETAL 834	-	-	-	-	3.5Zr	5.8	0.7	0.5	-	0.35	-	0.06	-	-	4Sn
					B/L Ti										

Note: B/L is remaining balance to 100%

2.2.5. Sealant for planar SOFC

Sealant is necessary part for planar design SOFC as shown in Fig. 2.3. There are various types of developed seal for pSOFC. They can be classified into rigid bonded seals, compressive seals, and compliant bonded seals [2].

Rigid bonded sealant is a sealant which is non-deformable at room temperature. It is a brittle joint, therefore, it is susceptible to fracture by tensile stresses during thermal change or thermal expansion mismatches between the sealant and adjacent components. Consequently the requirement of the sealant is that its CTE must be matched with each other joining components. The materials used in this group are glasses and glass-ceramics.

Compressive sealants are made of deformable materials that do not bond to the pSOFC components. They are applied as gaskets sealing under compressive load of entire stack. The sealing surfaces can slide pass one another without a disruption in hermeticity and each stack components are free to expand during thermal change. It is not necessary to consider CTE matching, however, a load frame is required to maintain the desired level of compression on the stack over the entire period of operation. The load frame introduces many problems in stack, including oxidation of the frame material, relaxation of load by creep and increase cost to maintenance the SOFC. The success compressive seal materials are mica-base sealants because they have internal slippage planes and more oxidation resistant than metal powder. However, the leak problem from interface reactions and crystallization still presents [32].

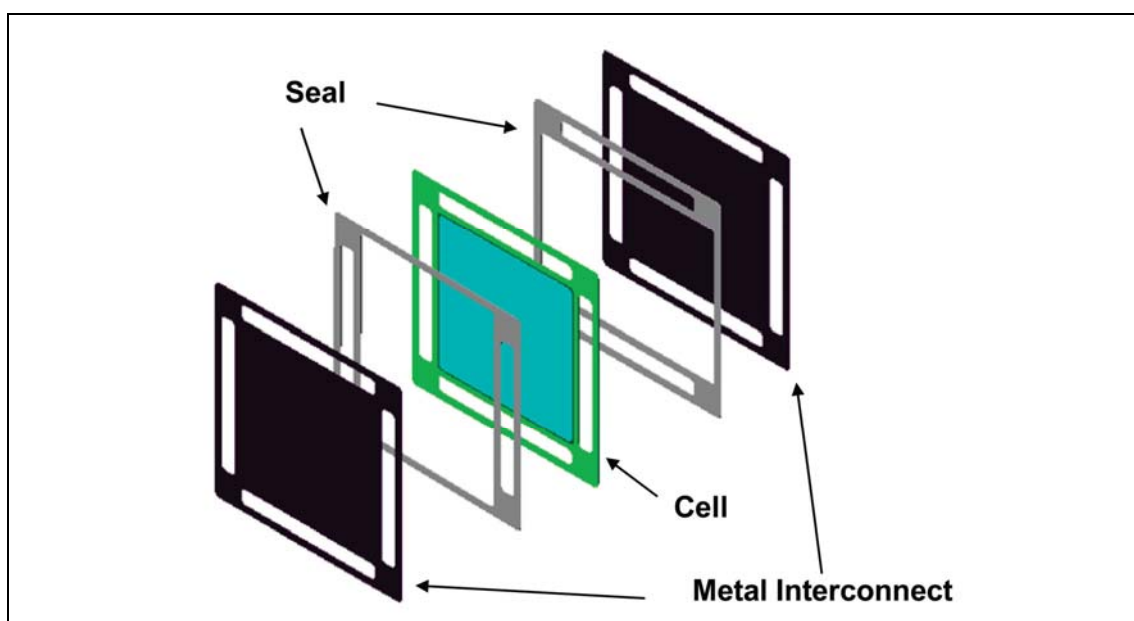


Fig. 2.3 Schematic of edge seal of pSOFC [2]

The compliant bonded sealant is unlike rigid bonded sealing, which can be deformed even at room temperature. This reduces the effect of CTE mismatch to some degree. However, there are still potential problem with cell deforming and non-uniformities in gas distribution. Furthermore, all sealant concepts in this group are metal-base and electrical conductive materials. Therefore, they cannot use directly as single sealant between cell and interconnect in pSOFC without insulating layer to prevent

internal shorting. They may be used combining with a second sealing such as glass sealant in a multi-seal stack design.

2.3 Glass and glass-ceramic sealant for pSOFC

Glass and glass-ceramic are one of the first materials, which utilized as pSOFC sealant materials. They are still most important sealants among the other types of developing sealants because they have stability in both reducing and oxidizing environment of the SOFC stack. In addition, they are inexpensive and can be easily applied to the sealing surfaces as a powder pasts or casted tape, perform good wetting on both surface of YSZ and metal interconnect such as stainless steel, are high electrical resistant, and can be tailored CTE matching to adjacent pSOFC components.

The general requirements of glass and glass-ceramic properties are listed as followed [10, 33-36]:

- Thermal properties: CTE between $9 - 13 \times 10^{-6} \text{ K}^{-1}$. It should be stable for 5,000 h for mobile application and for 50,000 h for stationary application at 650-900 °C operating temperature.
- Chemical properties: resistant to vaporization and compositional change in severe oxidizing and wet reducing environments at 650-900 °C.
- Electrical properties: electrical resistivity $> 1 \times 10^4 \Omega \cdot \text{cm}$
- Viscosity: viscosity should be between 10^6 - 10^9 dPas at sealing temperature and $\geq 10^9$ at working temperature.
- Mechanical properties: resist to external static and dynamic forces during transportation and operation. Resist to thermal cycling failure during start-up and shut-down of cell stacks
- Seal ability: sealing load < 35 kPa. Withstand differential pressure up to 14-35 KPa across a cell stack, total fuel leakage $< 1\%$ for the duration of the cell life.
- Fabrication flexibility: flexible design, low cost and high reliability.

In general, glass sealant compositions are designed to soften and flow at the temperature above working temperature in order to reach a hermetic seal. At working

temperature and long period of operation time, the glass fully crystallized to form a rigid bonded seal. The crystallization in glass is advantageous for many reasons, such as the crystallized glass is typically stronger than starting glassy phase, and it is possible to tailor their CTE by controlling the crystallization kinetics and the crystalline phase. Various glass-forming systems were considered as pSOFC sealants, which based on phosphates, borates, and silicate. However phosphate and borate glass are not stable in humidified environment of SOFC, since they can react with cell components by formation of volatile species [37-38]. At present, many researchers reported their best developed glass and glass-ceramic sealants have been based on silica with various type of modifiers to increase CTE and improve adhesion and joining properties. In order to developed glass and glass-ceramic sealants, there are important properties to consider, which are glass transition temperature (T_g), glass softening temperature (T_d), thermal expansion coefficient (CTE) and thermal stability. At first the basic theory of glass structure and their function of composition are considered in the following paragraph.

Glass structure is composed of three major components, which are network formers, network modifiers, and intermediate oxides. In addition, it may be included additive as a minor component. The glass structure includes all components is shown in Fig. 2.4. SiO_2 and B_2O_3 are commonly employed as glass former in developed glass and glass-ceramic sealants for SOFC. The cations from network formers (Si and B ion) act as the centers of polyhedral units, including tetrahedra and triangles. The network modifiers are commonly alkali oxides, for example, Li_2O , Na_2O , K_2O , etc, and alkaline earth, for example, MgO , CaO , BaO , SrO etc. Network modifiers occupy random positions between the polyhedra and give additional oxygen ions to modify the network structure, neutralize local charge, and glass properties. The intermediate oxides are Al_2O_3 and Ga_2O_3 , which their cations have higher valance and lower coordination number compare to network formers. They can or cannot participate in glass network; therefore, they could be act as glass former if they participate in a glass network and as a glass modifier if not. The additives are used to tailor the properties for sealant, but in some

cases, they are not necessary. Some examples of additives in glass and glass-ceramic sealants are rare earth metal oxides, such as La_2O_3 and Nd_2O_3 , and transition metal oxides, such as TiO_2 , ZnO , and Y_2O_3 . Some additives are called or referred to as nucleating agents, which can influence crystallization in glass (devitrification), such as ZnO , NiO , TiO_2 , Cr_2O_3 , and ZrO_2 . The oxygen ion link to the polyhedral unit are called bridging oxygen, but if this ion does not link to the polyhedral unit, it is referred to as or called non-bridging oxygen. The modifiers and additives play a role in creating non-bridging oxygen species to balance charge neutrality in a glass structure. The functions of different oxide components in glass structure are shown in Table 2.2.

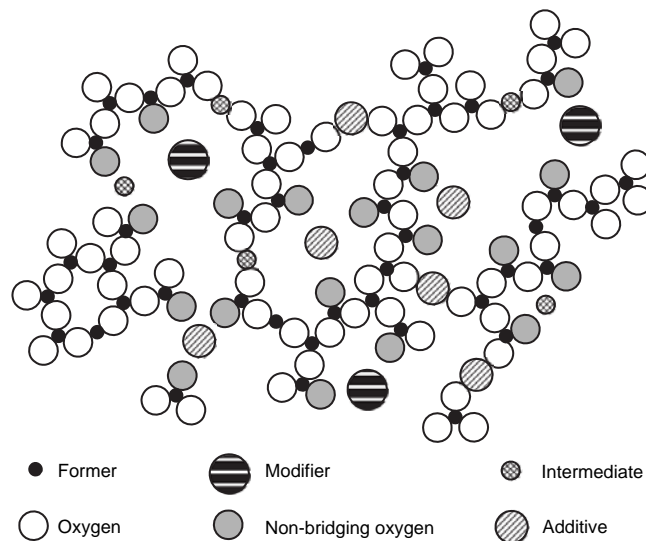


Fig. 2.4 Glass network structure [33]

Table 2.2 Function of different oxide constituents in a seal glass [2, 33, 39]

Glass constituent	Oxide	Function
Network former	$\text{SiO}_2, \text{B}_2\text{O}_3$	Form glass network
		Determine T_g and T_d
		Determine CTE
		Determine adhesion/wetting with other SOFC components
Network modifier	$\text{Li}_2\text{O}, \text{Na}_2\text{O}, \text{K}_2\text{O}$	Create non-bridging oxygen species
	$\text{BaO}, \text{SrO}, \text{CaO}, \text{MgO}$	Modify glass properties such as T_g, T_d , and CTE
Intermediate	$\text{Al}_2\text{O}_3, \text{Ga}_2\text{O}_3$	Hinder devitrification
		Modify glass viscosity
Additive	$\text{La}_2\text{O}_3, \text{Nd}_2\text{O}_3, \text{Y}_2\text{O}_3$	Modify glass viscosity
	ZnO, PbO	Increase CTE
	$\text{NiO}, \text{CuO}, \text{CoO}, \text{MnO}$	Improve glass flow ability
	$\text{Cr}_2\text{O}_3, \text{V}_2\text{O}_5$	Improve seal glass adhesion to other cell components
	$\text{TiO}_2, \text{ZrO}_2$	Induce devitrification

2.4 Literature survey of recently developed glass-ceramics sealant

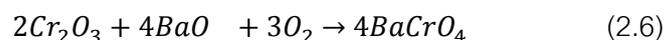
In recent years, there are abundant of glass and glass-ceramic sealants for pSOFC. There are many review papers such as Steele and Heinzl [40], Fergus[41], Reis and Brow [42], Lessing [8], Singh [43], Kilner et al. [44], Mahapatra and Lu [33], and recently by Donald et al.[45]. The glass compositions are summarized in Table 2.3 and selected properties are shown in Table 2.4. The investigated sealants could be classified glass compositions into following groups:

- Alkaline earth silicate
- Alkali alkaline earth silicate
- Alkaline earth borosilicate
- Alkaline earth borate

All glasses and glass-ceramics for pSOFC sealant application have been investigated for joining with metal interconnects at temperature 900 °C and working temperature of pSOFC is below 800 °C. The metals interconnect are austenitic and ferritic stainless steel as reviewed in section 2.2.4. The investigated glasses and glass-ceramics for pSOFC sealants are based on alkaline earth silicate compositions; for

example, BaO-Al₂O₃-SiO₂. Many authors reported their invented sealants based on this system by adding various oxide to tailor their properties including B₂O₃, CaO, MgO, SrO, Na₂O, La₂O₃, NiO, V₂O₅, Y₂O₃, ZrO₂, PbO, MnO and TiO₂ [9, 35, 39, 46-49]. Low silica and silica free borate base compositions were also investigated [50-52]. There are also included glass-ceramics composite system, such as oxide powder reinforced by adding MgO [53], boron nitride nanotube [54], YSZ nano- and micro-particle[55], sodium and sodium-free silicate particle [56] and silver particle[57].

The interface between glass sealant and metal interconnect in general is not present serious problem after joining, however, it is highly critical in long term operation [58-60]. Alkaline earth aluminosilicate glasses and glass-ceramics are more stable, however, there are the problems from the formation of high different CTE of BaCrO₄ (21.0–23.0 x10⁻⁶ K⁻¹[61]) and low CTE of monocelsian BaAl₂Si₂O₈ (2–3 x10⁻⁶ K⁻¹[10, 61]) from barium oxide containing glass-ceramics and ferritic stainless steel [6, 62] as following reaction.



Barium free glasses and glass-ceramics are another trend of development to avoid the reaction problems of barium and chromium containing alloys [48-49, 53, 63-72].

Alkali-containing glass-ceramics are generally avoided in compositions because it is able to harmfully react with metal during cell operation. The Na⁺ ion containing in glass-ceramics decrease their electrical resistivity because of high ionic mobility. However, pore and crack-free interface was recently reported in system Na₂O-CaO-Al₂O₃-SiO₂ by Smeacetto [73]-[64], while their electrical resistivity still was not reported.

Table 2.3 Developed glass compositions for SOFC sealants from many authors

Glass	Compositions													Reference
	Na ₂ O	MgO	CaO	BaO	SrO	Cr ₂ O ₃	ZnO	B ₂ O ₃	Al ₂ O ₃	SiO ₂	Y ₂ O ₃	La ₂ O ₃	Others	
<u>Alkaline earth silicate</u>														
BCAS4	-	-	9.2	55.6	-	-	-	-	5.5	25.3	-	-	-	[74]
BCAS5	-	-	8.8	57.4	-	-	-	-	5.4	22.1	-	-	-	[74]
7A	-	16.9	18.82	6.43	-	-	-	2.14	47.88	-	6.83	1.0NiO	-	[75]
7(Sr)-2B	-	16.92	18.83	-	4.35	-	-	2	2.14	47.92	-	6.84	1.0NiO	[76]
7A-Cr	-	16.82	18.72	6.4	-	0.5	-	-	2.13	47.64	-	6.8	-	[75]
10B	-	16.48	18.34	6.27	-	0.5	-	2	2.08	46.67	-	6.66	-	[70]
10C	-	16.14	16.85	9.21	-	0.5	-	2	2.04	45.73	-	6.53	-	[70]
G-18	-	-	8.8	56.4	-	-	-	7.3	5.4	22.1	-	-	-	[39, 67]
YSO-4	-	-	3.7	-	42.2	-	2.7	9.3	-	27.2	14.9	-	-	[77]
Glass #27	-	-	15	-	26.6	-	15	1.9	4.1	35.2	-	-	2.2TiO ₂	[78]
Mg1.5-55	-	8.9	-	50.7	-	-	-	-	-	40.4	-	-	-	[46]
Mg1.5-40-5B-10Pb	-	7.4	-	42	-	-	-	3.5	-	24.4	-	-	22.7PbO	[46]
Mg1.5-40-15B-	-	4.7	-	47.9	-	-	7.5	12.1	-	27.8	-	-	-	[46]
<u>Alkali alkaline earth silicate</u>														
SACN	9-12	-	20-25	-	-	-	-	-	10-14	50-55	-	-	-	[64, 79]
SACNZn	1.2	0.27	31.6	-	-	-	9.1	-	19.4	38.4	-	-	-	[73]
<u>Alkaline earth borosilicate</u>														
L2	-	-	-	47.4	-	-	-	10.3	9.0	17.7	-	15.6	-	[9]
LO6	-	-	-	20.0	-	-	-	60.0	5.0	15.0	-	-	-	[76]
LO9	-	-	-	50.0	-	-	-	30.0	5.0	15.0	-	-	-	[76]
SrLaB	-	-	-	-	15.2	-	-	20.5	9.0	3.5	-	51.8	-	[51]
MA12	-	8.4	-	-	-	-	-	8.8	9.7	22.7	-	50.4	-	[80]
VS1	-	-	-	-	33.9	-	-	15.2	-	26.2	24.7	-	-	[65]
VS2	-	-	-	-	29.8	-	-	13.4	-	23.0	-	33.8	-	[65]
VM1	-	16.6	-	-	-	-	-	19.2	-	33.1	31.1	-	-	[65]
VM3	-	20.1	-	-	-	-	-	23.1	16.9	39.9	-	-	-	[65]
BaBSi	-	-	-	50.0	-	-	-	19.9	-	24.0	1.9	2.2	2.0ZrO ₂	[62]

Glass	Compositions													Reference
	Na ₂ O	MgO	CaO	BaO	SrO	Cr ₂ O ₃	ZnO	B ₂ O ₃	Al ₂ O ₃	SiO ₂	Y ₂ O ₃	La ₂ O ₃	Others	
23	-	-	6.6	46.7	-	-	-	8.1	2.4	19.7	-	16.5	-	[39]
L09	-	-	-	68.6	-	-	-	18.7	4.6	8.1	-	-	-	[81]
P00	-	-	-	25.3	-	-	-	15.1	10.1	49.5	-	-	-	[81]
A2	-	-	-	60.6	-	-	-	12.6	5.0	21.8	-	-	-	[82]
VS1	-	-	-	-	33.9	-	-	15.2	-	26.2	24.7	-	-	[65]
17	-	3.9	5.5	23.9	-	-	-	17.4	7.7	15.1	-	26.5	-	[83]
Glass #59	-	-	-	34.3	23.2	-	-	15.6	-	26.9	-	-	-	[78]
A0	-	-	-	61.8	-	-	-	14.0	-	24.2	-	-	-	[82]
A2	-	-	-	60.6	-	-	-	12.6	5.0	21.8	-	-	-	[82]
Alkaline earth borate														
14a	-	20.0	20.0	10.0	-	-	-	40.0	10.0	-	-	-	-	[83]
MA1	-	8.1	-	-	-	-	-	33.9	9.4	-	-	48.6	-	[80]
BM1	-	10.5	-	45.6	-	-	-	43.0	-	-	-	-	-	[80]
BMA1 (GC)	-	6	-	6.7	-	-	-	32.2	8.9	-	-	46.2	-	[80]
BM2 (GC)	-	9.7	-	50.1	-	-	-	40.2	-	-	-	-	-	[80]

Table 2.4 Selected properties of some glass composition for SOFC sealants

Glass code	T_g (°C)	T_c (°C)	T_s (°C)	CTE ($\times 10^{-6} \text{ K}^{-1}$)	Electrical resistivity ($\times 10^6 \Omega \cdot \text{cm}$)	Ref.
MBS	–	–	700	10	100(400–700 °C)	
L2	655	862	710	11.1 (RT–655 °C)	–	[9]
10B	755	904	–	8.4 (200–600 °C)	–	[70]
10C	756	906	–	8.71(200–600 °C)	–	[70]
17	620	–	–	8.8	–	[83]
14a	576	–	–	9.4	–	[83]
BCAS4	609	755	672	11.9 (RT–609 °C)	5.2 (700 °C) 0.88 (800 °C)	[74]
BCAS5	608	720	660	12.4 (RT–608 °C)	0.36 (700 °C) 0.09 (800 °C)	[74]
7A	685	912	716	8.69 (200–500 °C)	–	[75]
MA1	623	887	671	9.01 9.5–10.3 (GC)	450 (700 °C) 28 (800 °C)	[80]
MA12	638	907	723	8.33 7.65–8.78 (GC)	– –	[80]
BMA1	620	785	656	9.66 9.24–10.0 (GC)	350 (700 °C) 30 (800 °C)	[80]
BM1	570	804	616	10.06 9.36–10.77 (GC)	46 (700 °C) 5.8 (800 °C)	[80]
BM2	582	845	593	11.1 11.18–12.13 (GC)	22 (700 °C) 3.8 (800 °C)	[80]
7A-Cr	675	895	721	8.48 (200–500 °C)	–	[75]
VS1	626	–	–	7.76 (RT–626 °C)	–	[65]
VS2	620	–	–	5.26 (RT–620 °C)	–	[65]
VM3	735	–	–	1.99 (RT–735 °C)	–	[65]
L09	–	–	–	10.98	–	[81]
18	–	630	685	11.8 (25–630 °C) 10.8 (GC)	– –	[39]
G18	–	–	–	10.5	–	[67]

Glass code	T_g (°C)	T_c (°C)	T_s (°C)	CTE ($\times 10^{-6} \text{ K}^{-1}$)	Electrical resistivity ($\times 10^6 \Omega \cdot \text{cm}$)	Ref.
G018-281	652	–	927	4.6 (20–300 °C)	–	[84]
SACN	700	780, 900	–	9.7 (200–400 °C)	–	[64, 79]
Mg1.5-55	715	–	750	10.1	–	[46]
SACNZn	740	950–1020	–	7.8 (200–400 °C)	–	[73]
				10 (GC)	–	
A0	622	763,907		10.83	–	[82]
A2	602	830	–	10.67	–	[82]

2.5 Effect of glass composition on properties of glass and glass-ceramic sealants

2.5.1. Thermal expansion

Thermal expansion coefficient of glass and glass-ceramic sealants is one of the most important properties for consideration. It should match with other joining components in SOFC to avoid thermal stress. Thermal stress always increases due to difference in CTE between the adjoined SOFC component and the sealant during operation. Tensile stress (CTE of component > CTE of sealant) and compressive stress (CTE of components < CTE of sealant) are generally occurred at the interface [85]. It should not exceed $1 \times 10^{-6} \text{ K}^{-1}$ [45, 86].

The CTEs of cathode lanthanum manganate, YSZ electrolyte, and metallic interconnects are $12.4 \times 10^{-6} \text{ K}^{-1}$ [87], $8.5\text{-}10.5 \times 10^{-6} \text{ K}^{-1}$ and $11\text{-}15 \times 10^{-6} \text{ K}^{-1}$ [88]. In order to seal these cell components the CTE of the sealant should be $8.5\text{-}15 \times 10^{-6} \text{ K}^{-1}$, however, in practice, desired CTE is in range of $9\text{-}13 \times 10^{-6} \text{ K}^{-1}$.

After thermal treatment, the CTE of glass can change by two reasons, which are (i) rearrangement of structure and (ii) crystallization of crystalline phases with different CTEs. The CTEs of crystalline phases in alkaline earth oxide containing glass-ceramics are shown in Table 2.5. Barium oxide borosilicate glass can crystallize $\text{BaAl}_2\text{Si}_2\text{O}_8$ during heat treatment at 750–800 °C. $\text{BaAl}_2\text{Si}_2\text{O}_8$ has three polymorphs including monoclinic, orthorhombic, and hexagonal celsian with different CTEs. Celsian phase has the lowest

CTE and it increases with thermal treatment time until complete crystallization. Therefore the CTE of BaO-containing seal glass decreases from $11.5 \times 10^{-6} \text{ K}^{-1}$ to $7.5 \times 10^{-6} \text{ K}^{-1}$ [39]. Similarly to SrO-containing borate seal glass, the CTE decreases from $9.5 \times 10^{-6} \text{ K}^{-1}$ to $6.78 \times 10^{-6} \text{ K}^{-1}$ after heat treatment for 50 h at 800 °C [55]. The other alkaline earth containing glass-ceramics, which can be crystallize high CTE crystalline phases such as enstatite, clinoenstatite, forsterite, calcium orthosilicate, are also interested.

Table 2.5 CTE of crystalline phases in glass-ceramics sealants [10, 85, 89]

Crystalline phase	Formula	CTE ($\times 10^{-6} \text{ K}^{-1}$)
Quartz	SiO_2	11.2-23.3
Cristobalite	SiO_2	12.5-50
Enstatite	MgSiO_3	9.0–12.0
Clinoenstatite	MgSiO_3	7.8–13.5
Protoenstatite	MgSiO_3	9.8
Forsterite	Mg_2SiO_4	9.4
Wollastonite	CaSiO_3	9.4
Calcium orthosilicate	Ca_2SiO_4	10.8–14.4
Barium silicate	BaSiO_3	10.5–12.5
	$\text{Ba}_2\text{Si}_3\text{O}_8$	12.6
Barium borate	BaB_2O_4	$\alpha_a = 4.0$ $\alpha_c = 36.0$
Barium zirconate	BaZrO_3	7.9
Hexacelsian	$\text{BaAl}_2\text{Si}_2\text{O}_8$	6.6–8.0
Monocelsian	$\text{BaAl}_2\text{Si}_2\text{O}_8$	2.3
Orthorhombic celsian	$\text{BaAl}_2\text{Si}_2\text{O}_8$	4.5–7.1
Hexacelsian	$\text{SrAl}_2\text{Si}_2\text{O}_8$	7.5–11.1
Monocelsian	$\text{SrAl}_2\text{Si}_2\text{O}_8$	2.7
Orthorhombic celsian	$\text{SrAl}_2\text{Si}_2\text{O}_8$	5.4–7.6
Cordierite	$\text{Mg}_2\text{Al}_4\text{Si}_5\text{O}_{18}$	2.0

2.5.2. Chemical stability

The glass-ceramic sealant must be operated in both oxidizing and reducing atmosphere and interfaced with ceramic and metal components at high temperature;

therefore, it must possess high chemical stability. Chemical stability should be considered in two aspects, which are the stability of bulk glass and stability of glass interfaces with other components of SOFC.

2.5.2.1. Chemical stability of bulk glass

Two main aspects of chemical stability should be considered, which are vaporization of glass and its chemical interaction with oxidizing and reducing atmospheres. The vaporization affects the changes of glass compositions, mechanical properties, and electrical properties. Alkali oxides and boron oxides have show higher vaporization at SOFC operating temperature because they have low melting points and high vapor pressures. While alkaline earth oxides, rare earth metal oxides, and alumina do not vaporize from a seal glass [90-91].

Alkali oxide containing borate glass and borosilicate glass can vaporize in the form of gaseous borates and alkali metaborates [78]. Na_2O vaporizes from Na_2O containing silicate glass sealant at 750 °C and from sodium borate glass at 1000 with much as 13 wt.% loss in wet atmosphere to formation of $\text{Si}(\text{OH})_4$ [33, 92].

Vaporization of B_2O_3 can increase in wet environment [78]. B_2O_3 reacts with water to form HBO_2 gas, and then breaks the glass network. BO_2 gas, which vaporizes from $\text{CaO-SrO-ZnO-B}_2\text{O}_3\text{-Al}_2\text{O}_3\text{-TiO}_2\text{-SiO}_2$ glass sealant, increases with temperature and heat treatment time. The weight loss cause by vaporization of $\text{B}_3\text{H}_3\text{O}_6$ increases from 0.16 to 0.98 mg/cm^2 when the atmosphere is changed from oxidizing atmosphere to 30% H_2O reducing atmosphere, after heat treated at 800 °C for 168 h. The weight loss of the glass increases from 2 to 20 mol% [78].

Addition of CaO in Na_2O -silicate glass can increase the chemical resistance to water-induced phase separation, while B_2O_3 performs the opposite effect [91]. Al_2O_3 shows its effect on improving the chemical stability of glass sealants [91]. Al_2O_3 inhibits the formation of the hydrated, open network structure surface layer. Addition of transition metal oxides, for example, ZrO_2 and TiO_2 , also can improve the chemical stability.

2.5.2.2. Chemical stability of interface

A sealant should have high interfacial stability with other SOFC components without strength decrease and flaw formation to achieve gas-tightness. There are many factors such as compositions, wetting behaviors, and bonding conditions (temperature, pressure, and atmosphere) should be considered.

The reaction between glass and glass-ceramic sealant and metal interconnect is more severe than the other SOFC components. The interactions depend on the glass and interconnect compositions, atmospheres, and sealing conditions. Ferritic stainless steel is preferred to use as interconnect because it has high electrical conductivity by forming of Cr_2O_3 [93]. Consequently, various chromia forming stainless steel alloys are being developed as interconnect, for example, Crofer22 APU, AISI430 and AISI441 alloys [93].

Glass in system Na_2O - CaO -silicate glass reacts with pre-oxidized AISI430 stainless steel in 3% H_2O reducing atmosphere at 800 °C after 200 h and forms Cr, Fe, Mn and O enriched interface of 1-2 μm thick [94]. Addition of B_2O_3 into Na_2O - CaO -silicate glass system increases the thickness to 20 μm . Although, the boron oxide is believed to improve glass wetting on metal alloy by decreasing viscosity, in recent works, B_2O_3 is avoided or kept to be lowest in glass compositions. It was found that chromium and iron diffuse up to 50 μm into BaO - MgO -borosilicate and BaO - ZnO -borosilicate glasses after thermal treatment at 850 °C for 100 h[46].

In general, glass sealant wets the YSZ electrolyte very well. Interface stability problem between glass sealant and YSZ electrolyte was not found [9, 33, 95]. However, there are a few case of the problem, for example, a BaO - CaO -borosilicate glass reacts with YSZ and form BaZrO_3 after heat treatment at 750 °C for 1200 h[39]. In a conclusion, the interfacial stability is not major consideration.

2.5.3. Mechanical properties

2.5.3.1. Bonding strength

There are a few papers reported about bonding strength of glass and glass-ceramic sealants with other SOFC components. However, the high bonding strength is preferred. It depends on glass composition, sealing condition, thermal treatment, and interfacial morphology.

The bonding strengths of Na₂O-silicate glass/MgO composite sealant and SrO-CaO-borosilicate glass with Crofer22 APU stainless steel are 1.87 and 6.2 MPa, respectively [33, 96]. The bonding strength of SrO-CaO-borosilicate glass with Crofer22 APU stainless steel decreases from 6.9 to 0.5 MPa after 500 h in air, in contrast, it increase to 7.0 MPa after heat treatment at 800 °C for 250 h in 30% H₂O reducing atmosphere. The reason of increasing bonding strength in the wet atmosphere is not reported. The bonding strength of BaO-CaO-silicate glass with a metallic interconnect is reported in term of fracture energy at room temperature and shear strength at 800 °C. The fracture energy of interface increases from 12 to 23 J·m² after heat treatment at 800 °C for 120 h [33].

Pore and crack-free interface can affect to the bonding strength. Some works improve the surface strength by preoxidizing the surface of stainless steel. A SrO-CaO-borosilicate glass with preoxidized Crofer 22 APU stainless steel decrease from 6.2 to 2.6-2.9 MPa because of an oxide layer at the interface [60]. Na₂O-CaO-silicate glass cannot join with AISI430 stainless steel, but it bonds well with pre-oxidized AISI430 stainless steel. The reason is that pre-oxidation layer of AISI430 stainless steel form a 1-5 μm thick Cr-Mn-Fe oxide layer which aids the bonding [97].

2.5.3.2. Thermal cycling stability

The sealant has to operate up to thousands of thermal cycles. The interfaces of the glass and glass-ceramic sealant are under thermomechanical stress. Crack initiation occur at the interfaces or in the glass or glass-ceramic sealant [85]. The crack is the reason to gas leakage, and degradation of cell performance. The thermomechanical

stress at the interface between glass or glass-ceramic sealant and metal interconnect generates thermal strain and mechanical strain. The thermal strain, ε_t depends on the CTEs of glass and the adjoined component and the temperature difference according to

$$\varepsilon_t = (\alpha_g - \alpha_c)\Delta T \quad (2.7)$$

Where α_g and α_c are the CTEs of glass and adjoined SOFC component, respectively. ΔT is the temperature difference during the thermal cycle under examination. Furthermore, mechanical strain depends on the differential pressure in the cell, load of cell unit, and externally applied load.

Crack can propagate in opening mode or sliding mode. The sliding mode dominates the failure of a glass sealant [59]. The fracture of glass sealant/ interconnect interface occurs when the thermomechanical stress generated exceeds the tensile strength. The stress is concentrated at cell edges where a seal glass bonds with other components. It increases along the inner edges of seal glass close to the fuel because the temperature from electrochemical reaction is higher. The maximum thermomechanical stress depends on the seal configuration, such as seal thickness. The smooth and thin glass seal is more advantageous.

2.5.3.3. Sealing ability

Sealing ability is ability to resist gas leak and mixing in cell stack. In order to evaluate the sealing ability of glass and glass-ceramic sealants, the leakage rate is measured. In general, the glass is sandwiched between two SOFC components such as metallic interconnect and electrolyte to measure the leak rate. There are different studies use different and incomparable experimental methods. For example, the difference of leakage rate units are reported in literature, the first is leakage rate is measured by the leaked gas volume across a tri-layer assembly per unit time per unit seal length at constant pressure gradient and expressed as standard cubic centimeter per minute per centimeter ($\text{sccm}\cdot\text{cm}^{-1}$), however, the required pressure gradient is not defined clearly [98]. Secondly, the gas leakage is measured from the pressure drop across a sandwich sample in $\text{Pa}\cdot\text{m}^2\cdot\text{s}^{-1}$. It is not clearly about the area of sandwich sample

or seal glass is used in expression [99]. Another one, leakage rate is reported as volume of gas leakage across the sealant in $\text{L}\cdot\text{min}^{-1}$ [33]. In this case, the pressure is not well defined. However, it can review each work individually as followed. The leakage rate of a $\text{SrO-CaO-Y}_2\text{O}_3\text{-B}_2\text{O}_3\text{-SiO}_2$ glass sealant varies from 10^{-2} to 10^{-4} $\text{sccm}\cdot\text{cm}^{-1}$ as a function of temperature [100]. Alkaline earth silicate glass with low boron and phosphorous contents mixed with ZrO_2 powder performs good sealing ability after thermal treatment at 650 and 800 °C for 50 h with leakage rate lower than 0.094 $\text{sccm}\cdot\text{cm}^{-1}$). The leakage rate of glass in the $\text{BaO-CaO-Al}_2\text{O}_3\text{-B}_2\text{O}_3\text{-SiO}_2$ system is $1.0\text{-}9.5 \times 10^{-7}$ $\text{Pa}\cdot\text{m}^2\cdot\text{s}^{-1}$ at 800 °C [99]. The leakage rate of $\text{Na}_2\text{O-Al}_2\text{O}_3\text{-SiO}_2$ glass/MgO composite sealant is $0.5\text{-}1.2$ $\text{L}\cdot\text{min}^{-1}$ after heat treatment at 750 °C, but decreases to $0.2\text{-}0.4$ $\text{L}\cdot\text{min}^{-1}$ after 2500 h.

It can be seen that leakage test is variously defined by different studies and may depend on sample geometry and specific design. A standard leakage test procedure is thus needed so that the literature results can be confirmed and compared.

2.5.4. Electrical resistivity

The electrical conductivity in glass and glass-ceramics is generally controlled by ionic charges from alkali and alkaline earth oxide compositions and by electrons and holes from transition metal in the glass and glass-ceramic composition [101]. The electrical resistivity of glass and glass-ceramic depends on the composition and the devitrification including phase separation and crystallization of starting glassy phase. It also depends on the operating temperature and should be more than 1×10^{-4} $\Omega\cdot\text{cm}$ in order to avoid a shorting circuit [36, 102].

A borate glass has higher electrical resistivity than a silicate glass when the modifiers are present in both systems. The reason is that the addition of modifier ions in a borate glass reduces non-bridging oxygen ions due to “boron anomaly” while the non-bridging oxygen ions increase in a silicate glass [33, 91]. The electrical resistivity increases when the ionic radius and valence of modifier ions increase, for example, the electrical resistivity of $\text{Cs}^+ > \text{Rb}^+ > \text{K}^+ > \text{Na}^+$ for alkali oxide containing glasses and $\text{Ba}^{2+} > \text{Sr}^{2+} > \text{Ca}^{2+} > \text{Mg}^{2+}$ for alkaline earth oxide containing glasses [101]. Because the modifier

ion creates non-bridging oxygen species, the electrical resistivity was decreased by adding higher amount of modifier. Thus, higher modifier contents should be avoided for glass and glass-ceramic sealants.

The initial addition of intermediate oxide could increase the electrical resistivity, in contrast, it decrease with higher addition [92]. For example, two ionic sites in glass system $\text{Na}_2\text{O}-\text{Al}_2\text{O}_3-\text{SiO}_2$, which are Na-non-bridging oxygen site and $\text{Na}^+[\text{AlO}_{4/2}]$ site. The concentration of Na-non-bridging oxygen site and Na^+ ions are decreased at initial addition of Al_2O_3 , resulting in an increase in electrical resistivity. Further addition of Al_2O_3 increases the concentration of $\text{Na}^+[\text{AlO}_{4/2}]$ site and decreases the electrical resistivity because of increasing mobility of Na^+ ions.

Effect of crystallization in glass on the electrical resistivity is exactly dependent on the composition and the morphology of crystalline phases and remaining glass matrix. The temperature also affects the electrical resistivity of glass and glass-ceramics. The electrical conductivity of glass and glass-ceramics increases with temperature because the diffusivity of modifier ions increases with temperature. At temperature below T_g , electrical resistivity shows Arrhenius behavior [77]

$$\rho = \frac{T}{A} \exp\left(\frac{E}{kT}\right) \quad (2.8)$$

Where E the activation energy for ionic mobility is, T is temperature, A is constant, and k is Boltzmann constant.

If the temperature is above T_g , the electrical resistivity decrease according to Vogle-Tamman-Fulcher equation.

$$\rho = \frac{T}{A'} \exp\left(\frac{B}{T-T_0}\right) \quad (2.9)$$

Where A' , B and T_0 are constants.

CHAPTER 3

EXPERIMENTAL PROCEDURE

The experimental procedure has been divided into two parts. The first part is development of barium free glass compositions from selected glass and glass-ceramics system from literatures to study the possibility to preparation and joining with metal interconnect and YSZ electrolyte. The selected compositions should be completely melted at 1450–1500 °C and their CTE should be in the range of requirement. Barium free glass-ceramic compositions were designed and prepared in a system of $R_2O - RO - Al_2O_3 - SiO_2$, where R is referred to as an alkali metal or alkali earth, such as Na, K, Ca and Mg. Na and K were varied to increase CTE of glass-ceramics by crystallization of high CTE Nepheline and Kaliophilite phases, and study their effects on the other properties. The primary requirements of pSOFCs glass-ceramic sealant, which are T_g , T_c , coefficient of thermal expansion and joining ability with chromium-forming ferritic stainless steel, AISI 430 stainless steel and Crofer 22 APU stainless steel, will be investigated. The Na_2O and K_2O components were varied in the compositions, their thermal properties and phase transformation in glass ceramic sealant after heat treatment at the joining temperature (900 °C) and working temperature (800 °C) were investigated.

In the second part, the alkali free and maintained concept of barium free glass - ceramics from the basic chemical composition as the first part were developed in order to avoid the decrease of electrical resistivity and high chemical reaction with the interconnect in long term use of glass–ceramics containing alkali oxide. Consequently this part is a development of alkali free and barium free glass–ceramic sealants from åkermanite and diopside based on $MgO-CaO-B_2O_3-Al_2O_3-SiO_2$ system.

3.1 Part I: Development of glass-ceramics seal in a system of R_2O [R = Na, K]–MgO–CaO–Al₂O₃–SiO₂

3.1.1. Glass formula selection

The glass compositions were selected from the literatures and phase diagram in consideration of coefficient of thermal expansion and thermal properties such as softening temperature. Then glass compositions which have ability to completely melted at temperatures between 1450–1500 °C and have a good thermal properties were selected to develop and examination their properties for joining and sealing with AISI430 and YSZ ceramics. The selected glasses, which their compositions were shown in Table 3.1, were prepared by the melting process. Their expected constitutional compounds were calculated and shown in Table 3.2. The constitutional compounds are assumed to be primary crystalline phase after the thermal treatment and fully crystallization, thus, the CTEs of glass-ceramics depend on the crystalline phase compositions.

Table 3.1 Starting glass compositions

Sample	Chemical composition (mol %)								
	SiO ₂	Al ₂ O ₃	CaO	MgO	ZnO	TiO ₂	Na ₂ O	K ₂ O	Bi ₂ O ₃
AZS11	50	5	-	21	20	4	-	-	-
AAS3	60	18	12	-	-	10	-	-	-
SACN	52	12	25	-	-	-	11	-	-
CMS1	50	10	20	10	-	-	10	-	-
CMS2	55	10	10	20	-	-	10	-	-
S1	51	9	5	25	-	-	5	5	-
S2	54	10	5	23	-	-	4	4	-
S3	55	8	2	26	-	-	2	2	5
S1N	53.5	11.5	7.5	27.5	-	-	-	-	-

Table 3.2 Crystalline phases and CTEs of glass compositions and constitutional compound calculation (CIPW norm) of glass-ceramics

Sample	Crystalline phase compositions	CTE (10^{-6} K^{-1})	Reference
AZS11	Enstatite solid solution+ cristobalite + willemite solid	10.2 (200-400 °C)	[85]
AAS3	Anorthite + cristobalite	8.5	[85]
SACN	$\text{Ca}_2\text{Al}_2\text{SiO}_7 + \text{NaAlSiO}_4$	9.4–9.8 (300–500 °C)	[64]
CMS1	$\text{Na}_2\text{O}\cdot\text{Al}_2\text{O}_3\cdot 2\text{SiO}_2 +$ $\text{Na}_2\text{O}\cdot 2\text{CaO}\cdot 3\text{SiO}_2 + \text{CaO}\cdot\text{SiO}_2$	-	-
CMS2	$2\text{MgO}\cdot\text{SiO}_2 + \text{Na}_2\text{O}\cdot\text{Al}_2\text{O}_3\cdot 2\text{SiO}_2$	-	-
S1	$2\text{MgO}\cdot\text{SiO}_2 + \text{K}_2\text{O}\cdot\text{Al}_2\text{O}_3\cdot 2\text{SiO}_2 +$ $\text{Na}_2\text{O}\cdot\text{Al}_2\text{O}_3\cdot 2\text{SiO}_2$	-	-
S2	$\text{MgO}\cdot\text{SiO}_2 +$ $\text{Na}_2\text{O}\cdot\text{Al}_2\text{O}_3\cdot 6\text{SiO}_2 + \text{K}_2\text{O}\cdot\text{Al}_2\text{O}_3\cdot 6\text{SiO}_2$	-	-
S3	$\text{MgO}\cdot\text{SiO}_2 + \text{Na}_2\text{O}\cdot\text{Al}_2\text{O}_3\cdot 6\text{SiO}_2 + 2\text{MgO}\cdot\text{SiO}_2 +$ $\text{K}_2\text{O}\cdot\text{Al}_2\text{O}_3\cdot 6\text{SiO}_2 + \text{CaO}\cdot\text{Al}_2\text{O}_3\cdot 2\text{SiO}_2$	-	-
S1N	$\text{MgO}\cdot\text{SiO}_2 + \text{CaO}\cdot\text{Al}_2\text{O}_3\cdot 2\text{SiO}_2 + 2\text{MgO}\cdot\text{SiO}_2$	-	-

After testing the glass forming ability of the selected compositions, the results are shown in Chapter 4, the glass compositions in Table 3.3 were designed from CMS1 and CMS2 compositions by varying amount of Na_2O and K_2O in glass compositions. Both alkali oxides were also studied their “mixed-alkali effect” on CTE and electronic resistivity by adding 5% each oxide in Table 3.3.

Table 3.3 List of glass compositions

Oxides	Compositions (mol%)							
	CM11	CM12	CM13	CM14	CM21	CM22	CM23	CM24
SiO ₂	52.5	50	50	50	52.5	50	50	50
Al ₂ O ₃	12.5	10	10	10	12.5	10	10	10
CaO	22.5	20	20	20	12.5	10	10	10
MgO	12.5	10	10	10	22.5	20	20	20
Na ₂ O	-	5	10	-	-	5	10	-
K ₂ O	-	5	-	10	-	5	-	10

3.1.2. Glass preparation

Glass compositions were prepared from chemical grade reagents, which are CaCO₃, MgCO₃, Na₂CO₃, K₂CO₃, Al₂O₃, and SiO₂ (see Appendix A). Batch of mixed oxides was loaded in a platinum crucible and melted at 1450 °C for 2 hour in electric furnace. The molten glass was then poured in a graphite mould. Cast glass was cut and cropped for the dilatometric measurement. The rest was quenched to room temperature by air, and ground for other subsequent measurements and testing. Glass powder was ground in an agate mortar and sieved through a 230 mesh screen (<63 μm). The as-fabricated glass must be homogeneous with non-crystallization and undissolved phases. Particle size distribution of glass powder was performed by laser light scattering technique using Malvern Mastersizer 2000 (Malvern Instruments Ltd, UK).

3.1.3. Determination of glass transition temperature and crystallization temperature

Thermal properties of glass powder were analyzed by differential thermal analysis, DTA (DTA7, Perkin Elmer, USA). An as-fabricated glass sample was ground in an agate mortar and sieved through a 230 mesh screen (< 63 μm). Approximately 20 mg of glass powder was loaded in a platinum crucible lining with a thin layer of alumina powder in a sample holder of DTA furnace. Standard alumina was used as a reference

material. They were heated from room temperature to 1200°C with a heating rate of 10 K·min⁻¹. Glass transition temperature (T_g) and crystallization temperature (T_c) were determined.

DTA is able to measure reaction energy (in term of endothermic and exothermic energy) and temperature, glass transition temperature, phase transition temperature and energy, and specific heat or heat capacity of materials as a function of temperature. In this part, DTA with thermal analyzer software was used to examine T_g and T_c of selected glass. T_g was determined automatically by computer software, which is a midpoint (T_m) between extrapolated onset temperature (T_i) and extrapolated end temperature (T_e) in Fig. 3.1. T_c was determined by onset temperature as shown in Fig. 3.2.

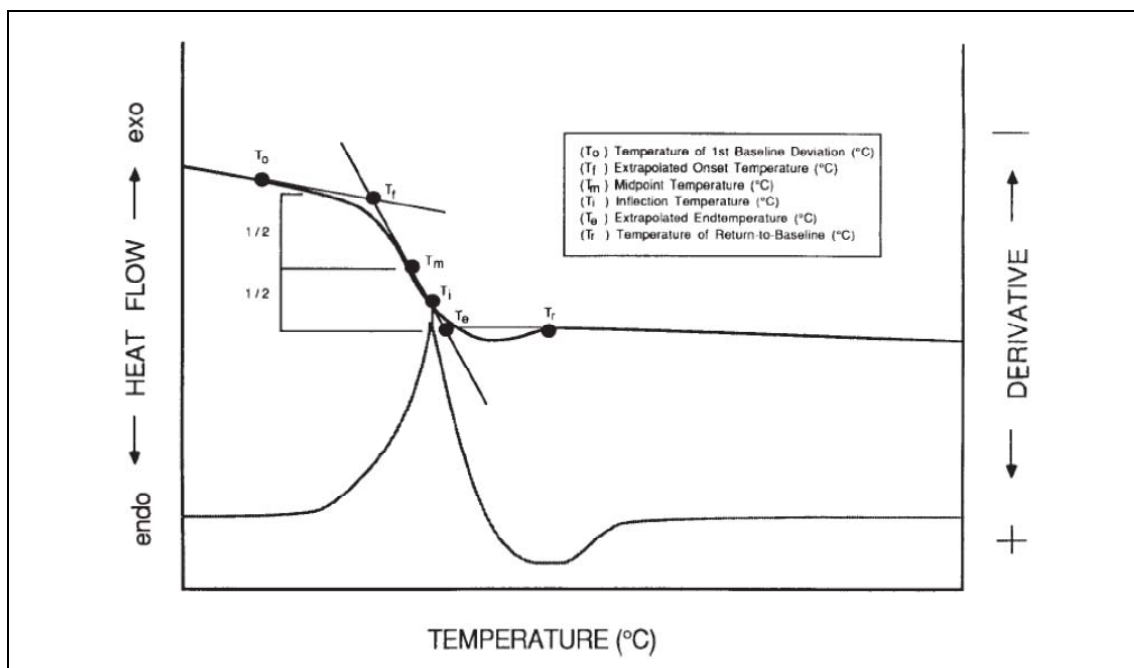


Fig. 3.1 Glass transition region measured temperatures [103]

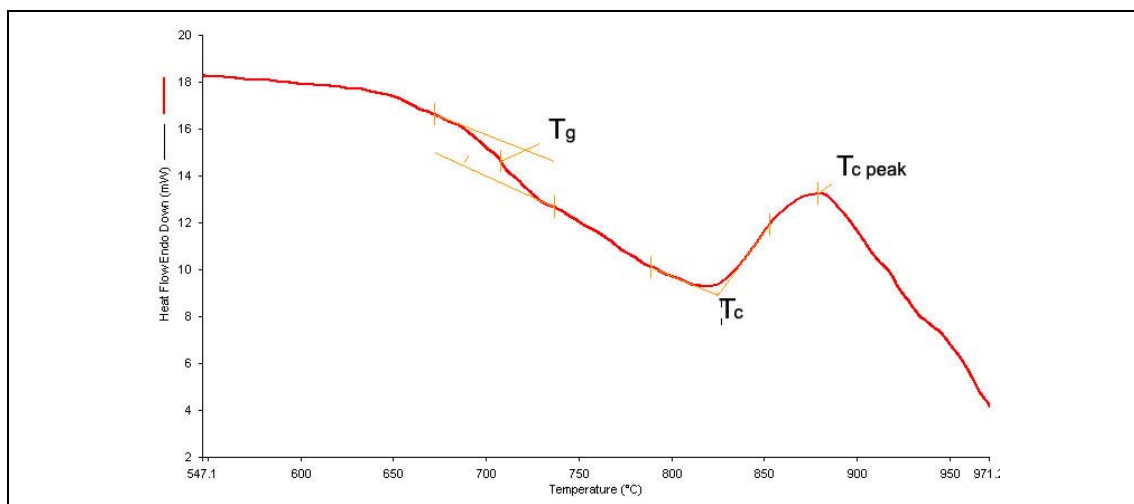


Fig. 3.2 T_g and T_c determined using computer software.

3.1.4. Microstructure and crystallization observation

Homogeneity and undissolved phases of as-fabricated of glass samples were determined by an optical microscope; OM (Olympus BX60M, Olympus optical co. Ltd., Japan) under reflected light with magnifications ranging from 50X to 1000X. Digital images were taken using a digital camera (Olympus DP12, Olympus optical co. Ltd., Japan).

Crystalline phase in glass and glass–ceramics was detected and examined by X-ray diffractometer (Bruker D8 Advance, Germany). The operating condition is: $10^\circ < 2\theta < 60^\circ$, step size of 0.02° and 40 kV.

3.1.5. Dilatometric measurement

Dilatometric measurement of glass and glass–ceramics was used to examine the coefficient of thermal expansion (CTE), glass transition temperature (T_g) and dilatometric softening temperature (T_d) of as-melted glass and crystallized glass (glass-ceramics). In order to prepare the sample, as-melted glass was cut into 5 mm x 5 mm x 25 mm. While in case of glass-ceramic samples, the compacted glass powders were heat treated at 900 °C for 2 h with heating and cooling rates of of 5 K min^{-1} , consequently, it was cut into 5 mm x 5 mm x 25 mm. CTE was determined by a slope of linear range from dilatometric curve (Netzsch DIL402C, Netzsch, Germany).

3.1.6. Joining test

Joining test was performed by joining glass paste between AISI 430 stainless steel (SC17, Thainox Stainless Public Co., Ltd.). The glass will be ground and sieved below 63 μm . The powder of glass was blended with the 1 % PVA solution to form viscous paste. The glass paste was spread on the surface between the couple of AISI 430 stainless steel plates (50 x 25 x 0.3 mm) as a sandwich. Before application of the glass paste, the stainless plates were thoroughly cleaned in alcohol using an ultrasonic bath for 10 minutes. The sandwich sample was then heated to up to 900 °C keeping at this temperature for 2 hours with heating and cooling rate of 3 $\text{K}\cdot\text{min}^{-1}$. The cross section of joined sandwich specimens was observed using SEM/EDS. For joining with YSZ ceramic, the method is the same as joining with AISI 430 stainless steels.

Cross section of joining sample between glass-ceramics and AISI430 stainless steel was observed by scanning electron microscope; SEM (JEOL JSM-6400 model) and energy dispersive spectrometry; EDS (OXFORD Instrument ISIS 300).

3.1.7. Electrical resistivity measurement

In order to measure the electrical resistivity of glass-ceramics, a pellet shape of pressed glass powder was sintered in an electric furnace with a heating rate of 5 $\text{K}\cdot\text{min}^{-1}$ dwelling at 900 °C for 2 hours. The surface of as sintered sample was ground into smooth and clear surface before coated with silver paste. The impedance spectra was collected over the frequency range of 5 Hz to 13 kHz, and the temperatures range of 600 – 800 °C in air using HP 4192A LF Impedance Analyzer, (Hewlett Packard, Japan). The impedances were measured at every 50 °C interval. The sample was soaked at each temperature for 30 min before collect the data to ensure the stable temperature. The experimental setup is illustrated in Fig. 3.3. The impedance spectra were plotted between real part Z' and imaginary part Z'' , which is called Nyquist plot.

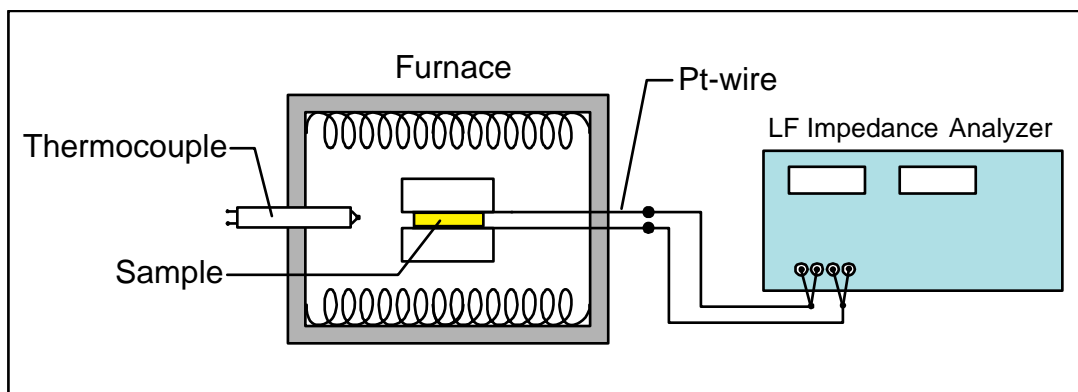


Fig. 3.3 Experimental setup of impedance analysis

The bulk electrical resistivity was calculated from;

$$\rho = \frac{RA}{L} \quad (3.1)$$

Where ρ = electrical resistivity in $\Omega \cdot \text{cm}$

R = electrical resistance in Ohm, Ω

L = sample thickness in cm

A = cross-section area of sample in cm^2

3.2 Part II: Development of glass-ceramics seal in system $\text{MgO-CaO-B}_2\text{O}_3\text{-Al}_2\text{O}_3\text{-SiO}_2$

In this part, some experiments were done in “Institut für Gesteinshüttenkunde” (GHI) laboratory, RWTH Aachen, Germany. The experimental procedures of glass preparation, thermal property measurement and electrical resistivity are followed the same experiments in Part I. However to clarified of some differences in detail, the experimental procedure in the same articles in part I is explained again.

3.2.1. Glass formula selection

The glass compositions were selected by considering the glass-ceramics based on åkermanite and gehlenite system. From the previous studies, the volumetric mean thermal expansion coefficient of åkermanite and gehlenite are $32.1 \times 10^{-6} \text{ K}^{-1}$ and $28.3 \times 10^{-6} \text{ K}^{-1}$ in the temperature range of 298–1400 K, reported by Merlini et al [104].

Table 3.5 Constitutional Compound Calculations (CIPW norm), and FactSage calculations of glass designed glass composition

Compounds (CIPW norm) (wt.%)	31	32	33	34	35	36	37
M2S (Fosterite)	30.02	20.00	15.01	13.19	24.81	18.50	6.00
CMS2 (Diopside)		4.99	9.97	4.45	0.00	0.00	0.00
CAS2 (Anorthite)		5.02	9.99	19.56	26.76	3.00	45.00
C2MS2 (Åkermanite)	69.98	69.99	65.04	62.80	37.02	78.50	49.00
C2AS (Gehlenite)					11.41		
Total	100.00	100.00	100.00	100.00	100.00	100.00	100.00
Compounds (FactSage) (wt.%)	31	32	33	34	35	36	37
M2S (Fosterite)	30.00	20.00	15.01	13.19	24.82	18.50	5.89
CMS2 (Diopside)		5.00	9.96	4.43			
CAS2 (Anorthite)		4.99	9.99	19.56	26.75	4.50	44.80
C2MS2 (Åkermanite)	70.00	70.00	65.05	62.81	37.02	77.00	49.27
C2AS (Gehlenite)					11.42		
Total	100.00	100.00	100.00	100.00	100.00	100.00	99.96
Liquidus temperature (°C)	1500	1410	1380	1340	1360	1410	1200

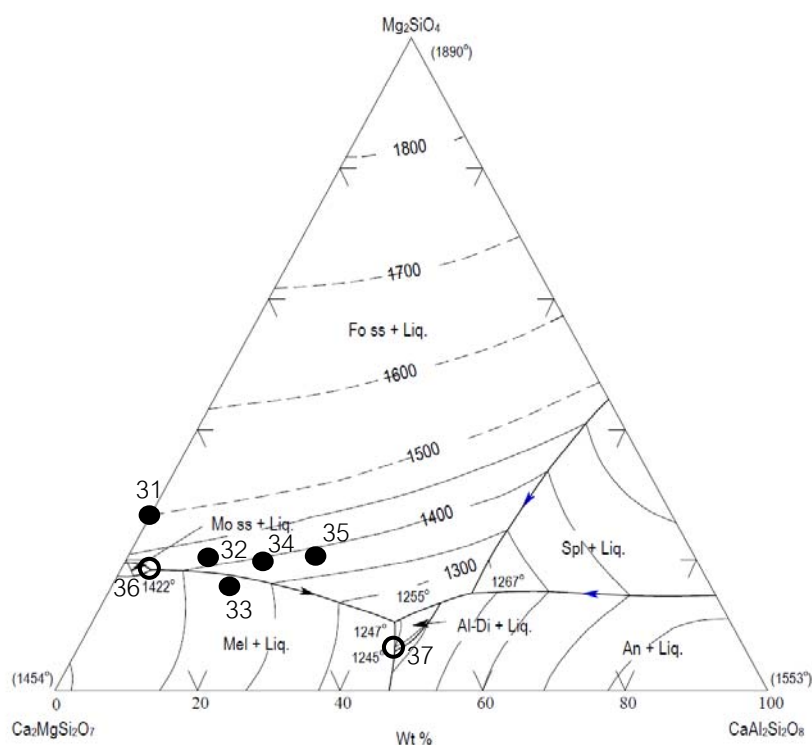


Fig. 3.4 Phase diagram (Acer. Fig. 5473-A) with positions of glass 31 - 37 compositions

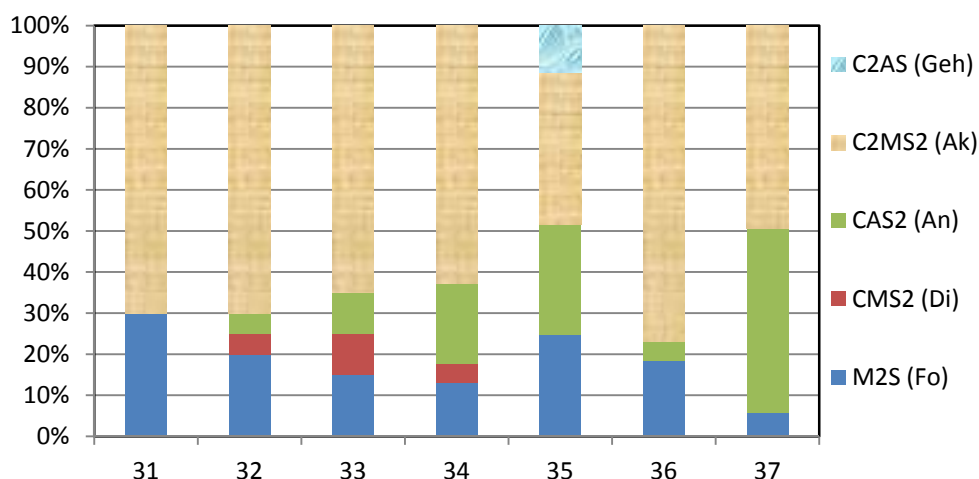


Fig. 3.5 Equilibrium plot of Constitutional Compounds of glass 31 - 37 calculated by FactSage

The example of plot of constitutional compounds vs temperature in Fig. 3.6 shows the constitutional compounds at equilibrium and “the liquidus temperature”; the temperature at which slag curve rises up to become 100 wt.%. It was useful to help to determine and select only low liquidus temperature for melt and preparation. The other plots, glass 32 to 37 compositions, are shown in Appendix B and the liquidus temperatures are summarized in Table 3.5 . The glass compositions 34, 35 and 37 were selected to prepared because their liquidus temperature were low enough and easy to melt and pour at 1500 °C.

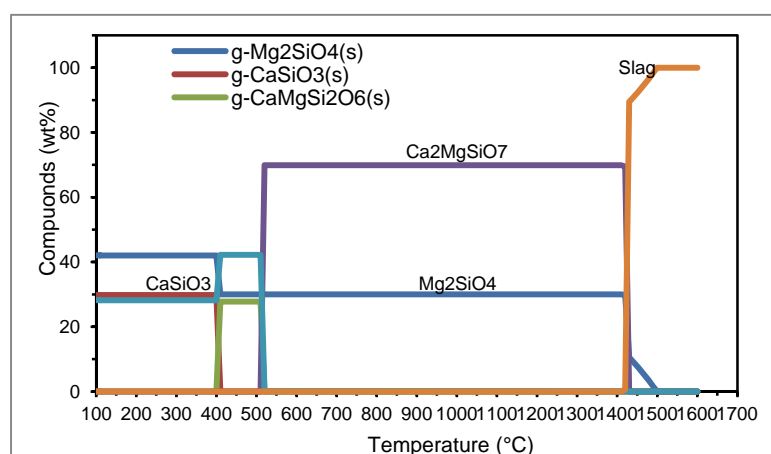


Fig. 3.6 Equilibrium plot of Constitutional Compounds of glass 31 composition calculated by FactSage

B_2O_3 was used to decrease their liquidus temperature and original viscosity. The glass compositions 34 and 35 were modified by adding B_2O_3 from 5–20 wt.%. While the glass composition 37, which its liquidus temperature is low enough to melt, B_2O_3 was added only 5 wt.%. This composition locates at the eutectic point with the lowest liquidus temperature of 1200 °C. The final selected glass compositions for sealing property study are shown in Table 3.6.

Table 3.6 Glass compositions in system Mg–Ca– B_2O_3 – Al_2O_3 – SiO_2

Oxides (wt.%)	SiO_2	Al_2O_3	MgO	CaO	B_2O_3
34	44.2	7.2	17.7	30.9	-
34-5B	42.0	6.8	16.8	29.4	5.0
34-10B	39.8	6.4	15.9	27.8	10.0
34-15B	37.6	6.1	15.0	26.3	15.0
34-20B	35.4	5.7	14.1	24.7	20.0
35	41.0	14.0	19.7	25.3	-
35-5B	38.9	13.3	18.7	24.0	5.0
35-10B	36.9	12.6	17.7	22.8	10.0
35-15B	34.8	11.9	16.7	21.5	15.0
35-20B	32.8	11.2	15.8	20.2	20.0
37	43.6	16.5	10.7	29.2	-
37-5B	41.4	15.7	10.1	27.8	5.0

3.2.2. Glass preparation

The raw materials for melting glass were prepared from reagent grade of oxides, carbonates and silica sand (listed in Appendix A). The mixed powders were melted at 1500 °C for 2 hours in a platinum crucible. The melted glass then was poured in cold water in form of frit. In order to acquire the homogenous glass, the frit was repeated to melt and quench with the same condition. Glass frit was ground in an agate mortar and then sieved through 230 mesh standard sieve (<63 μ m) and 325 mesh standard sieve

(<44 μm). Particle size distribution was examined and analyzed using laser light scattering technique.

The flow chart of overall experiment including thermal characterization, thermal treatments, electrical resistivity measurement, hot-stage microscopy and viscosity measurement, joining test between glass-ceramics/stainless steel, and thermal cycle and gas leak test is shown in Fig. 3.7.

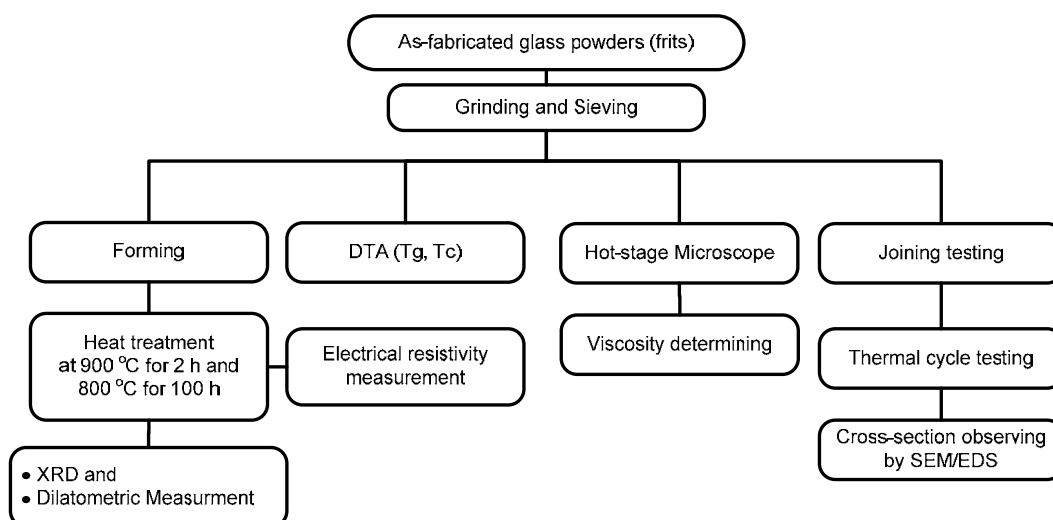


Fig. 3.7 Flow chart of overall experimental procedure in part II from starting glass powders

3.2.3. DTA and dilatometric measurement of glass and glass - ceramics

Powder of glasses with size < 63 μm were characterized their thermal properties in the same experimental procedures as in Part I. Thermal properties including with T_g and T_c were measured using differential thermal analysis (DTA, NETZSCH STA 409, Germany) with a heating rate of 5 K min^{-1} .

Dilatometric measurement was operated by dilatometer. Compacted glass powder (<63 μm) were heat treated at 900 $^{\circ}\text{C}$ for 2 h with heating and cooling rates of 5 K min^{-1} , consequently, it was cut in to 5 mm x 5 mm x 25 mm for investigating CTE.

Furthermore, long term stability of CTE was examined. The sample was continued to soak at 800 °C for 100 h and was investigated the change of CTE.

The crystallized phases of sintered specimens were analyzed by X-ray diffraction.

3.2.4. Hot - stage microscopy experiment

Hot stage microscope (Fig. 3.8) with geometry analysis software (EMI2) was used to calculate the percentage of the decrease in height, width and area of the 2D sample images (shadow). The cylindrical shaped of pressed glass powder with height and diameter approximately 3 x 3 mm was placed on a thin platinum plate with alumina support. The measurement was operated from room temperature to 1300 °C with a heating rate of 5 K min⁻¹. The temperatures corresponding to the characteristic viscosity points (first shrinkage (T_{FS}), maximum shrinkage (T_{MS}), softening (T_D), half ball (T_{HB}) and flow (T_F) were obtained from the taken photographs during the hot-stage microscopy experiment following Scholze's definition and refined by Pascual [111].

The viscosity curves were carried out from Vogel–Fulcher–Tamman (VFT) equation;

$$\log \eta = A + \left(\frac{B}{T - T_0} \right) \quad (3.1)$$

by calculating fixed viscosity values from HSM characteristic points [111]. Where η is viscosity (dP·s) which is related to temperature T (K) or thermal parameter from hot stage microscope. A , B and T_0 are constants.

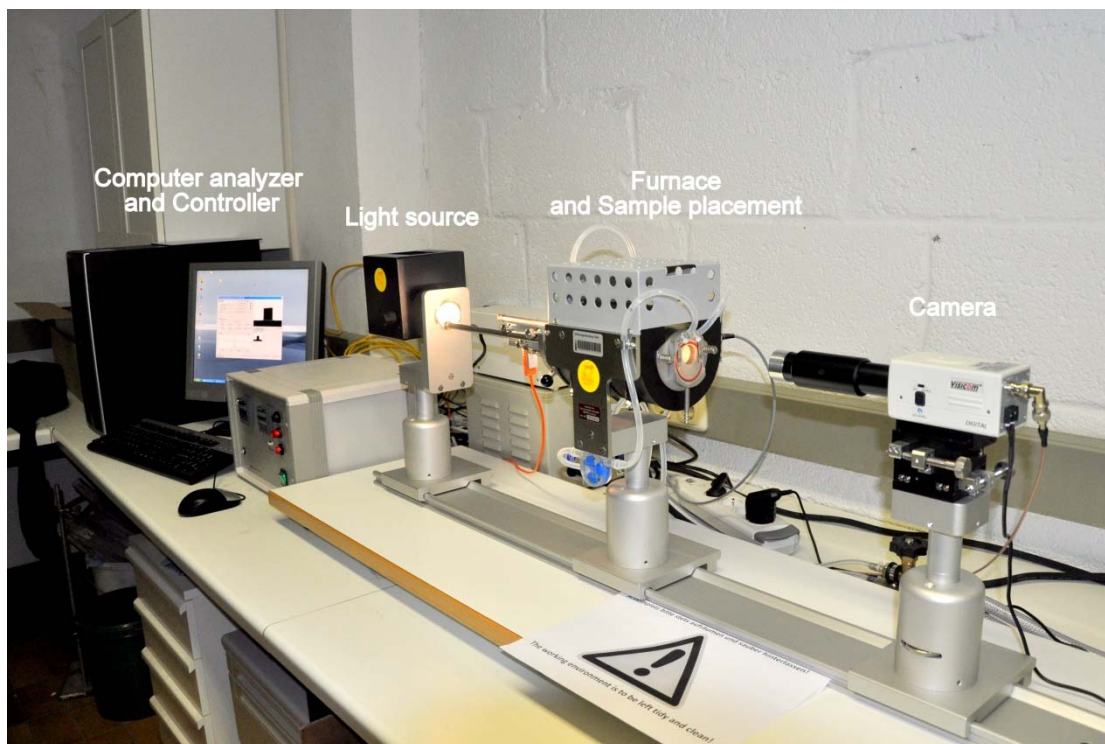


Fig. 3.8 Hot-stage microscopy experimental setup

3.2.5. Joining test

Joining test was started by glass paste preparation. Powder of glass with size less than $<44 \mu\text{m}$ was mixed with the binder solution between ethyl cellulose and terpeneol (raw materials details shown in APPENDIX A). In order to prepare the solution, 5 wt % of ethyl cellulose was solved in a closed glass bottle of terpeneol solution. Then the solution was stirred by using magnetic stirrer and put the bottle in warm water for 24 h. The temperature should not exceed $50 \text{ }^\circ\text{C}$. To make glass powder paste, the glass powder was mixed with 18-25 % of ethyl cellulose and terpeneol solution. The paste was injected through a 2 mm diameter of syringe nozzle on $50 \text{ mm} \times 50 \text{ mm} \times 3 \text{ mm}$ Crofer 22 APU stainless steel (supported by Forschungszentrum Jülich, Germany) as illustrated in Fig. 3.9 (a). The glass paste was dried at room temperature for 1 - 2 days. Then another plate of crofer 22 APU stainless steel was put on top and heated to $900 \text{ }^\circ\text{C}$ for 2 h with slow heating and cooling rate of $3 \text{ K}\cdot\text{min}^{-1}$. The sandwich sample was loaded with 1 kg of refractory brick or about $3.9 \times 10^3 \text{ N}\cdot\text{m}^{-2}$. The same sample was continued to

soak at 800 °C for 100 h. The sandwich sample was cut and ground to investigate their microstructure of cross section and interfacial reaction between glass – ceramics and Crofer 22 APU stainless steel using scanning electron microscope; SEM (JEOL JSM-6400 model) and energy dispersive spectrometry; EDS (OXFORD Instrument ISIS 300).

For joining the glass-ceramic with 8 mol% yttria stabilized zirconia (8YSZ) ceramics, 8YSZ ceramic plates were acquired from MTEC laboratory (National metal and materials technology center). They were prepared from nano particle and sintered at 1250 °C. The glass paste was pasted on it and followed the step in the same way of Crofer 22 APU stainless steel.

3.2.6. Thermal cycle and leak test

Thermal cycle testing were observed by examining gas leak of heat treated sandwich sample, which glass-ceramics were sealed between Crofer 22 APU plates after heat treated each thermal cycle. One of Crofer 22 APU plate was drilled with 1 cm diameter for gas inlet as show in Fig. 3.9(a). Each thermal cycle was started by elevating temperature with 3 K min⁻¹ to 800 °C, dwelling at this temperature for 12 h then cooling down to room temperature with rate of 3 K min⁻¹. Leak test was measured at room temperature. The experimental setup is illustrated in Fig. 3.9(b). Leak rate was measured by monitoring volume change of water level in manometer with time under pressure of 2 psi of Helium gas (99.9995% pure, Praxair (Thailand) Co., Ltd). The calculate leak rate (L) in standard cubic centimeters per minute at STP (sccm) was normalized by outer sealing length. The leak rate of the system without sample (background leak rate) was measured before each test and subtracted from as-measured leak rate.

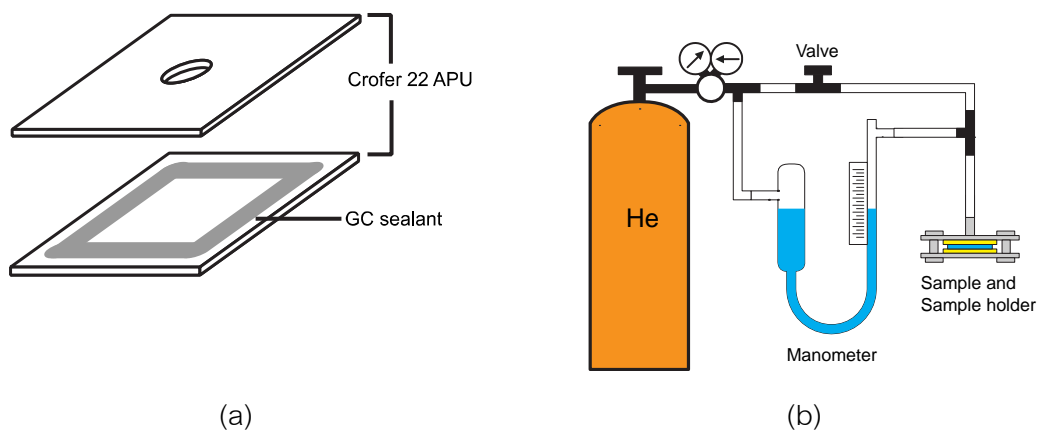


Fig. 3.9 Illustration of (a) test sample assembly of glass-ceramics (GC) sealant and Crofer 22 APU stainless steel plates, (b) gas leak test experimental setup

3.2.7. Electrical resistivity measurement

Electrical resistivity of glass-ceramic sample in this part was processed in the same way as described in section 3.1.7.

CHAPTER 4

RESULTS AND DISCUSSION

4.1 Part I: Development of glass-ceramics sealant in system R_2O -MgO-CaO- Al_2O_3 - Si_2O

4.1.1. Glass selection

The beginning of this research was the selection of glass system to use as the sealant at high temperature. The glass compositions listed in Table 3.1 were prepared by melting at temperature from 1450–1550 °C in a Zircon–mullite crucible in order to study possibility of use a commercial crucible. The results showed the reactions between glass composition and crucible, and the glass could not be completely melted. Then the platinum crucible was used as melting crucible. The glass AZSII and AAS could not be obtained by melting at 1450 °C in platinum crucibles. The glass AZSII could be poured out from the crucible, but there were phase separation with white colors. Another glass composition AAS could not be poured out since the melting temperature was too low to melt this composition. In summary for this step, there were only three glass compositions, which were SACN, CMS1 and CMS2, could be completely melted at 1450 °C. The results are shown in Fig. 4.1. These three compositions contained as high as 10 mol % of Na_2O , which might decrease the properties according to sealing requirements, such as electrical resistivity and chemical reaction with stainless steel. Consequently the glass compositions were designed by varying the amount of alkali oxides in order to study their effects.

Glass composition S1, S2, S3 and S1N were selected from constitutional compound calculation as shown in Table 4.1. The compositions were selected by considering the content of clinoenstatite ($MgO \cdot SiO_2$) which its CTE is $13.5 \times 10^{-6} K^{-1}$ (300–700 °C). The compositions were designed based on the previous three compositions those can be melted at 1450 °C. In this case, Na_2O were decreased and balance with K_2O by 1:1 ratio, in assumption of mixed alkali effect which is able to improve electrical resistivity by replacing Na^+ ion with the larger radius K^+ ion [112]. From the

Constitutional Compound Calculation, the primary crystalline phases of the composition S1, which contained 5 mol % Na_2O and 5 mol % K_2O , were forsterite ($2\text{MgO}\cdot\text{SiO}_2$), nepheline ($\text{Na}_2\text{O}\cdot\text{Al}_2\text{O}_3\cdot 2\text{SiO}_2$) and kaliophilite ($\text{K}_2\text{O}\cdot\text{Al}_2\text{O}_3\cdot 2\text{SiO}_2$). The composition, that was reduced the concentration of alkali oxides (Na_2O and K_2O) to 4 mol% each, clinoenstatite phase ($\text{MgO}\cdot\text{SiO}_2$) was found as the major crystalline instead. Then the calculation result of non-alkali oxide composition S1N showed the highest of clinoenstatite ($\text{MgO}\cdot\text{SiO}_2$) and the second phase was åkermanite ($2\text{CaO}\cdot\text{MgO}\cdot 2\text{SiO}_2$).

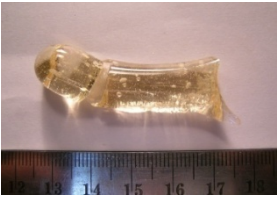
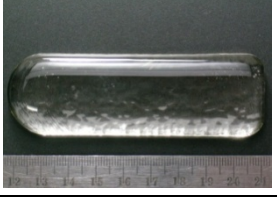
Glass	Melted in Zircon-Mullite crucible		Melted in Pt-crucible
	1450 °C	1550 °C	1450 °C
AZSII			
AAS			Un obtained
SACN			
CMS1			
CMS2	-	-	

Fig. 4.1 As-melted glass from different crucible and temperature

Bismuth was added in glass S3 as fluxing agent, and improvement the CTE. The result of melting experiment showed that all molten glasses could be poured out from the crucible with low viscosity (flow freely), however, the glass was crystallized very quickly. In Fig. 4.2, the pictures of melted glass are shown with their microstructure of crystalline phase by optical microscope. The XRD patterns were confirmed that the separate crystalline phase on glass S1 and S2 was forsterite (Fig. 4.3). Because there is a few of crystalline phases on a surface of small piece of glass sample, no crystalline pattern was found in XRD peak of S2 (Fig. 4.4). But the morphology of crystalline phase in S2, observed by optical microscope, was the same as in S1 glass. Thus it could be implied that the crystalline phase was forsterite.

Table 4.1 Constitutional compound calculation of selected glass composition

Compound	Compositions (wt %)			
	S1	S2	S3	S1N
$K_2O \cdot Al_2O_3 \cdot 6SiO_2$	-	23.64	11.82	-
$K_2O \cdot Al_2O_3 \cdot 2SiO_2$	16.79	-	-	-
$Na_2O \cdot Al_2O_3 \cdot 6SiO_2$	-	29.17	16.92	-
$Na_2O \cdot Al_2O_3 \cdot 2SiO_2$	9.99	-	-	-
$MgO \cdot SiO_2$	-	57.28	41.35	58.69
$2MgO \cdot SiO_2$	43.63	-	15.65	5.39
$CaO \cdot MgO \cdot 2SiO_2$	-	-	2.30	4.54
$2CaO \cdot MgO \cdot 2SiO_2$	-	-	-	31.38
$CaO \cdot Al_2O_3 \cdot 2SiO_2$	-	-	6.94	-

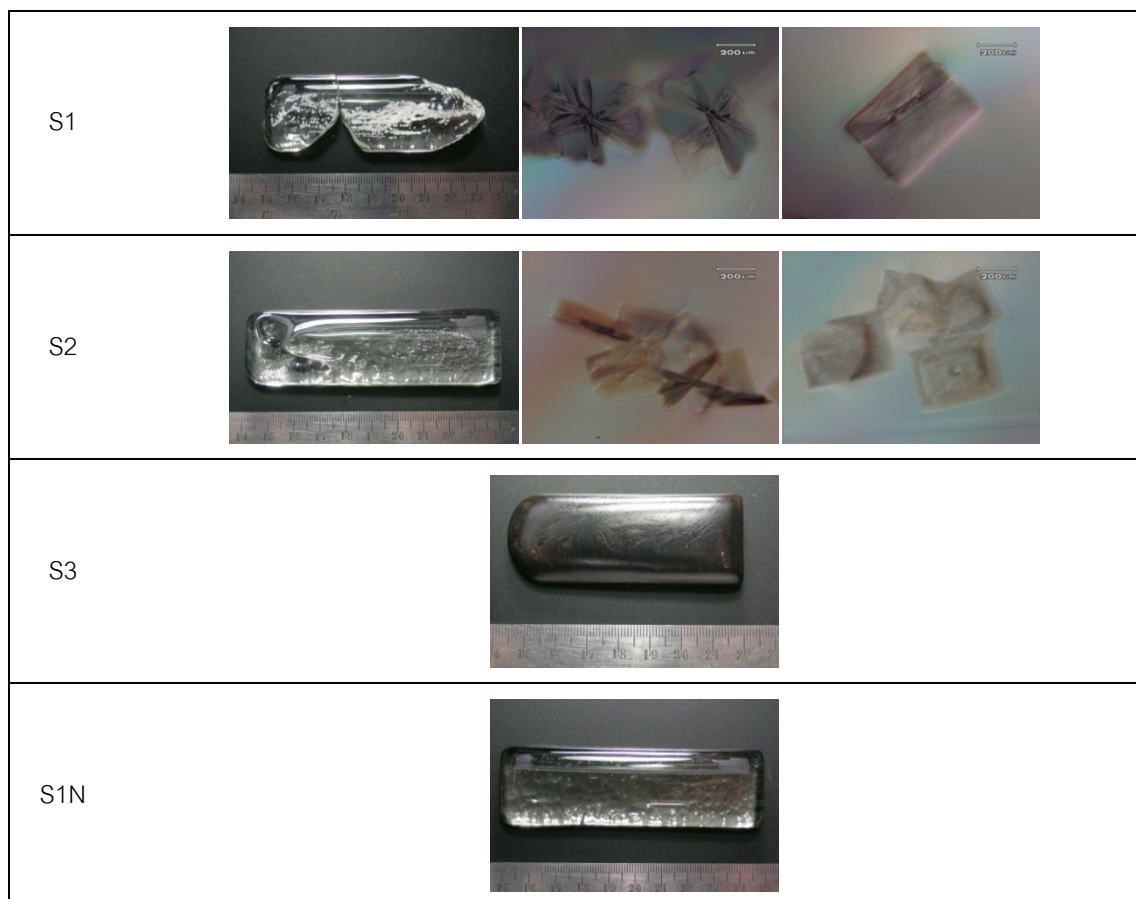


Fig. 4.2 As – melted glass after melted at 1500 °C, 2 h in platinum crucible

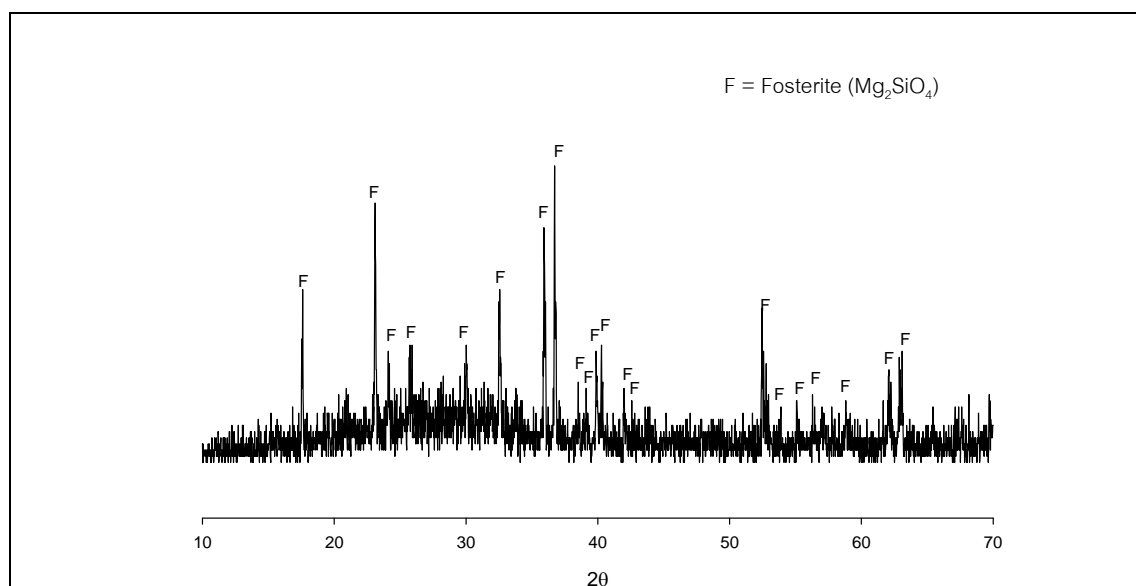


Fig. 4.3 X-ray diffraction pattern of containing crystalline phase glass piece S1

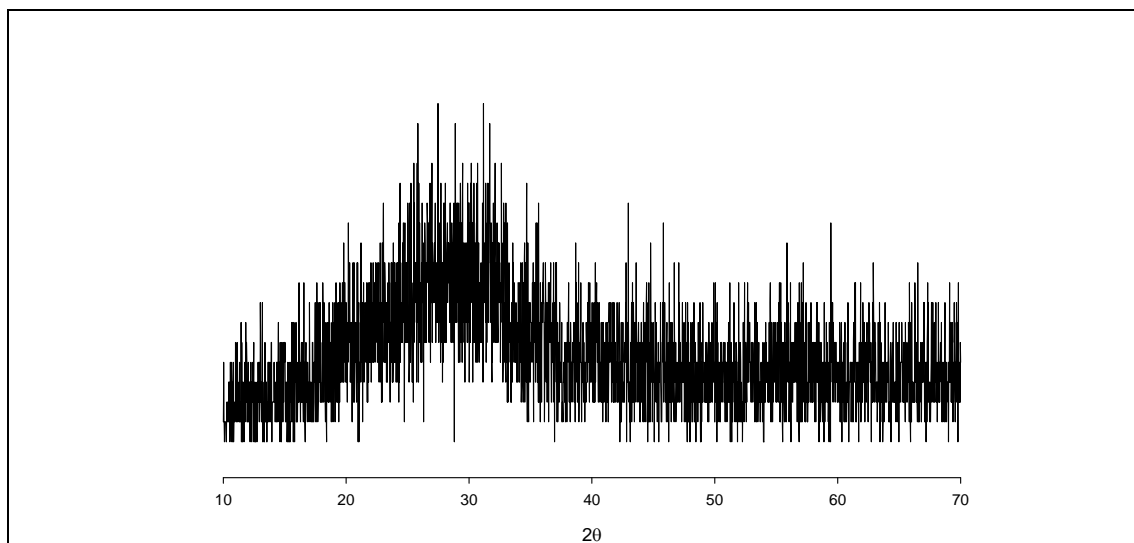


Fig. 4.4 X-ray diffraction pattern of containing crystalline phase glass piece S2

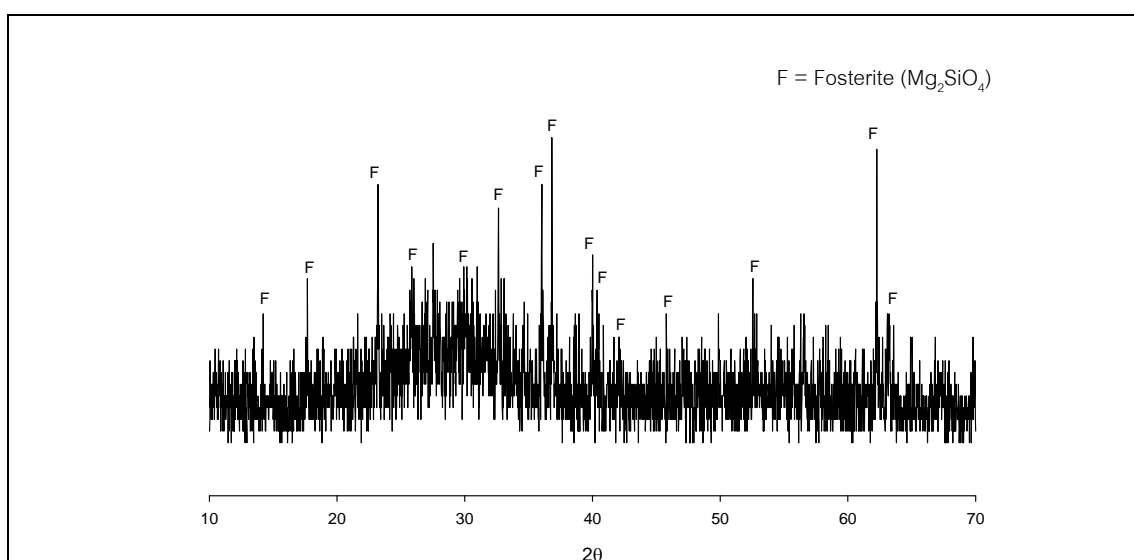


Fig. 4.5 X-ray diffraction pattern of containing crystalline phase glass piece S3

From above, there were four glass compositions, which were completely melted. Their glass transition temperature (T_g) and crystallization temperature (T_c) are showed in Table 4.2. Two crystallization peaks of T_c (T_{c1} and T_{c2}) were found in all glass compositions, it meant that crystallization of different phase was observed. XRD patterns of sintered glass (glass-ceramics) could be used to confirm the system of crystalline phases. The identified crystalline phases in glass-ceramics after heat treated glasses at 900 °C, 2 h, are shown in Table 4.3. Nepheline was found as major crystalline phase

with diopside ($\text{CaMgSi}_2\text{O}_6$) and wollastonite (CaSiO_3) in the glass-ceramics containing around 10 mol % Na_2O (S1, S2 and SACN).

Table 4.2 Differential thermal analysis of as-melted glasses

Glass	T_g ($^{\circ}\text{C}$)	T_{c1} ($^{\circ}\text{C}$)	T_{c2} ($^{\circ}\text{C}$)
CMS1	654	740	824
CMS2	640	748	834
SACN	684	777	847
S1N	742	836	924

Table 4.3 Detected crystalline phases in glass-ceramics after sintered at 900 $^{\circ}\text{C}$, 2 h, obtained by XRD.

Crystalline phase	CMS1	CMS2	SACN	S1N
Nepheline	X	X	X	-
Diopside	X	X	-	X
Forsterite	-	-	-	X
Wollastonite	-	-	X	-

Thermal expansion of glass-ceramics sample after sintered at 900 $^{\circ}\text{C}$, 2 h are shown in Table 4.4. The CTE of AISI430 stainless steel is also measured to compare with sintered glass. After sintered, crystallized S1N glass show the lowest CTE, which is out of range of requirement (should be $9\text{--}13 \times 10^{-6} \text{ K}^{-1}$).

In conclusion of glass selection, the glass composition base on CMS1, CMS2 and SACN were selected to improve and study other properties in the further experiments.

Table 4.4 Thermal expansion of sintered glass at 900 °C for 2 h using dilatometer comparison of AISI430 stainless steel

Sample	CTE ($\times 10^{-6} \text{ K}^{-1}$) (50-600°C)
CMS1	12.47
CMS2	12.80
SACN	12.91
S1N	8.68
AISI430 stainless steel	11.97

4.1.2. Preparation of glasses in CM1 and CM2 series

Glass composition close to CMS1, CMS2 and SACN were divided into two series, which are CM1 and CM2. Then the alkali oxides, which are Na_2O and K_2O were varied from 0, 5 (mixed), and 10 mol %. The compositions are listed in Table 3.3. All compositions were completely melted at 1450 °C, 2 h in a platinum crucible. The crystalline or undissolved phase was not found in bulk glass. The powders of glasses were prepared and their particle size distributions are shown in Table 4.5. The median of particle size (d_{50}) of glasses were between 31 – 41 μm .

Table 4.5 Particle size distribution of glass powder

Glass	Particle size distribution (μm)	
	d_{50}	d_{90}
CM11	39.525	86.153
CM12	35.512	67.349
CM13	41.362	90.451
CM14	31.146	59.132
CM21	36.161	78.694
CM22	34.356	69.771
CM23	34.732	55.651
CM24	34.634	73.889

4.1.3. Thermal properties of glass and glass-ceramics in CM1 and CM2 series

The thermal properties of glass and glass-ceramics are shown in Fig. 4.6. The results showed that the T_g and T_d of all glasses were in range that be possible to use as sealant, which T_d was lower than 800 °C. It should become soft enough for joining at 900 °C.

Table 4.6 Thermal properties including T_g , T_c , T_d (°C) and CTE ($\times 10^{-6} \text{ K}^{-1}$) of bulk glass and glass-ceramics (after sintered at 900 °C, 2h) in CM1 and CM2 series.

Thermal Properties	CM11	CM12	CM13	CM14	CM21	CM22	CM23	CM24
T_g by Dilatometer	730	714	653	642	640	595	636	647
T_g by DTA	724	727	654	667	730	625	640	684
T_c by DTA	828	817	740	862	925	847	748	892
T_d by Dilatometer	785	776	709	717	777	651	688	719
CTE (bulk glass)	7.45	7.88	11.5	11.21	7.21	11.68	10.4	10.27
CTE (900 °C, 2h)	8.72	8.52	12.98	13.83	8.71	12.55	13.28	14.19

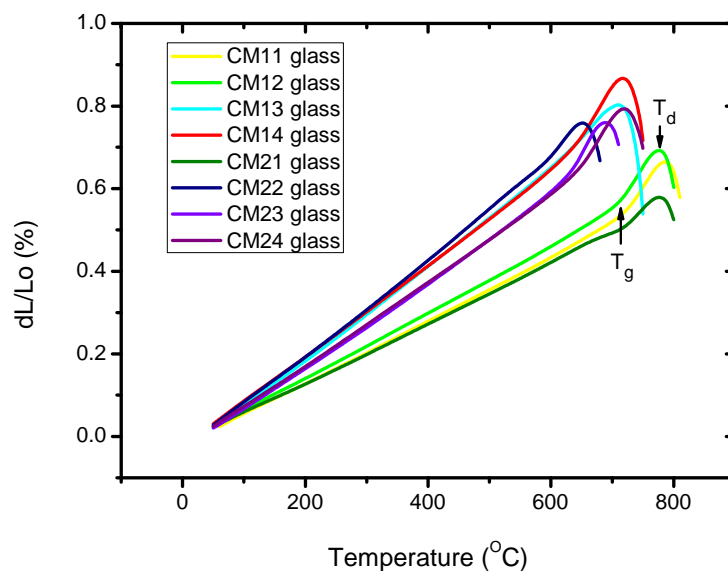


Fig. 4.6 Dilatometric curves of glasses in CM1 and CM2 series

In order to compare the effect of 5 mol% single alkali oxide (Na_2O and K_2O) and mixed alkali oxide addition on T_g and T_d , the data are plotted in Fig. 4.7 and Fig. 4.8. The

result showed that single alkali oxide in CM13 and CM14 reduced T_g and T_d . Mixed alkali oxide in CM12 also had an effect on T_g and T_d . In case of CM2 series, alkali oxides also decrease T_g and T_d of glass in the series. The mixed alkali oxides in this series showed more effect more than single alkali oxide as shown in Fig. 4.8.

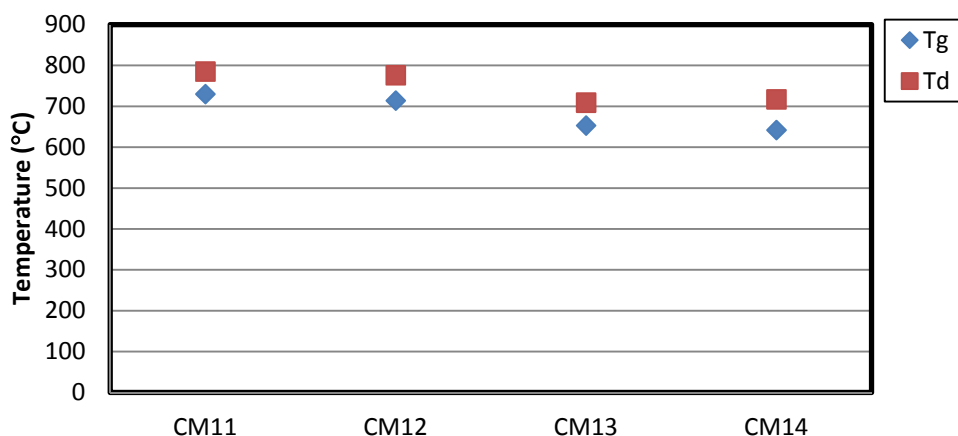


Fig. 4.7 Comparison of T_g and T_d of bulk glass CM1 obtained by dilatometer

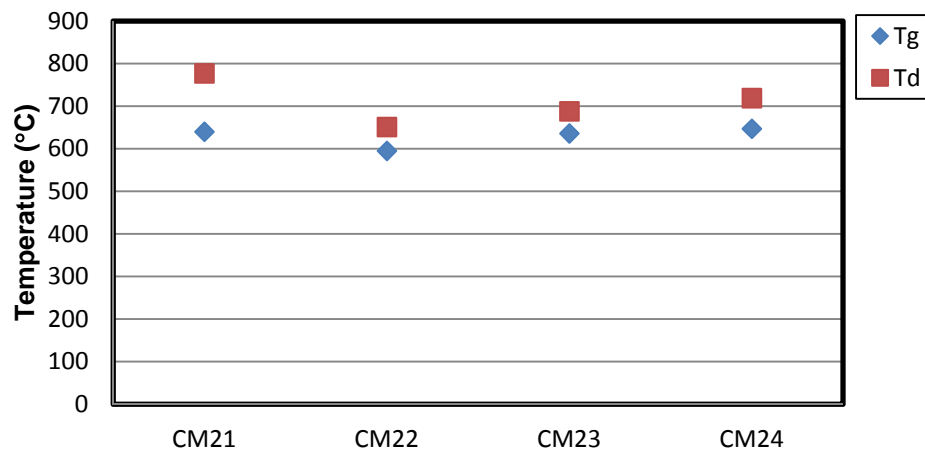


Fig. 4.8 Comparison of T_g and T_d of bulk glass CM2 obtained by dilatometer

The CTEs of as melted-glasses in case of alkali-free glass composition CM11 and CM21 were the lowest in their series. In CM1 series, the CTE of glass compositions with mixed alkali oxides CM12 were higher than alkali free composition, but the composition, with

10 mol% Na₂O, CM13 showed the highest CTE in this series as $11.5 \times 10^{-6} \text{ K}^{-1}$. While mixed alkali oxide composition CM22 showed the highest CTE in their series. The CTEs of all glasses increased after sintering at 900 °C for 2 h. The CM13 composition showed the CTE in range of requirement, which is $9 - 13 \times 10^{-6} \text{ K}^{-1}$. The CM14 and CM24 compositions, which were containing 10 mol% of K₂O, perform the highest CTE after sintered at 900 °C for 2 h. Their CTEs were slightly higher than requirement. The crystallization temperature of glass compositions those containing 10 mol % Na₂O were the lowest in their series. It could be explained that glass containing Na₂O, which was a network modifier in silicate glass structure, decreased its T_g and viscosity. In general, the crystallization easily occurred in low viscosity glass; consequently, the nucleation of crystalline phases took place easier in this case.

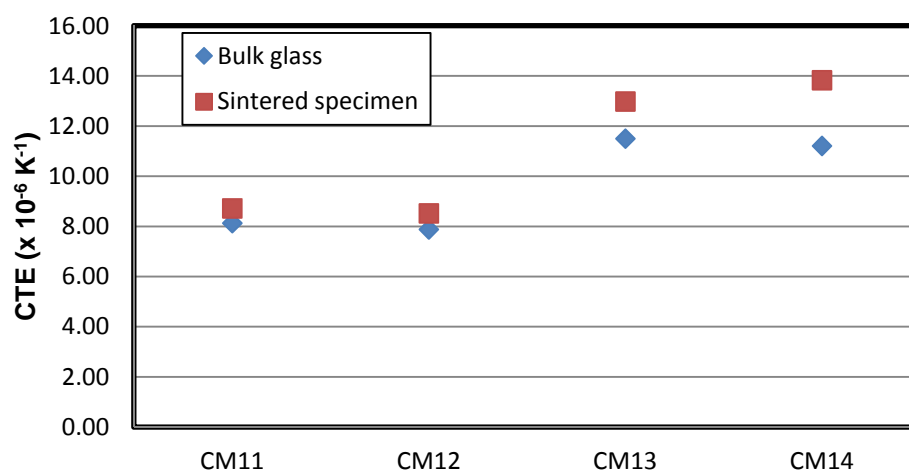


Fig. 4.9 Comparison of CTE of bulk glass CM1 obtained by dilatometer

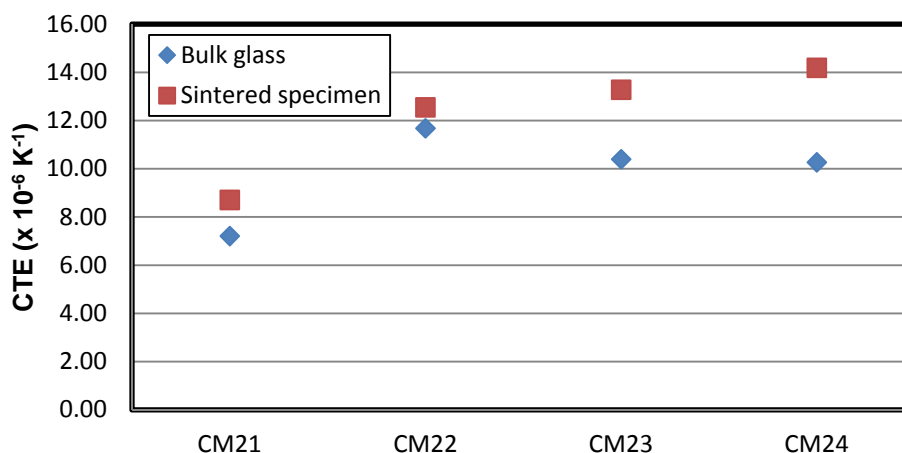


Fig. 4.10 Comparison of CTE of bulk glass CM2 obtained by dilatometer

4.1.4. Dilatometric result and crystallization behavior of heat treated glass-ceramics in CM1 and CM2 series

4.1.4.1. Dilatometric result of glass-ceramics after heat treatments

Table 4.7 are the CTE of glass, glass-ceramics obtained by heat treated at 900 °C for 2 h, and continue heat treated at 800 °C for 10 h. The dilatometric curves were plotted in Fig. 4.11. Although CTEs of glass-ceramics of non-alkali oxide (CM11 and CM21), were higher than that of glassy, their CTE, were still lower than that requirement of $9\text{--}13 \times 10^{-6} \text{ K}^{-1}$. While the CTEs of 10 mol% K_2O samples, CM14 and 24 after longer heat treatment process were higher than $13 \times 10^{-6} \text{ K}^{-1}$. The crystalline phases were detected and discussed in next section. The glass-ceramics of 10 mol% Na_2O CM13 and CM23 seemed compatible with AISI430 stainless steel and YSZ because the CTE was in range close to $13 \times 10^{-6} \text{ K}^{-1}$ even after heat treated at 800 °C, 10 h. In case of mixed alkali oxides glass-ceramics, it was found that the CTE of glass-ceramics CM22 was close to the stainless steel and YSZ. Consequently, the CM13, CM22 and CM23 were selected to study the possibility for sealing in SOFC.

Table 4.7 CTE of glass and heat treated glass–ceramics with different condition ($\times 10^{-6} \text{ K}^{-1}$, range 100 – 600 °C)

Conditions	CM11	CM12	CM13	CM14	CM21	CM22	CM23	CM24
Bulk glass	8.13	7.88	11.5	11.21	7.21	11.68	10.4	10.27
GC-900°C, 2h	8.72	8.52	12.98	13.83	8.71	12.55	13.28	14.19
GC-900°C, 2h + 800°C, 10h	8.70	8.20	12.45	15.82	8.70	13.17	13.11	15.26

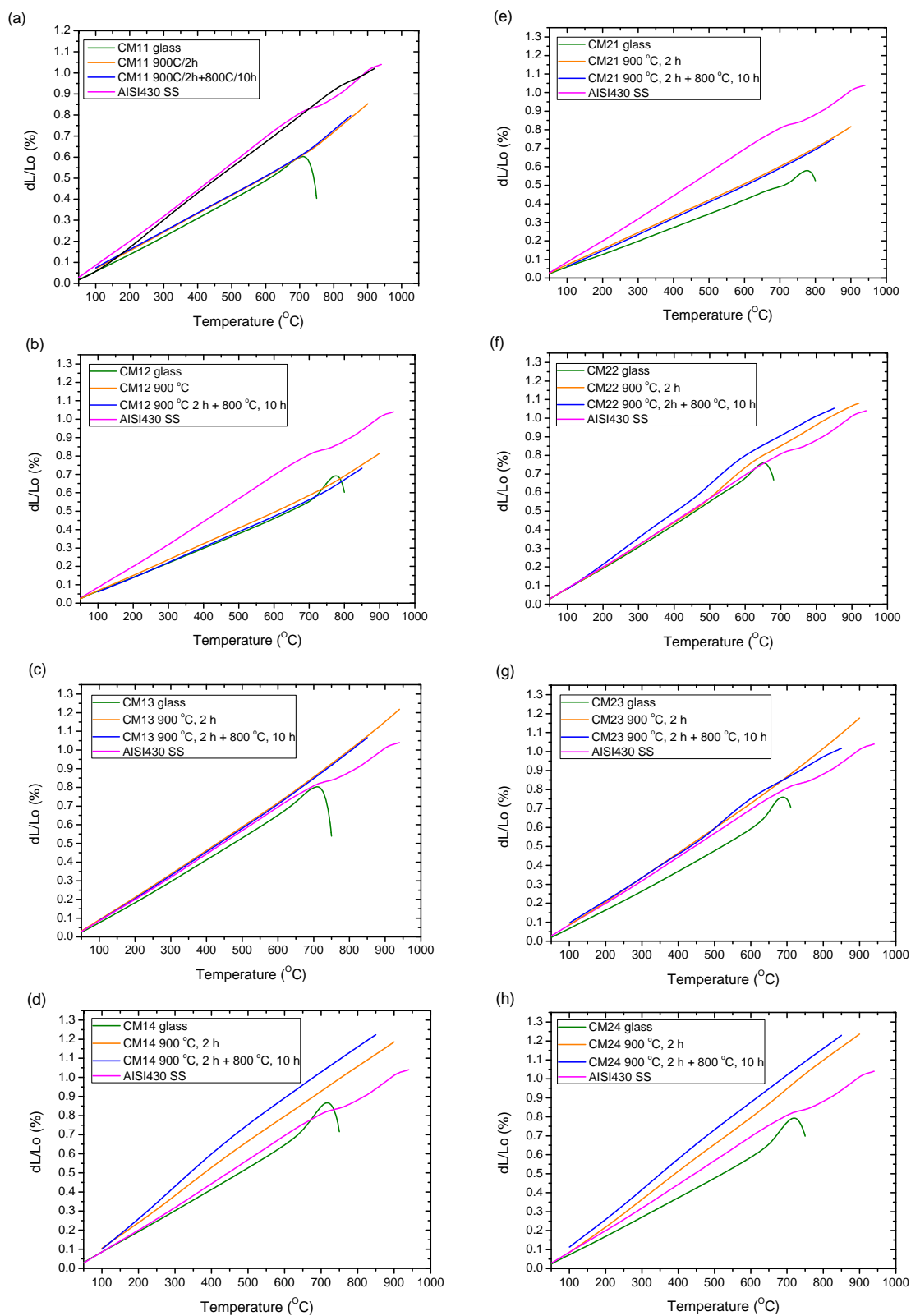


Fig. 4.11 Comparison of dilatometric curves of glass and glass-ceramics with different heat treatment condition

4.1.4.2. Crystallization Behavior

The crystallization of heat treated glass-ceramics at 900°C for 2 h was investigated by XRD. The results show in Table 4.8. It could be summarized that formation of nepheline ($\text{NaAlSi}_3\text{O}_8$) and kaliophilite (KAlSi_3O_8) phases were found with the addition of Na_2O and K_2O in these glass systems while diopside crystalline phase was only found as the major crystalline phase in mixed both alkali oxide glass-ceramics CM12 compositions. The Na and K played a role in increasing CTE of glass-ceramics in this system. According to dilatometric results, it implied that kaliophilite crystalline phase in glass-ceramics gave an increase of CTE greater than that of nepheline phase. The CTE of nepheline glass-ceramics was reported as high as $16.4 \times 10^{-6} \text{ K}^{-1}$ [113-114], while CTE of kaliophilite glass-ceramics was $21.68 \times 10^{-6} \text{ K}^{-1}$ [115-116]. The other detected crystalline phases in the glass-ceramics, which their CTEs were higher than $9 \times 10^{-6} \text{ K}^{-1}$ were forsterite ($9.4 \times 10^{-6} \text{ K}^{-1}$), åkermanite ($10.8 \times 10^{-6} \text{ K}^{-1}$), clinoenstatite ($7\text{-}13.5 \times 10^{-6} \text{ K}^{-1}$) and gehlenite ($9.4 \times 10^{-6} \text{ K}^{-1}$). All of these were acceptable since their CTEs were not much different than that of other crystalline phases. The diopside ($5 \times 10^{-6} \text{ K}^{-1}$) crystalline phase found in glass-ceramics CM11 and CM12 was the cause of their low CTE in their crystallized form as glass-ceramics.

Table 4.8 Crystalline phases of glass-ceramics after sintered at 900°C for 2 h obtained by XRD pattern

XRD results	CM11	CM12	CM13	CM14	CM21	CM22	CM23	CM24
Diopside ($\text{CaMgSi}_2\text{O}_6$)	X	X	-	-	-	-	X	-
Clinoenstatite (MgSiO_3)	X	-	-	X	X	-	-	X
Åkermanite ($\text{Ca}_2\text{Mg}(\text{Si}_2\text{O}_7)$)	-	-	X	-	-	X	-	-
Nepheline ($\text{NaAlSi}_3\text{O}_8$)	-	-	X	-	-	X	X	-
Forsterite (Mg_2SiO_4)	-	-	-	-	-	-	X	-
Gehlenite ($\text{Ca}_2\text{Al}_2\text{SiO}_7$)	-	-	-	X	-	-	-	-
Kaliophilite (KAlSi_3O_8)	-	-	-	X	-	-	-	X

4.1.5. Electrical properties

The electrical resistivity of the sintered pellets of all glass compositions were investigated by using AC-Impedance Analyzer. The Impedance spectra of glass-ceramics sample in CM1 and CM2 series are shown in Fig. 4.12 and Fig. 4.13 respectively.

In ceramics especially semiconductor ceramics, there were two first semicircles corresponding to bulk resistivity (arc at high frequency) and grain boundary resistivity (arc at middle frequency next to bulk resistivity), respectively [117-118]. For glass and glass-ceramics, the grain boundary was absence or very low in case of fully crystallized glass, consequently, only first semi-circle of impedance spectra was found referring to bulk resistivity. The electrical resistivity of glass-ceramics in this work was considered in term of total resistivity (ρ_t).

The electrical resistivity was obtained from total resistivity from semi-circle spectra, which was extrapolated to real part axis (Z') from Nyquist plot. The electrical resistivity of glass was decreased by increasing temperature from 600 to 800 °C because the alkali ions such as Na^+ ion and K^+ ion could move easier in the glass and grain boundary at high temperature. The electrical resistivity of glass-ceramics in CM1 series showed that the glass-ceramics containing 10 mol % K_2O (CM14) had the higher electrical resistivity than mixed alkali-oxides (CM22) and 10 mol % Na_2O . However, it was slightly less than that of alkali free glass-ceramics CM11. On the other hand, the electrical resistivity of the glass-ceramics with 10 mol % Na_2O (CM24) was lower than alkali free glass-ceramic (CM21). Glass-ceramics CM11 was also the highest electrical resistivity at all temperatures among all glass compositions in both series.

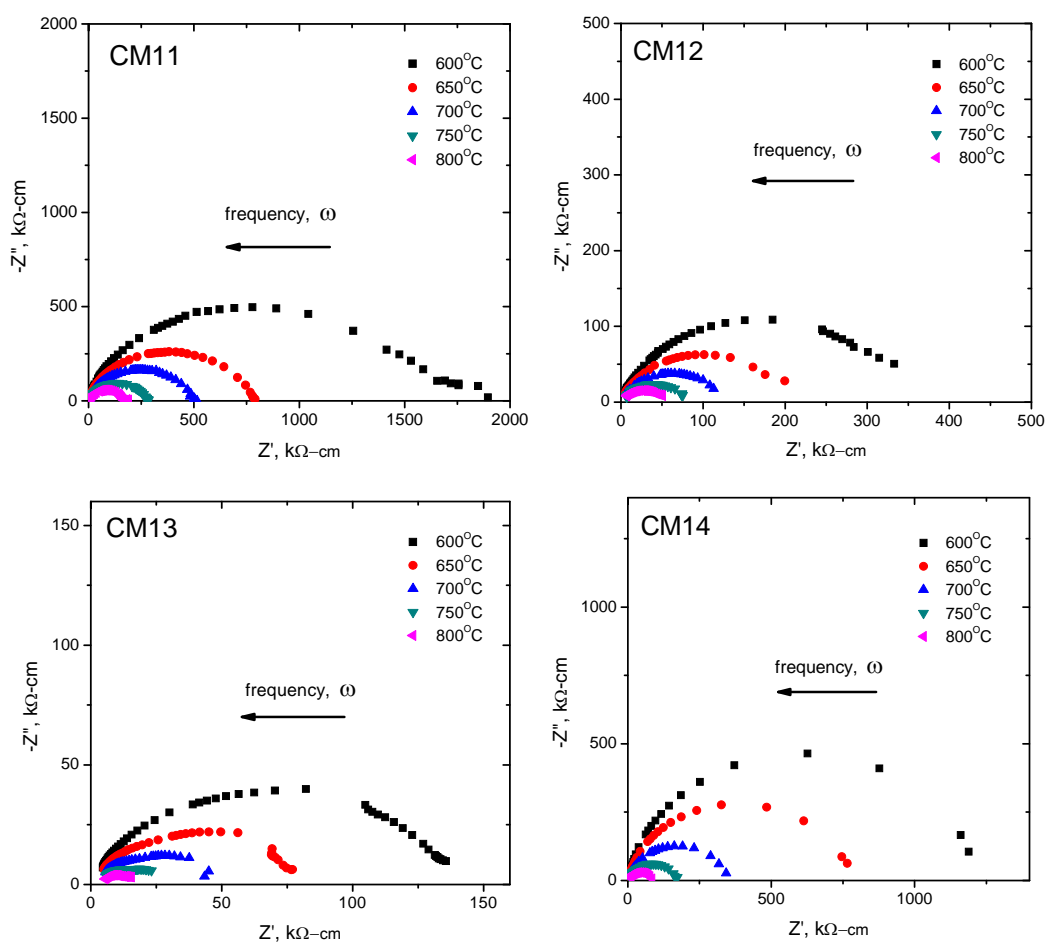


Fig. 4.12 Impedance spectra , in Nyquist diagram form, of all glass-ceramics in CM1 series at different temperature.

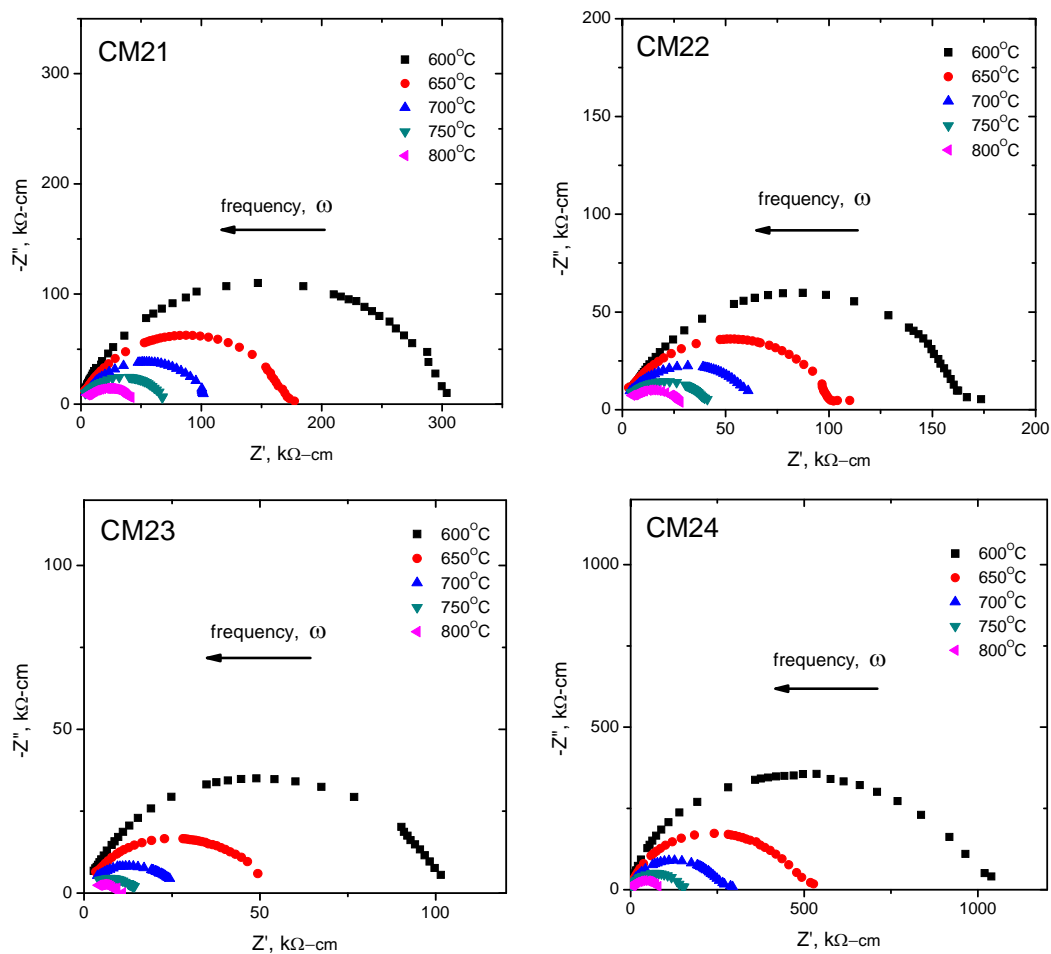


Fig. 4.13 Impedance spectra, in Nyquist diagram form, of glass-ceramics in CM2 series at different temperature.

The total resistivity (ρ_t) of glass-ceramics can be illustrated as an Arrhenius relation [119] below.

$$\rho_t = \rho_o \exp\left(\frac{E_a}{kT}\right) \quad (4.1)$$

Where E_a is activation energy, ρ_o is constant, k is the Boltzmann constant, and T is the temperature of measurement. From this equation E_a is derived from the slopes of the linear range of the log Resistivity (ρ_t vs. $1000/T$). The Arrhenius curves of glass-ceramics in CM1 series and CM2 series are plot in Fig. 4.14 and Fig. 4.15.

Table 4.9 Electrical resistivity of glass–ceramics at 600–800 °C

Temperature (°C)	Resistivity $k\Omega\text{-cm}$							
	CM11	CM12	CM13	CM14	CM21	CM22	CM23	CM24
600	1555.54	360.80	140.68	1253.82	294.16	174.82	97.96	993.30
650	763.90	203.02	90.18	660.40	185.78	112.50	59.04	481.80
700	495.30	122.50	56.58	325.00	105.24	63.34	25.68	253.78
750	286.52	83.78	37.74	171.00	79.00	40.64	14.88	138.22
800	170.06	56.04	19.74	89.60	46.74	29.34	11.22	78.30

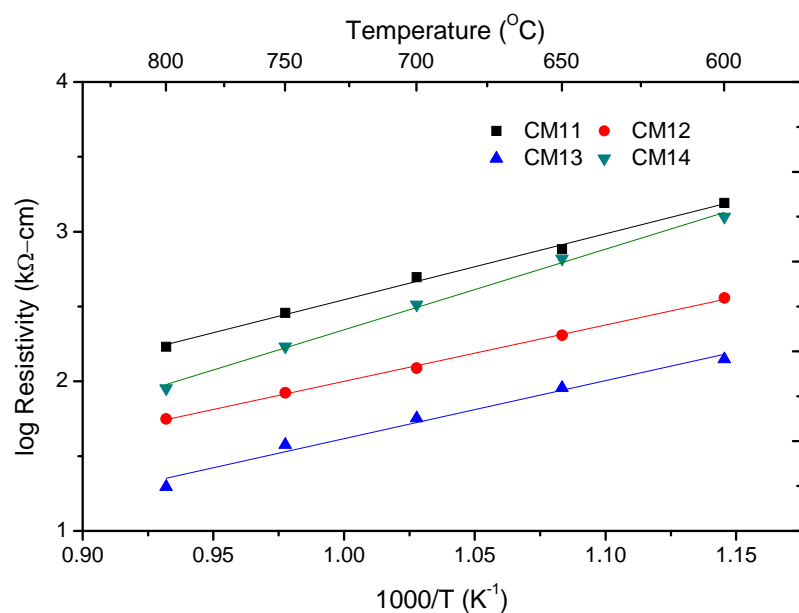


Fig. 4.14 Arrhenius plots of log resistivity vs. $1000/T$ of glass-ceramics in CM1 series at temperature between 600 – 800 °C.

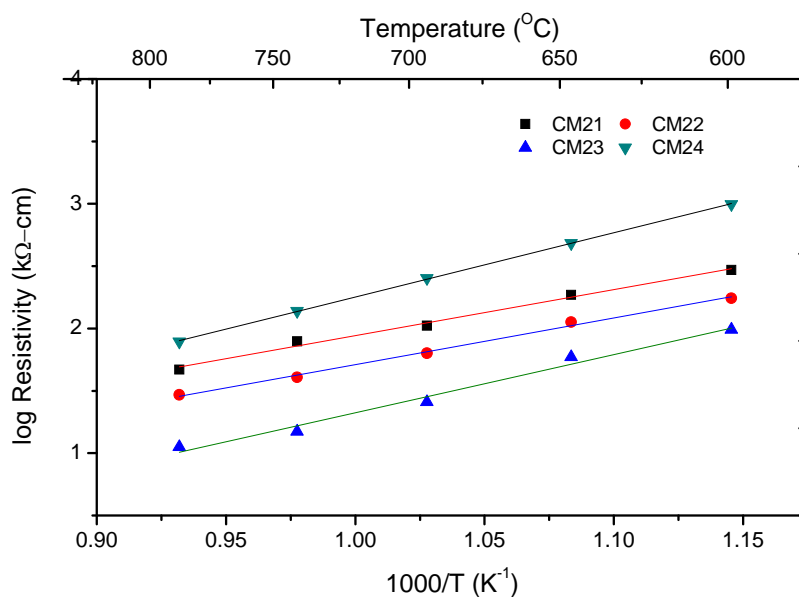


Fig. 4.15 Arrhenius plots of log resistivity vs. $1000/T$ of glass-ceramics in CM2 series at temperature between 600 – 800 °C.

The activation energies of glass-ceramics are shown in Table 4.10. The glass-ceramics containing 10 mol % K_2O in both series performed the highest E_a in their series. E_a of CM14 and CM24 were higher than other glass-ceramics in the same series. It could explain that E_a of CM14 and CM24 was caused by the large dimension of K^+ . Compared the atomic radius of each metal ions, the size of $K^+ > Na^+$. The electrical conductivity in glass is caused by conducting of metal ions especially alkali ions [101]. Mg^{2+} is a conducting ion as well as K^+ since their atomic radius and ionic mobility are comparable. In case of CM21, it found that the resistivity is slightly lower than CM24, which contains 10 mol% K_2O . It could be concluded that the higher amount of Mg^{2+} in CM21 composition could be conducting in this glass-ceramics at high temperature.

Table 4.10 Activation energy of glass-ceramics at temperature 600 – 800 °C

Glass-ceramics	CM11	CM12	CM13	CM14	CM21	CM22	CM23	CM24
E_a (eV)	0.87	0.75	0.77	1.07	0.73	0.74	0.93	1.02

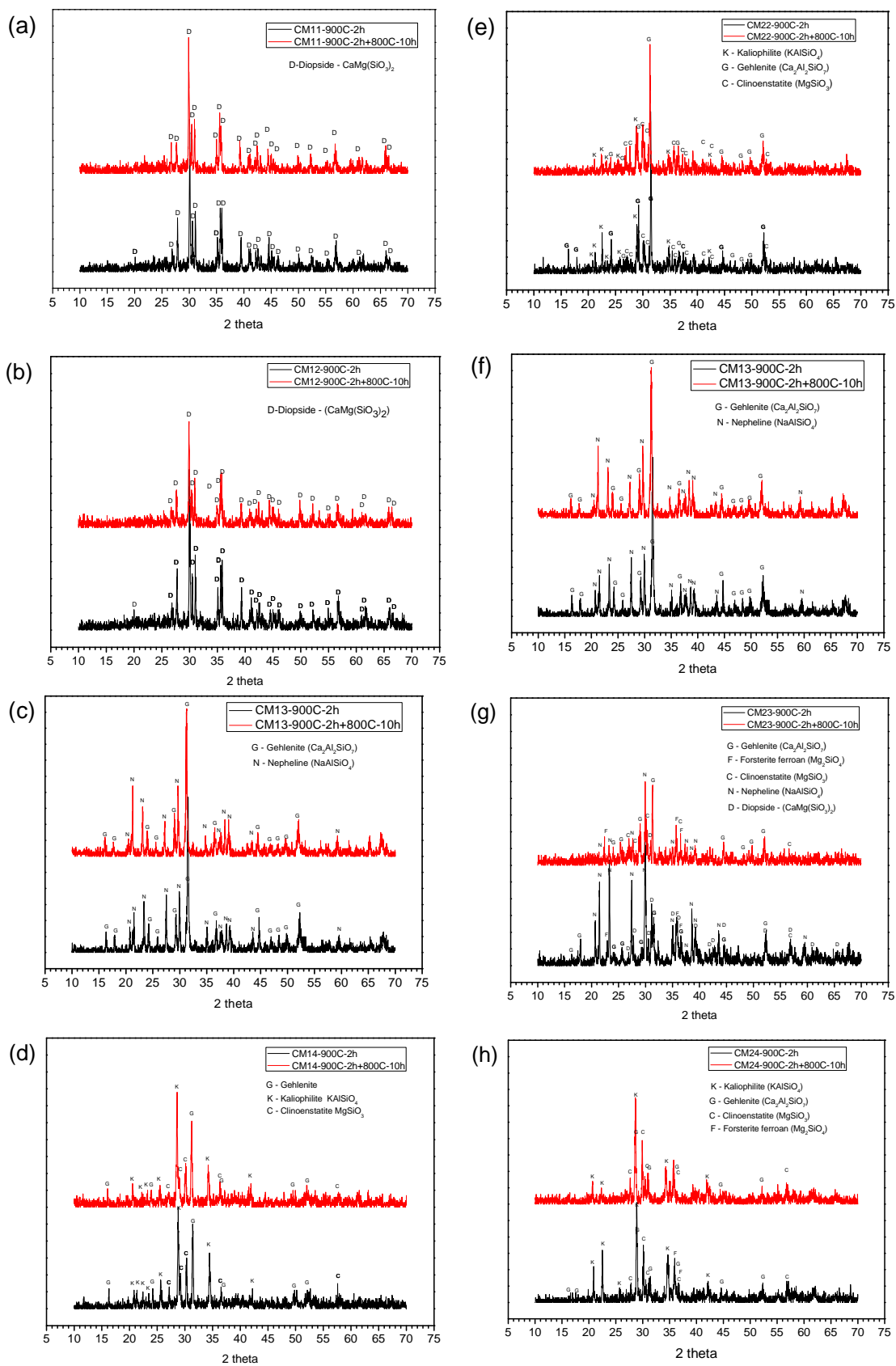


Fig. 4.16 XRD-patterns of glass-ceramics after heat treated by different condition

4.1.6. Joining test between glass–ceramics and AISI430 stainless steel

Joining test sample preparation was assembled of glass-ceramics layer in-between a couple of AISI430 stainless steel as sandwich like specimen. The glass paste was applied between AISI430 stainless steel (50 x 25 x 0.4 mm). In this experiment the glass paste was prepared from mixing of 1 wt.% PVA solution and glass – powders (< 63 μm). The portion of 65 -70 % solid was appropriate to become a good viscous paste for pasting on the surface. After dried the paste in room temperature, the sandwich specimen was heated up to joining temperature at 900 $^{\circ}\text{C}$, 2 h. Cross-sectional microstructure of only joined specimens was observed. The result found that CM11 and CM21, non alkali containing, could not joined with the stainless steel. In case of alkali containing composition, it was found that all composition except CM12 could be attached between AISI430 stainless steel. The joining test results are summarized in Table 4.1. From this table, it could be concluded that the glass–ceramics with CTE lower than $9 \times 10^{-6} \text{ K}^{-1}$ were unacceptable to use for joining with the stainless steel. For the sandwich specimens, it was found that the CTE of glass–ceramics are in range between 12 and $14 \times 10^{-6} \text{ K}^{-1}$. It correlates to CTE of AISI430 stainless steel, which is $11.97 \times 10^{-6} \text{ K}^{-1}$.

SEM image of the interface between glass–ceramics and AISI430 stainless steel are shown in Fig. 4.17. The EDS line scan was taken to investigate the ionic diffusion of Cr and Fe to form Cr_2O_3 and $\text{FeO}/\text{Fe}_2\text{O}_3$ at the interface are shown in Fig. 4.18 - Fig. 4.22. From these figures, the high concentration of Cr and Fe ion were found at the interface layers between AISI430 stainless steel and glass-ceramics CM13 and CM23. The height of layer were approximately 60 (Fig. 4.18) and 100 μm (Fig. 4.22). The thinner layers of Cr and Fe oxides approximately 10 (Fig. 4.19) and 50 μm (Fig. 4.22) were also found in case of CM14 and 24. In case of mixed oxide CM22, the EDS line scan pictures show sharper interface between glass ceramics. It seemed that mixed alkali oxides decreased the corrosion rate on the stainless steel interface. The penetration of ions from glass-ceramics, including Ca, Mg, Al, Si, Na and K, into the AISI430 stainless steel matrix was not observed in all cases.

Considered bonding between the interfaces, the cracks were found in the glass-ceramics instead at the interface as shown in Fig. 4.17 (b), (c) and (d) since the CTE mismatch between glass-ceramics and the stainless steel. It could be implied that adhesion force between glass-ceramics and AISI430 stainless steel was higher than the cohesion force of inner glass-ceramics bond.

Table 4.11 Joining test between glass–ceramics and AISI430 stainless steel at 900 °C, 2 h compare with CTE of glass and glass–ceramics

Paste sample	CTE (100-600°C), $\times 10^{-6} \text{ K}^{-1}$		Joining test
	Bulk glass	GC 900°C, 2 h	
CM11	8.13	8.72	✘
CM12	7.88	8.52	✘
CM13	11.5	12.98	✓
CM14	11.21	13.83	✓
CM21	7.21	8.71	✘
CM22	11.68	12.55	✓
CM23	10.4	13.28	✓
CM24	10.27	14.19	✓

Note: ✓ = attached, ✘ = detached

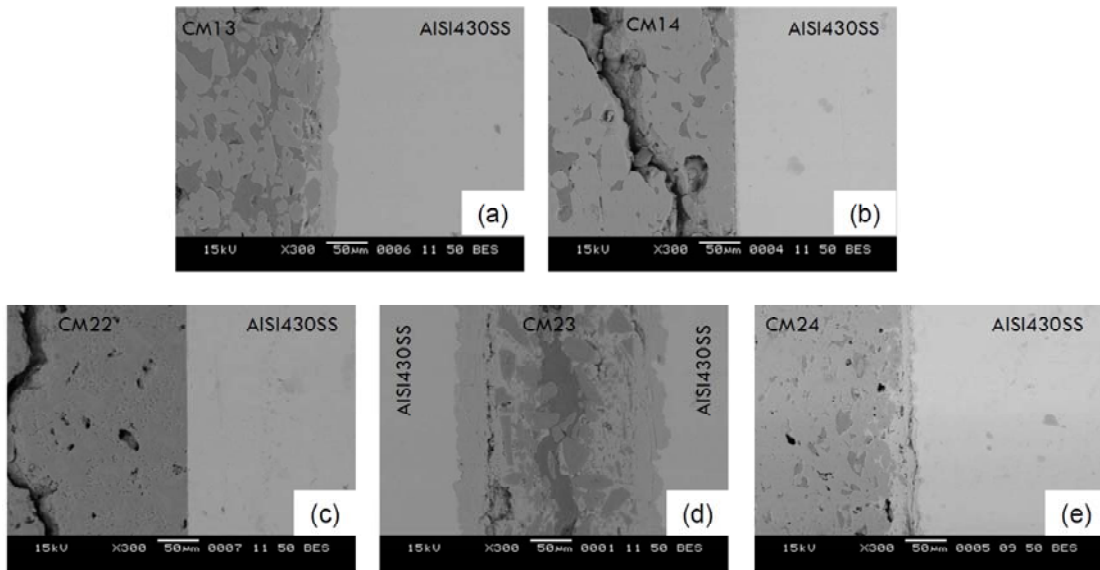


Fig. 4.17 Cross section of glass–ceramics and AISI430 stainless steel after joining at 900 °C, 2 h

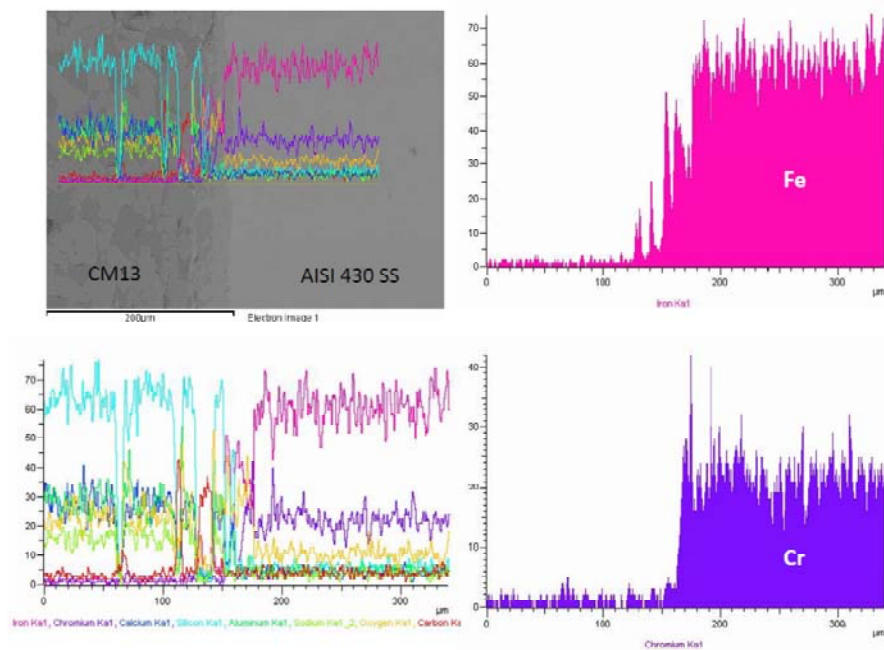


Fig. 4.18 EDX line scan across interface between CM13 glass–ceramics and AISI430 stainless steel

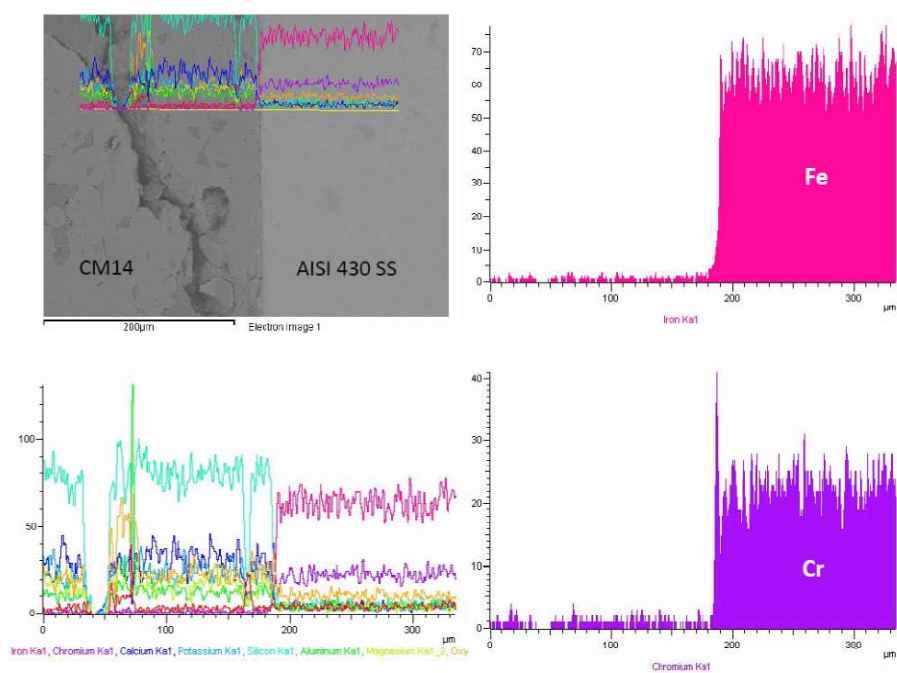


Fig. 4.19 EDX line scan across interface between CM14 glass–ceramics and AISI430 stainless steel

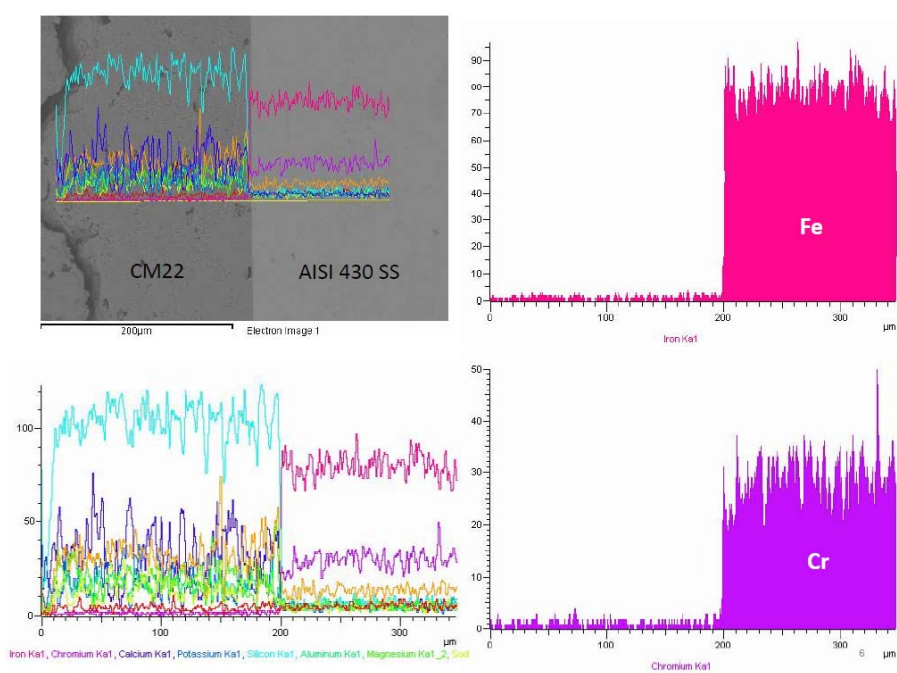


Fig. 4.20 EDX line scan across interface between CM22 glass–ceramics and AISI430 stainless steel

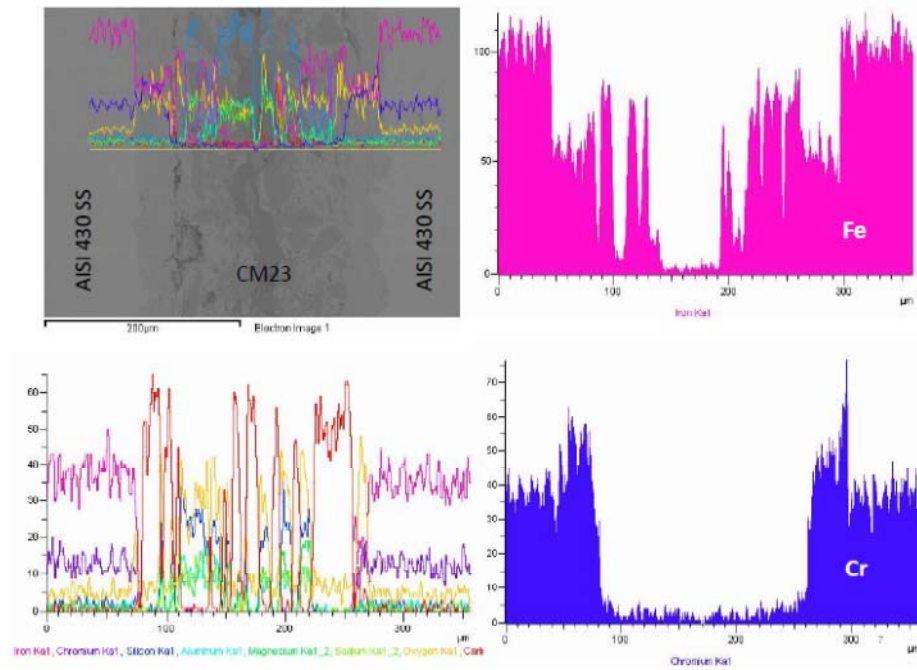


Fig. 4.21 EDX line scan across interface between CM23 glass–ceramics and AISI430 stainless steel

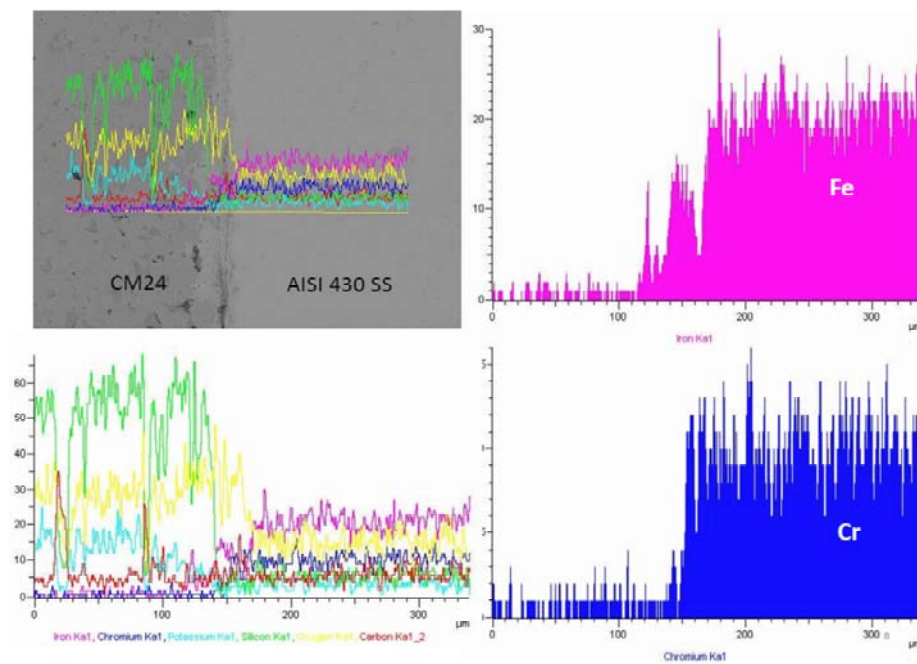


Fig. 4.22 EDX line scan across interface between CM24 glass–ceramics and AISI430 stainless steel

4.1.7. Joining test between glass-ceramics and YSZ ceramic

From the CTE after crystallized as glass-ceramics by heat treatment and the results of joining test with stainless steel, glass compositions CM13, CM22 and CM23 were selected to join with 8 mol % Y_2O_3 - ZrO_2 (YSZ). The CTEs of all selected glass composition were close to AISI430 stainless steel and YSZ. The comparison of dilatometric curves is shown in Fig. 4.23. The results of joining test showed that only CM22 and CM23 can be attached on YSZ ceramics after heat treated at 900 °C for 2 h. The cross section images of heat treated sample are shown in Fig. 4.24 observed by optical microscope. Although the chemical reaction is not found at interface the between glass-ceramics and YSZ, many pores were found in glass-ceramics CM22 and close pore was found in CM23 glass-ceramics.

From experimental result of developing glass-ceramics sealant, many properties of glass-ceramics in this part were able to utilize as glass-ceramics sealant at high temperature. For SOFC sealant applications, the electrical resistivity of glass composition containing alkali oxides especially Na^+ , although, was accepted as requirement, this glass was highly dangerous for the ferritic steel interconnect. The next part of experiment was continued to develop a barium-free glass-ceramics for SOFC sealant application excluded alkali oxide in the compositions.

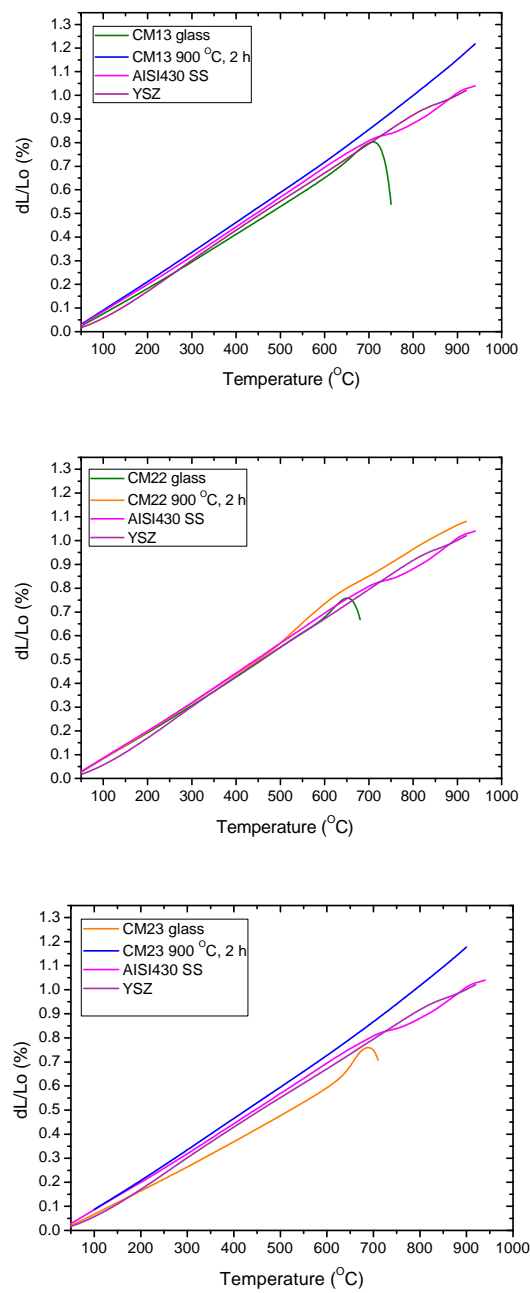


Fig. 4.23 Comparison of dilatometric curves of selected bulk glass, glass–ceramics, AISI430 SS and YSZ ceramics

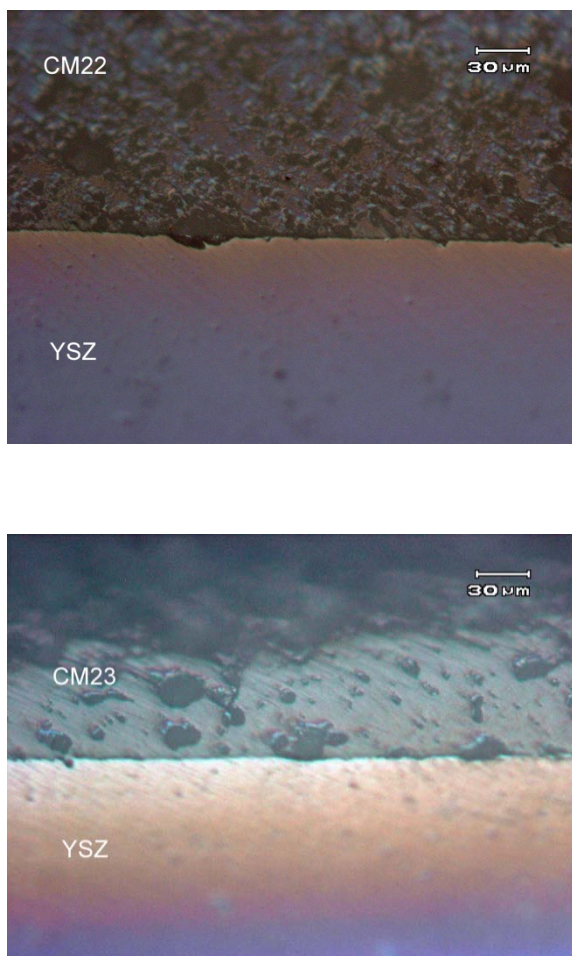


Fig. 4.24 Cross section of Glass–ceramics and YSZ ceramic after heat treated at 900 °C,
2 h

4.2 Part II: Development of glass-ceramics seal in system $\text{MgO-CaO-B}_2\text{O}_3\text{-Al}_2\text{O}_3\text{-SiO}_2$

4.2.1. Glass selection and preparation

In the second part, the glass composition 34, 35 and 37 base on åkermanite, diopside and forsterite constitutional compounds were successfully prepared by melting at 1500 °C. Then, glass compositions 34 and 35 which their liquidus temperature is slightly higher than glass 37 were varied composition by adding 5, 10, 15 and 20 % B_2O_3 in original composition. 5 % B_2O_3 was added to modify glass 37 composition because it was original from eutectic point, which melting temperature is the lowest. The completely melted glass was water quenched as frit and ground into powder. The particle size

distribution of glass powder, which sieved through 325 mesh screen ($<44 \mu\text{m}$), are shown in Table 4.12. The median particle size distribution d_{50} and d_{90} of each glass powder sample are very close, which are approximately $28 \mu\text{m}$ and $60 \mu\text{m}$, respectively.

Table 4.12 Particle size distribution of glass powders for properties characterization and joining test

Glass	Particle size distribution (μm)	
	d_{50}	d_{90}
34	28.464	60.354
34 -5B	28.802	60.602
34 -10B	28.49	59.242
34 -15B	27.102	57.111
34 -20B	27.326	57.413
35	28.354	58.464
35 -5B	27.963	57.252
35 -10B	28.465	59.806
35 -15B	28.029	58.166
35 -20B	28.293	56.986
37	28.644	57.974
37 -5B	28.802	58.314

4.2.2. Thermal properties of glass 34, 35 and 37 series

The T_g , T_c and T_p of glasses are summarized in Table 4.2. DTA curves of glasses 34 series are plotted with definition of their T_g , T_c and T_p in Fig. 4.25. Boron oxide content in glass composition reduced the glass transition and crystallization onset point in this glass series. The crystallization temperatures of glass decreased from 845 to 757 $^{\circ}\text{C}$ by increasing boron oxide content. This means that the crystalline phases will formed at joining temperature (900 $^{\circ}\text{C}$) and working temperature (800 $^{\circ}\text{C}$) of glass-ceramic sealants.

Table 4.13 T_g , T_c and crystallization peak temperature (T_p) obtained by DTA

Properties	T_g	T_c	T_{p1}	T_{p2}
34	744	845	889	921
34-5B	695	819	885	-
34-10B	673	788	864	-
34-15B	655	774	860	-
34-20B	647	757	869	-
35	745	847	919	-
35-5B	708	821	928	-
35-10B	674	786	913	-
35-15B	661	782	901	-
35-20B	653	768	915	-
37	746	837	944	-
37-5B	717	871	926	-

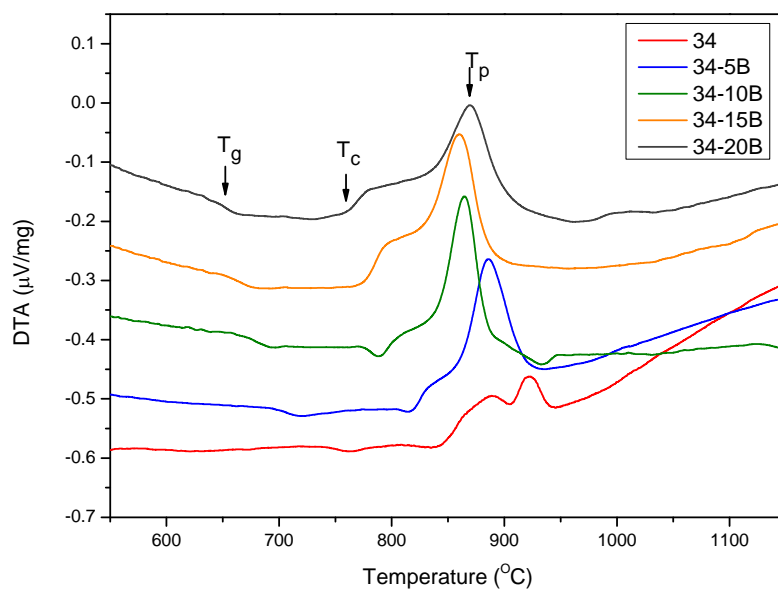


Fig. 4.25 DTA curves of glass 34 series

For glasses in 35 series, the trend of T_g and T_c was the same as 34 series, which was decreased by boron oxide contents. The T_g and T_c was in range of 653 – 745 °C and 768 – 847 °C.

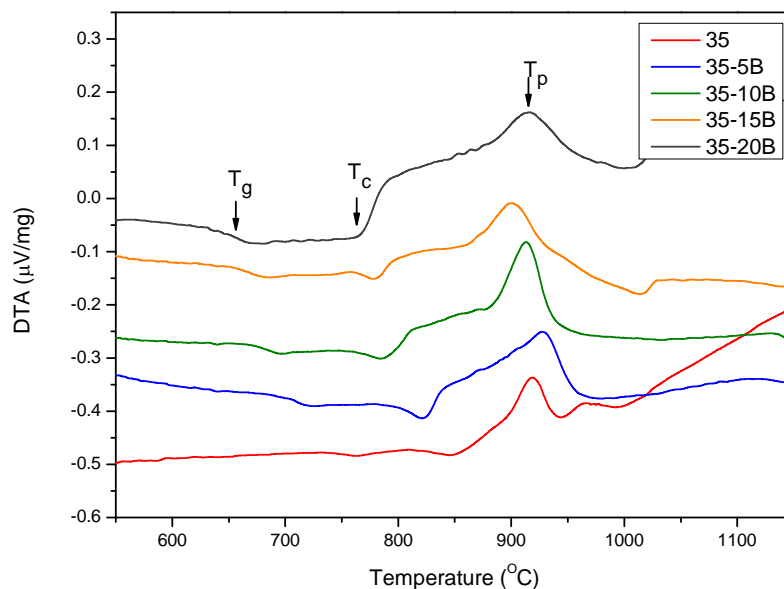


Fig. 4.26 DTA curves of glass 35 series

The T_g and T_c range of glass in 37 series showed in Fig. 4.27 are also be explained in the same way as previous glass series. The 5 wt.% of boron could reduce the T_g and T_c of non-boron oxide glass 37 from 746 to 717 $^{\circ}\text{C}$ and 837 to 871 $^{\circ}\text{C}$ respectively.

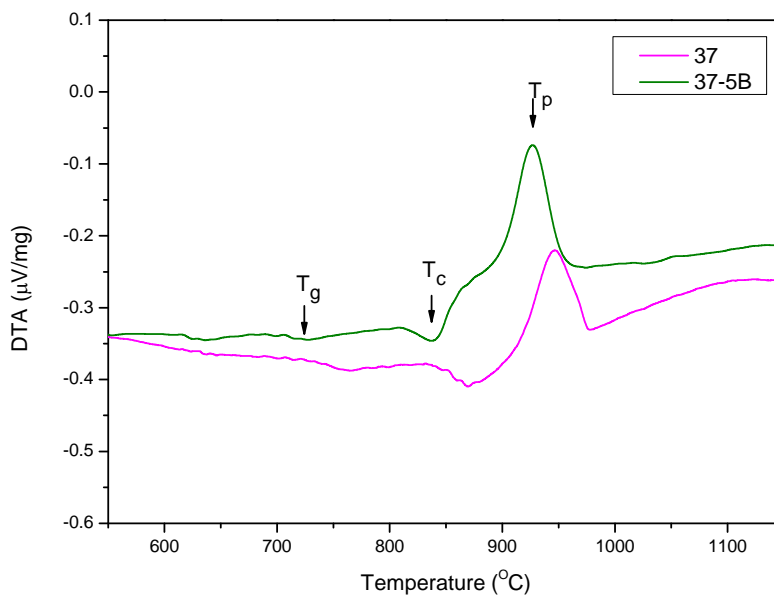


Fig. 4.27 DTA curves of glass 37 series

4.2.3. Hot-stage microscope

Fig. 4.28 is the example of image analysis of glass 34 – 10B obtained by hot-stage microscope. The compact glass powder was heated from room temperature to 1300 °C at a heating rate of $5 \text{ K} \cdot \text{min}^{-1}$. The variation of height and area of compact glass powder (Fig. 4.28 (a)) was measured on the images, correlated to the temperature as shown Fig. 4.28 (b). The other image analysis results were shown in Appendix E.

Table 4.14 Thermal parameters obtained by hot stage microscope (temperature in °C) and calculated constants A B and T_0 in VFT equations

Glass	T_{FS}	T_{MS}	T_D	T_{SP}	T_{HB}	T_F	A/A_0	A	B	T_0
34	767	843	-	-	-	-	0.74			
34-5B	745	807	-	-	1203	1217	0.62	-2.58	5778	250
34-10B	715	769	787	864	1125	1148	0.62	-1.91	4440	312
34-15B	706	765	776	817	1090	1134	0.63	-3.07	6105	204
34-20B	678	732	750	813	1020	1062	0.64	-3.68	6090	201
35	773	845	1340	-	-	-	0.73	-	-	-
35-5B	749	816	846	-	1167	1183	0.63	0.98	1497	565
35-10B	712	779	797	831	1128	1142	0.66	1.45	1127	565
35-15B	680	750	776	813	900	1137	0.63	1.23	1367	506
35-20B	675	747	750	816	890	1033	0.64	-0.17	2076	451
37	785	861	876	1257	1269	1312	0.65	1.83	1057	640
37-5B	762	831	854	908	1178	1215	0.64	1.36	1258	600

All boron free compositions except glass 37 are unable to obtain sphere point and half sphere. This is caused by fast crystallization in both compositions. A/A_0 is the ratio between final area and initial area of the glass-powder compact. The compact powder achieves the good densification of 95-98% when the value of A/A_0 is around 0.65 at T_{MS} [34]. A/A_0 of composition 34 and 35 at maximum shrinkage are 0.74 and 0.73 respectively while the other compositions reach to maximum shrinkage at A/A_0 around 0.64. It can be explained by correlation between T_{MS} and T_c (from DTA, in Table 4.13). The T_{MS} is the temperature reach to their maximum shrinkage, while T_c is onset point for crystallization process, the first crystalline phase appear in glassy matrix. If $T_c > T_{MS}$, the dense and homogeneously crystallization can be obtained in glass-ceramics after thermal process. In contrast, if $T_c < T_{MS}$ the crystallization in the compacted glass started earlier, thus the further sintering process was inhibited. Consequently the densification is incompleated because of remaining of high porosity in bulk glass-ceramics. The complete densification can be obtained in glass compositions with higher boron oxide content after thermal process because the higher content of boron oxide lead to form higher the glassy phase in the glass-ceramics.

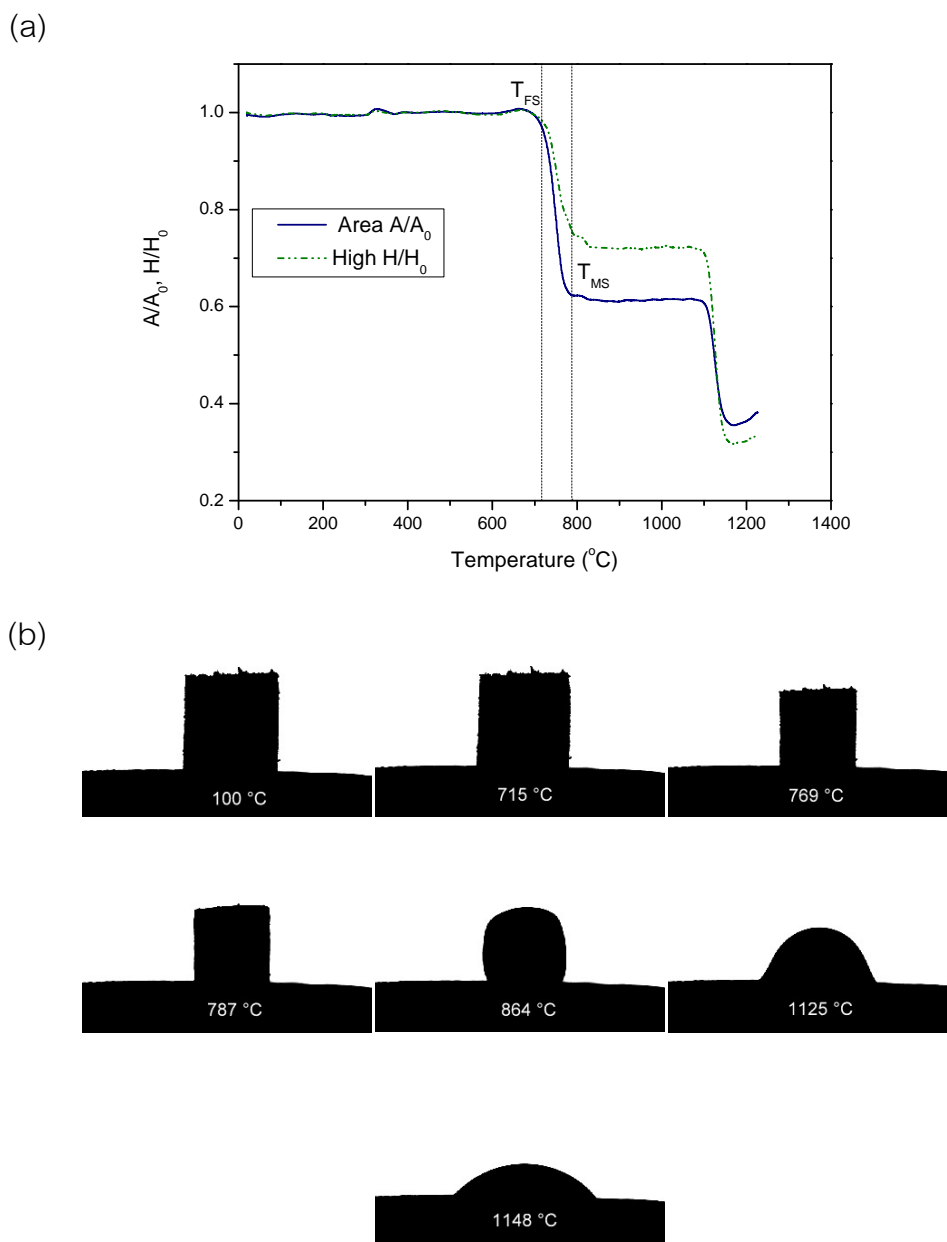


Fig. 4.28 (a) Variation in area and height of powder sample of 34 – 10B during hot stage microscope measurement (b) Geometric shapes of the sample associated to (a)

The viscosity of glass-ceramics were carried out by fixed point calculation followed the definition of M.J. Pascual as shown below and VFT equation described in Chapter 3.

Characteristic viscosity points, defined by M.J. Pascual :

- First shrinkage temperature, T_{FS} ($\log \eta = 9.1$) η is viscosity dPa · s
- Maximum shrinkage temperature, T_{MS} ($\log \eta = 7.8$)
- Deformation temperature, T_D ($\log \eta = 6.3$)
- Sphere temperature, T_{SP} ($\log \eta = 5.4$)
- Hemisphere temperature, T_{HB} ($\log \eta = 4.1$)
- Flow temperature, T_F ($\log \eta = 3.4$)

The calculated viscosity of glass 34 series with 5 – 20 wt.% boron oxide is shown in Fig. 4.29. The viscosity at the same temperature decreases with amount of boron oxide content. For this glass series, the viscosity at 800 °C and 900 °C is in range of $10^{5.7} - 10^{7.3}$ and $10^{4.3} - 10^{5.5}$ dPa·s respectively.

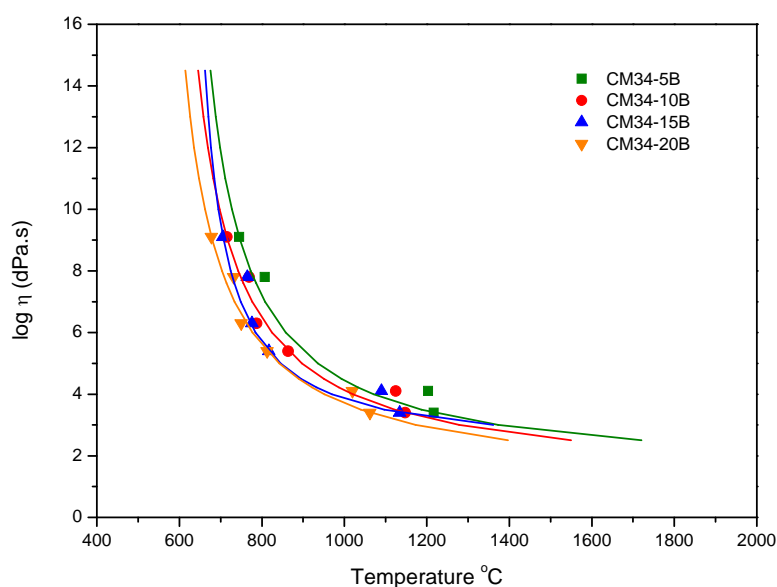


Fig. 4.29 Plot of viscosity data of glass 34 series obtained from hot-stage microscope compared with viscometer curves calculated from VFT equation (solid line)

The viscosity of glasses in glass 35 series is slightly lower than glass 34 series, which also reduced by boron oxide contents. Their viscosity is $10^{5.7} - 10^{7.3}$ dPa·s at 800 °C and $10^{4.4} - 10^{5.5}$ dPa·s at 900 °C respectively as shown in Fig. 4.30.

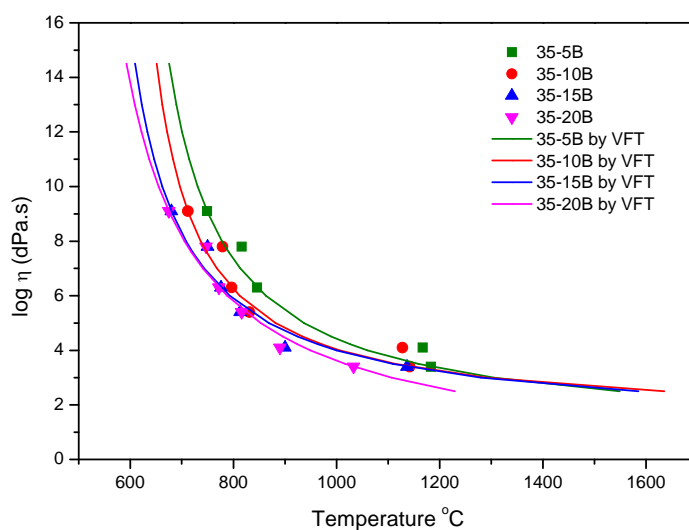


Fig. 4.30 Plot of viscosity data of glass 35 series obtained from hot-stage microscope compared with viscometer curves calculated from VFT equation (solid line)

The viscosity of glass 37 and 37-5B are plotted in Fig. 4.31. The viscosity of boron containing glass was slightly lower than non boron. It decreased from $10^{5.8}$ to $10^{5.4}$ dPa·s at 900 °C, and from 10^8 to $10^{7.2}$ dPa·s at 800 °C. At high temperature, the viscosities that obtained from fixed viscosity at T_{HB} and T_{SP} were deviated from viscosity calculated by VFT because the crystallization rate of glass in this system was very fast, thus, the crystalline phases were remain in glassy phase. The viscosity then shifted to higher, before completely melt at higher temperature.

From the softening behavior and viscosity experiments, it was found that glasses with boron oxide from 5–20 wt.% have the CTEs in range of requirements for SOFC sealing application, which were between 10^6 and 10^9 dPa·s at working temperature and prone to keep higher than 10^9 dPa·s after crystallized as glass-ceramics [34, 89].

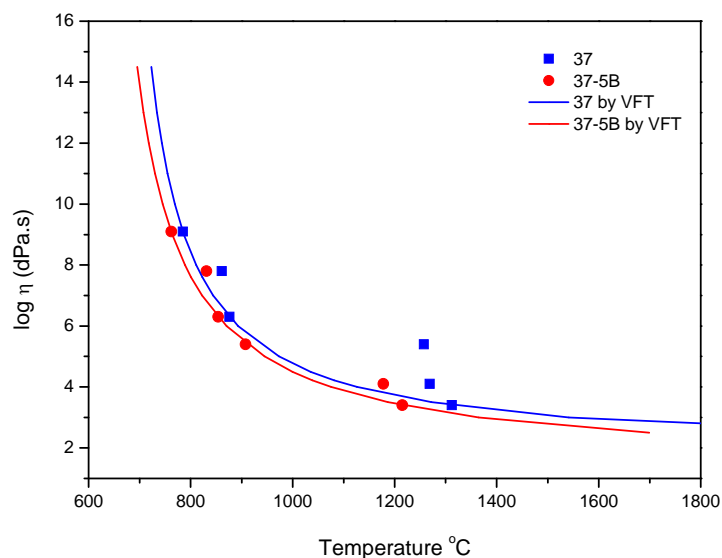


Fig. 4.31 Plot of viscosity data of glass 37 series obtained from hot-stage microscope compared with viscometer curves calculated from VFT equation (solid line)

4.2.4. Joining test between glass-ceramics/ Crofer 22 APU stainless steel and glass-ceramics/YSZ ceramics

The purposes of the joining test experiment are to test long term stability of the joining between glass-ceramics and Crofer 22 APU and between glass-ceramics and YSZ in. The interface between joined materials was observed through cross-sections by SEM/EDS. Both joining test samples were heat treated at joining temperature 900 °C, 2 h and then 800 °C for 100 h in normal air.

4.2.4.1. Joining test between glass–ceramics and Crofer 22 APU stainless steel

The results of joining test between glass-ceramics and Crofer 22 APU stainless steel are summarized in Table 4.14. Glass-ceramics without boron oxide content glass 37 and with 5 wt.% boron oxide glass 35-5B could not join with the stain steel. After heat treatment at joining temperature, they were broken separately. In case of glass composition which was containing higher boron oxide and lower viscosity at joining temperature, all glass-ceramics from glass 34 series could be joined with Crofer 22

APU. The glass-ceramics from glass 35 series with 10-20 wt.% B₂O₃ and 37-5B with 5 wt.% B₂O₃ could be joined with Crofer 22 APU stainless steel. The lower viscosity glass-ceramics made by addition of boron oxide contained more glassy phase in bulk glass-ceramics. It will encourage the stress release in a brittle glass-ceramics, caused by CTE mismatch, and given them a proper viscosity to keep joining with the stainless steel.

Table 4.15 Joining test results compare with the CTE of glass ceramics.

Paste sample	CTE (100-600°C), $\times 10^{-6} \text{ K}^{-1}$	Joining test
	GC 900°C, 2 h	
34-5B	11.71	✓
34-10B	10.13	✓
34-15B	9.53	✓
34-20B	9.72	✓
35-5B	10.12	✗
35-10B	9.20	✓
35-15B	9.25	✓
35-20B	10.41	✓
37	11.02	✗
37-5B	10.12	✓

Note: ✓ = attached, ✗ = detached

SEM images together with EDS mapping pictures of Cr and Fe elements which were taken on cross-section between glass-ceramics in 34 series and Crofer 22 APU stainless steel are shown in Fig. 4.32. The diffusion of Cr and Fe ion were observed by EDS mapping. While the other joined samples performed sharply contrast of Cr and Fe element concentrations at the interface, it only found that the significant detected points of Cr element across into glass-ceramics 34-20B side. It could be assumed that at higher viscosity and in glassy state, Cr and Fe ions could not diffuse through the interface between viscous glassy phase and the stainless steel. In case of glass-ceramics containing higher boron oxide content, the viscosity is continue to decrease, the Cr and Fe then can diffuse and form layer of Cr₂O₃ and FeO/Fe₂O₃ as the layer found at the interface.

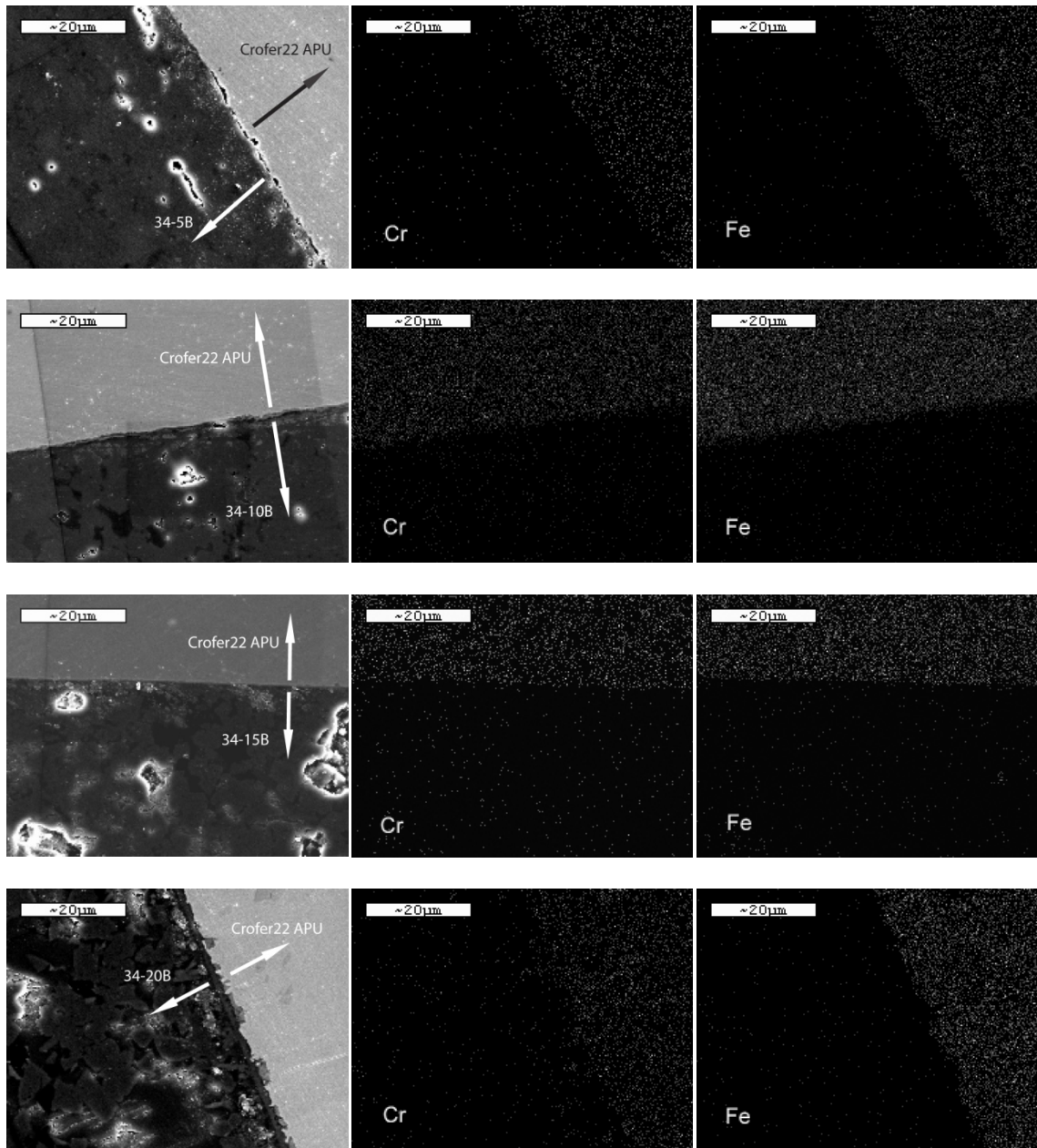


Fig. 4.32 SEM and EDX mapping of cross-section pictures of joined glass-ceramics in 34 series and Crofer 22 APU at 900 °C, 2 h and dwelling at 800 h, 100 h

For joining of glass-ceramics from glass 35 series and the stainless steel (Fig. 4.33), the glass-ceramics containing 10, 15 and 20 wt.% shaved sharply interface. The

diffusion trace of Cr and Fe through the glass-ceramics and the stainless steel boundary was not found.

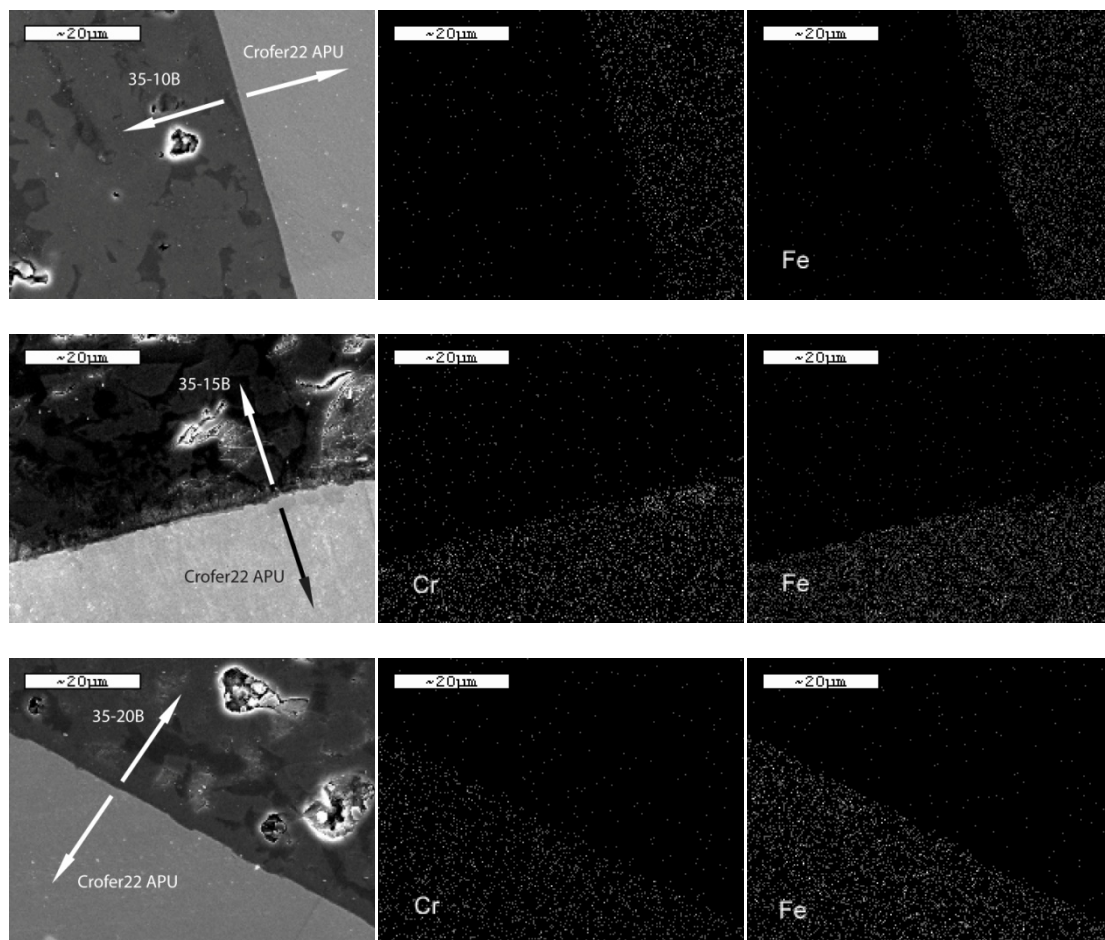


Fig. 4.33 SEM and EDX mapping of cross-section pictures of joined glass-ceramics in 35 series and Crofer 22 APU at 900 °C, 2 h and dwelling at 800 h, 100 h

Glass-ceramics 37 joined with the stainless steel also similar to the other sample which perform a sharply interface, the layer of Cr or Fe oxides was not found as shown in Fig. 4.34.

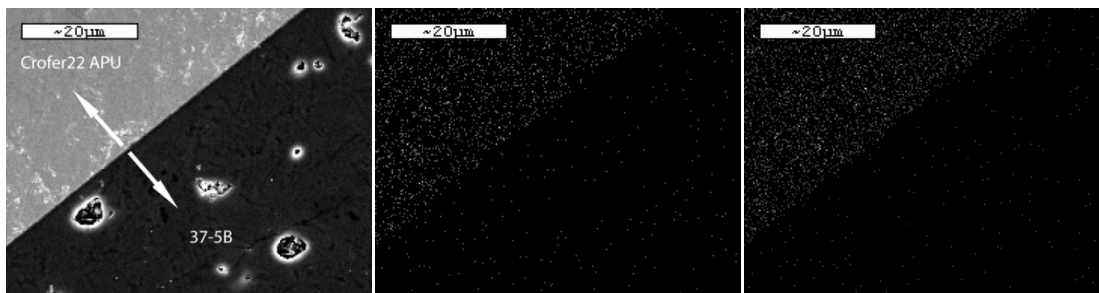


Fig. 4.34 SEM and EDX mapping of cross-section pictures of joined glass-ceramics in 37 series and Crofer 22 APU at 900 °C, 2 h and dwelling at 800 h,100 h

4.2.4.2. Joining test between glass–ceramics and YSZ ceramic

The joining test of this experiment is different from 4.2.2.1. The sandwich of glass paste between YSZ ceramics plate was free of compressive force in order to compare the different with load of 1 kg sandwich sample in previous section. As-received YSZ ceramics (8 mol% $Y_2O_3 - ZrO_2$) were prepared from MTEC laboratory by tape casting of nano particle and sintered at 1200 °C. The glass-ceramics was also joined following the same method of joining test with Crofer 22 APU stainless steel.

The cross-section between glass-ceramics from glass 34 series and YSZ were shown in Fig. 4.35. The glass-ceramics 34-5B and 34-10B perform dense crystalline phases among glassy matrix and with small pores after heat treated at 900 °C for 2 h dwelling at 800 °C for 100 h. Their joining interfaces with YSZ show smoothly and tightly interface without reaction layer between glass-ceramics and YSZ ceramics. The size and amount of pore found in glass-ceramics 34-10B are bigger than glass-ceramics 34-5 B. In glass-ceramics containing higher boron oxides, which are glass-ceramics 34-15B and glass-ceramics 35-20B, the separation between crystalline phases and micro crack among them were detected. The EDS spectra at different phases were determine in quantity of elements, showed in Fig. 4.36 and Fig. 4.37 . It found that ratio of point 1 in Fig. 4.36 is close to åkermanite (C_2MS_2), therefore, the crystallization of this phases and low CTE of glassy phase (point 2) should be the reasons for micro cracks. The glass-ceramics 34-20B found diopside phase separate from glassy phase according to point 1 and point 2 in EDS result Fig. 4.37. Small pores were found along the interface

between YSZ and both glass-ceramics 34-15B and 34-20B, however, there is no crack penetrate from this zone.

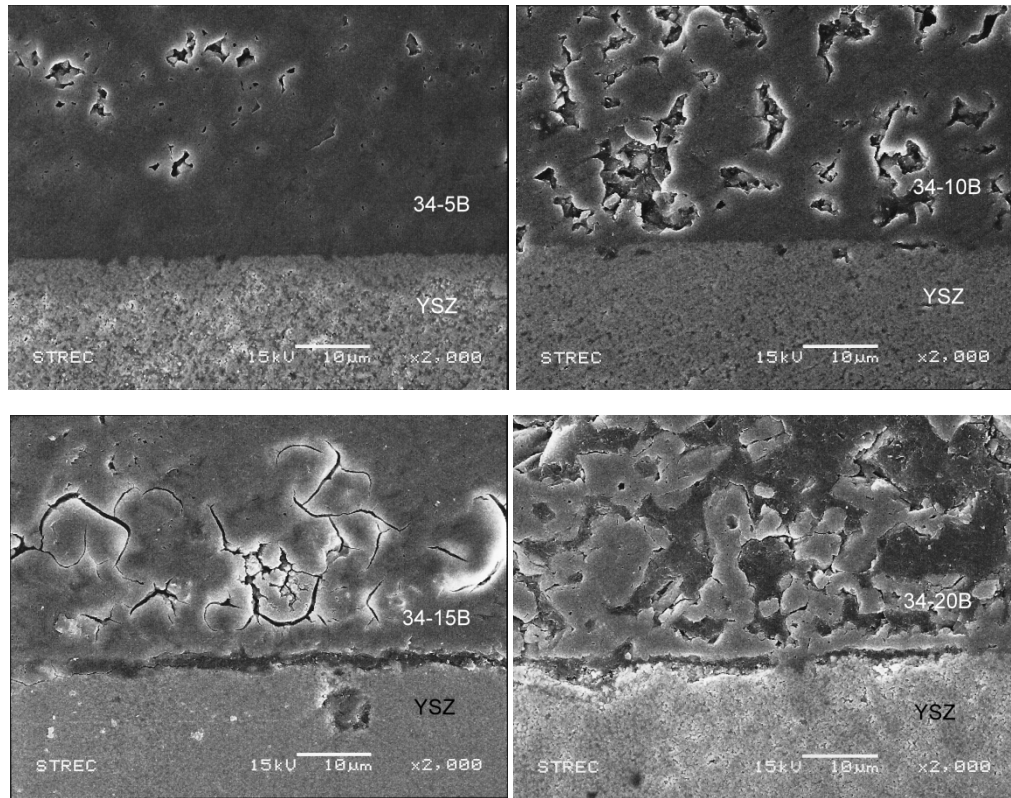


Fig. 4.35 SEM of cross-section pictures of joined glass-ceramics in 34 series and YSZ ceramics

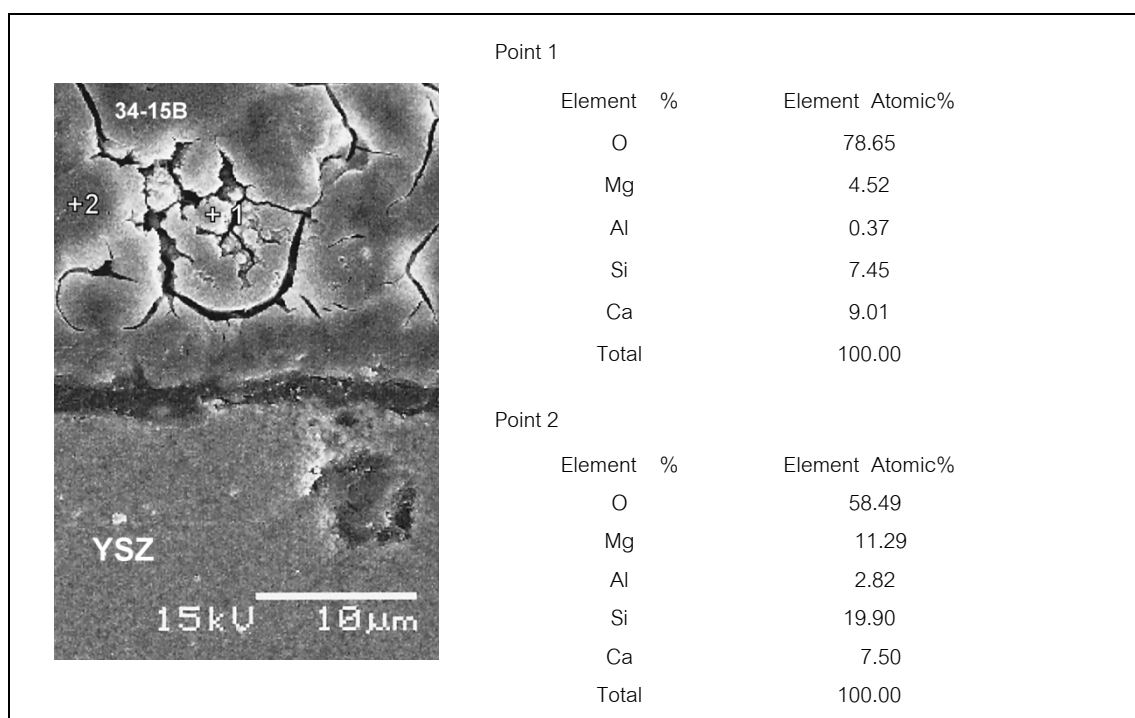


Fig. 4.36 SEM/EDS quantitative results of glass-ceramics 34-15B joined with YSZ

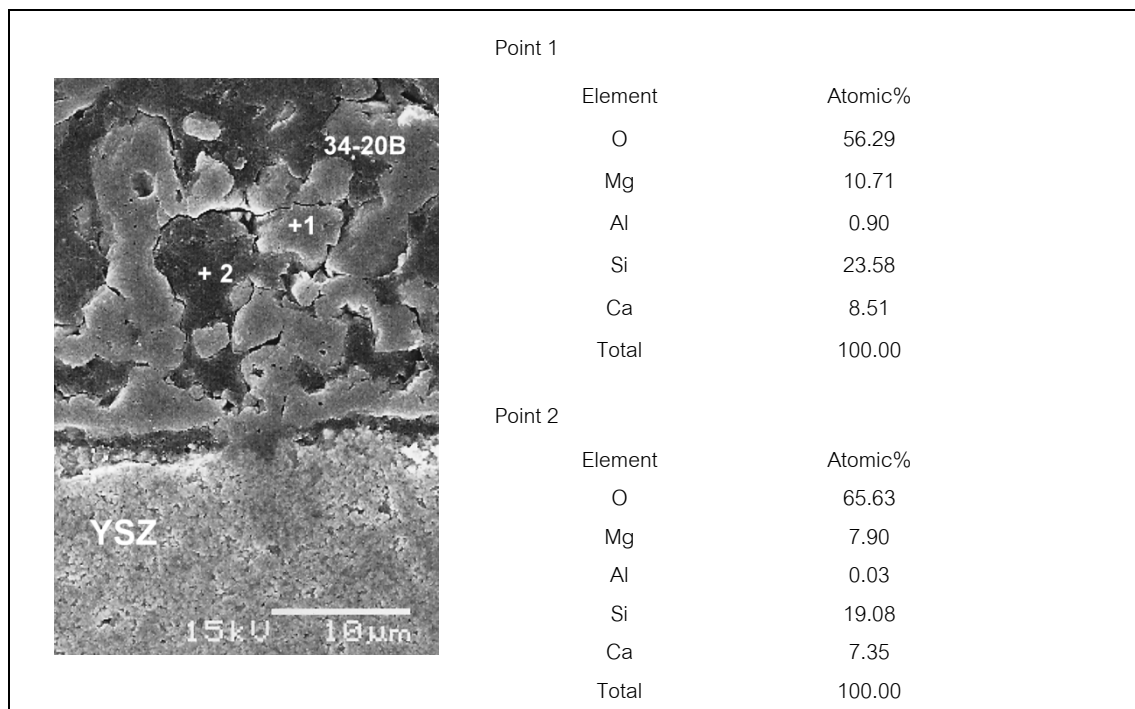


Fig. 4.37 SEM/EDS quantitative results of glass-ceramics 34-20B joined with YSZ

The results of heat treated sandwich of glass 35 series and YSZ showed the increase in pores size. The amount of pores related to the boron oxide contents in glass. The interface between glass-ceramics and YSZ was also smoothly and tightly interface without chemical reaction layer as shown in Fig. 4.38. The pore size and amount of pore were increase with B_2O_3 contents.

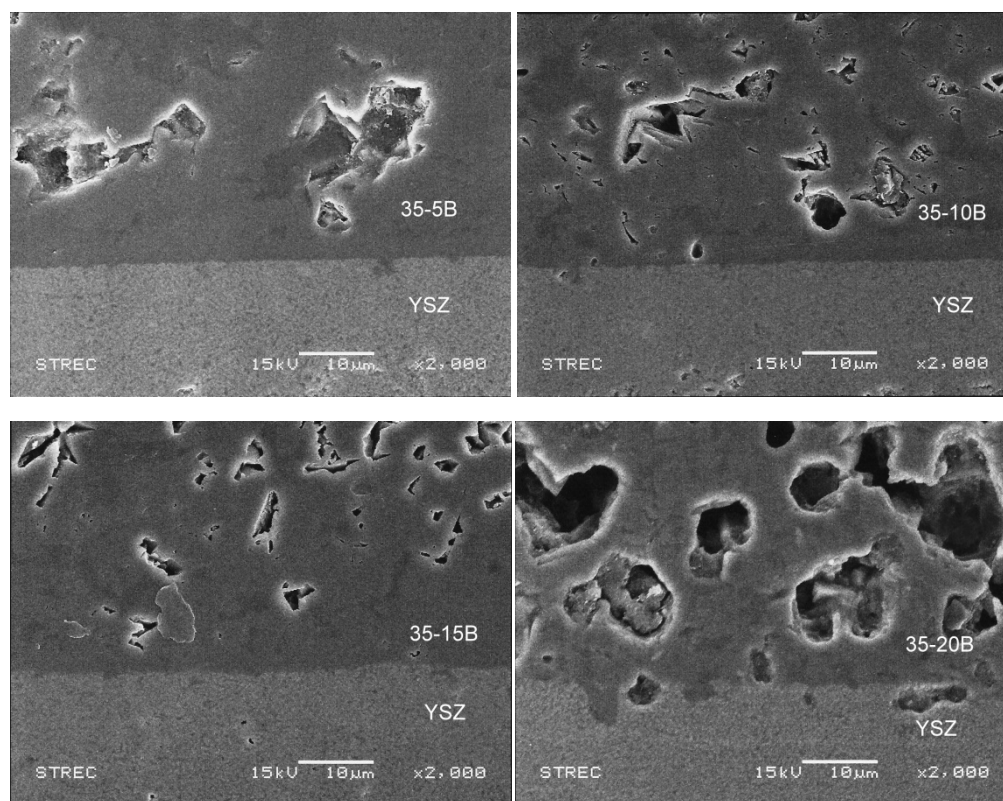


Fig. 4.38 SEM of cross-section pictures of joined glass-ceramics in 35 series and YSZ ceramics

In Fig. 4.39, glass-ceramics 37-5B showed the similar bonding with YSZ without attacking the interface of YSZ.

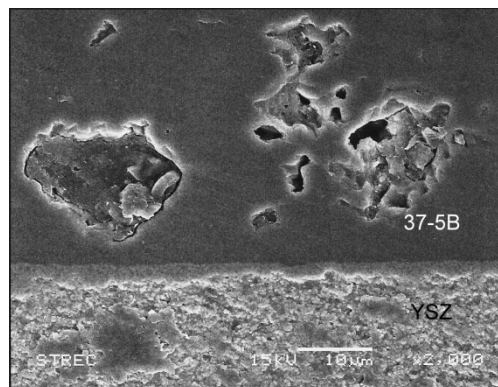


Fig. 4.39 SEM of cross-section pictures of joined glass-ceramics in 37 series and YSZ ceramics

Glass-ceramics obtained by heat treatment without load was containing higher pore and larger size than load of 1 kg as sandwich sample of glass-ceramics and crofer22 APU stainless steels. The glass-ceramics between the crofer22 APU stainless plates could be deformed by load, consequently, it led to release the pores and bubbles during joining process at 900 °C. The pores were difficult to release out from viscous glassy phase between sintering process, and high crystallization rate inhabited their movement by increasing of viscosity when crystallization happens. Finally, the pores were remaining surrounded by crystalline phases.

4.2.5. Thermal cycle and leak test

Thermal cycle test was evaluated from leak rate. The experiment was carried out by heat treating the sandwich sample of Crofer 22 APU/ glass-ceramics/ Crofer 22 APU at 800 °C, dwelling for 12 h each thermal cycle. The helium gas leak rate from the sample was measured at room temperature by pressure drop using manormeter as described in chapter 3. The results in Table 4.16 are the leak rate in unit volume of water change by gas pressure dropping (cm^3) per time (min) and sealing length.

The comparison of leak rates of all sample vs number of thermal cycles are plot in Fig. 4.40. The leak rate of glass-ceramics 37 as sealant in the sandwich sample obviously increased after heat treated for 2 thermal cycles. The leak rate continue increased to reached the maximum at $7.40 \times 10^{-2} \text{ cm}^3 \cdot \text{min}^{-1} \cdot \text{cm}^{-1}$ after cycle number 6

and small dropped to 5.60×10^{-2} after 7 thermal cycle number and the thermal cycle test of this sample was terminated.

For the glass-ceramics in 34 and 35 as the sealants, the differences of leak rates were not clear in comparing with each composition or each thermal cycle. The leak rate were in the range of 10^{-3} – 10^{-4} $\text{cm}^3 \cdot \text{min}^{-1} \cdot \text{cm}^{-1}$. While compare with other works from literatures, it was found that the smallest leak rate of compressive mica seal at 800 °C, 2 psi of He gas, is 1.55×10^{-4} $\text{cm}^3 \cdot \text{min}^{-1} \cdot \text{cm}^{-1}$ [12]. Therefore, the leak rates of glass-ceramics sealants in 34 and 35 series were comparable to that work. The glass-ceramics sealant should hermetically seal at high temperature because it will become softer by glassy phase and dense matrix. However, it must be free of crack between interlayer and brittle ceramic phase by thermal expansion mismatch.

Consequently, it could be said that the glass composition with 5 – 20 wt.% boron in 34 series and 10 – 20 wt.% in 35 series could be prepared for a stable sealant, which kept low leak rate through 10 thermal cycles or 108 h of heat treated at 800 °C.

Table 4.16 Leak rate of sandwich sample of Crofer 22 APU/glass-ceramics/Crofer 22 APU after thermal cycle test ($\text{cm}^3 \cdot \text{min}^{-1} \cdot \text{cm}^{-1}$)

Sample	Number of thermal cycle									
	1 0h	2 12h	3 24h	4 36h	5 48h	6 60h	7 72h	8 84h	9 96h	10 108h
34-5B	1.53	5.33	2.32	7.53	2.62	2.27	2.01	1.71	1.37	3.43
	E-03	E-03	E-03	E-04	E-03	E-03	E-03	E-03	E-03	E-03
34-10B	1.20	2.45	2.66	1.78	4.05	4.92	9.96	1.48	3.11	1.56
	E-03	E-03	E-04	E-03	E-03	E-03	E-04	E-03	E-04	E-03
34-15B	2.39	2.65	3.48	2.45	2.47	1.43	4.69	1.10	1.10	4.39
	E-03	E-03	E-04	E-03	E-03	E-03	E-04	E-03	E-03	E-03
34-20B	2.18	2.26	1.81	1.42	2.43	5.30	1.85	1.56	8.26	1.41
	E-03	E-03	E-03	E-03	E-03	E-04	E-04	E-03	E-04	E-03
35-10B	2.25	2.33	1.90	2.18	8.37	1.56	2.61	1.13	1.28	1.68
	E-03	E-03	E-03	E-03	E-04	E-03	E-05	E-03	E-03	E-03
35-15B	2.61	2.59	3.36	1.47	3.69	1.71	7.34	9.38	2.79	2.45
	E-03	E-03	E-03	E-03	E-03	E-03	E-04	E-04	E-04	E-03
35-20B	1.63	2.62	5.20	1.54	2.27	2.25	8.90	1.18	1.56	1.77
	E-03	E-03	E-03	E-03	E-03	E-03	E-04	E-03	E-03	E-03
37-5B	2.54	2.59	7.31	1.14	4.23	7.40	5.60			
	E-03	E-03	E-03	E-02	E-02	E-02	E-02			

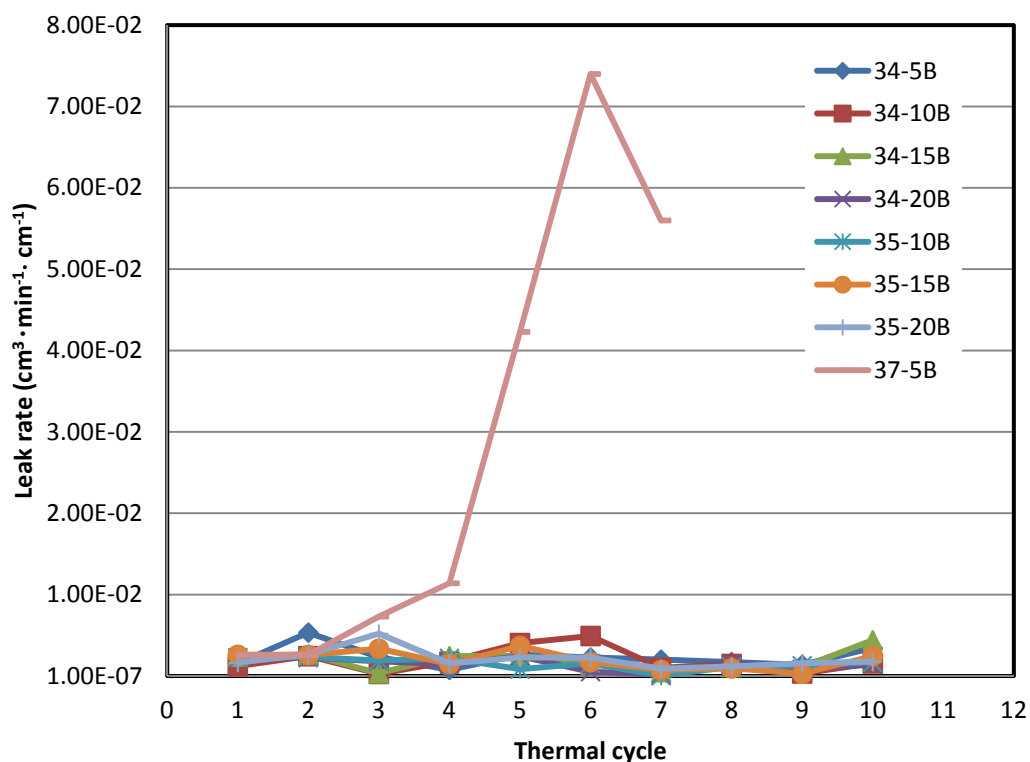


Fig. 4.40 Comparison of leak rate of Crofer 22 APU stainless steel and glass-ceramic sealant after each thermal cycle (800 °C, 12 h)

4.2.6. Crystallization behavior and thermal expansion stability

The crystalline phases in glass-ceramics were determined by XRD. The results are summarized in Table 4.17. The åkermanite crystalline phase was found as major crystalline phase, in non-boron oxide glass-ceramics 34, 35 and 37 series, which XRD patterns are shown in Fig. 4.41. In comparison of different crystalline phases corresponding to B_2O_3 contents in each series of glass compositions, the XRD-patterns of glass-ceramics are plotted in Fig. 4.42 and Fig. 4.43. Diopside and forsterite phases are found in glass-ceramics with 5 wt.% B_2O_3 with åkermanite phase. The åkermanite phase was not found in higher than 10 wt.% B_2O_3 containing glass-ceramics. In glass-ceramics 35-15B and 35-20B, the anorthite phase is detected and its XRD intensity increase among amorphous broad peak as showed in Fig. 4.43.

Table 4.17 Crystalline phases found in glass-ceramics after heat treated at 900 °C, 2 h obtained by XRD

Composition	Åkermanite (C ₂ MS ₂)	Diopside (CMS ₂)	Forsterite (M ₂ S)	Anorthite (CAS ₂)
34	X	-	-	-
34-5B	X	X	X	-
34-10B	X	X	-	-
34-15B	-	X	X	-
34-20B	-	X	-	-
35	X	-	-	-
35-5B	X	X	X	-
35-10B	X	X	X	-
35-15B	-	X	X	X
35-20B	-	X	-	X
37	X	-	-	-
37 – 5B	X	X	X	-

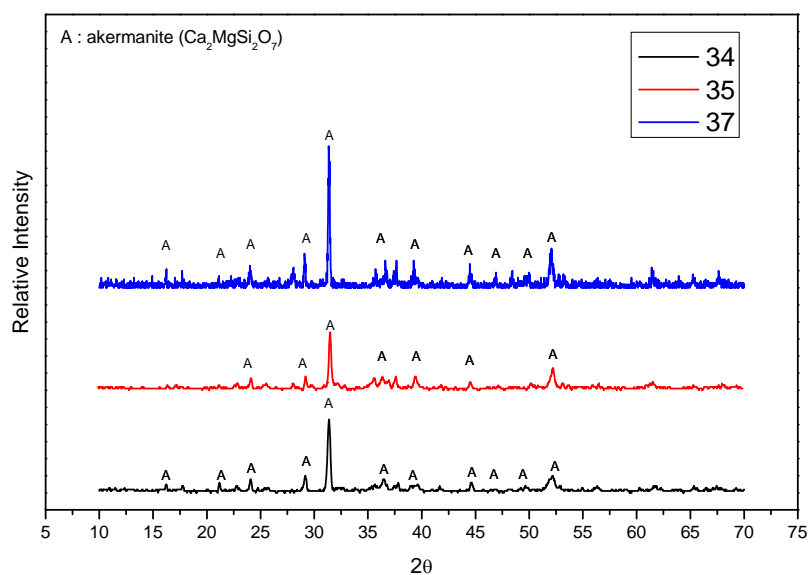


Fig. 4.41 XRD-patterns of glass-ceramics 34, 35 and 37 after heat treated at 900 °C, 2 h

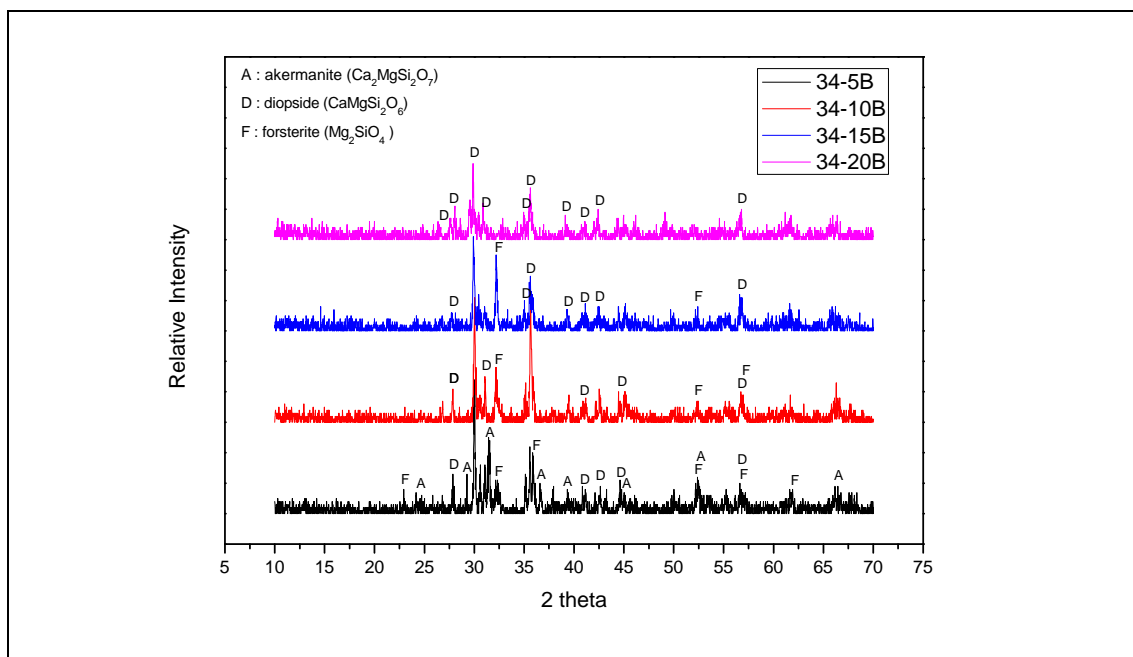


Fig. 4.42 XRD-patterns of glass-ceramics 34 series after heat treated at 900 °C, 2 h and continue heat treated at 800 °C, 100 h

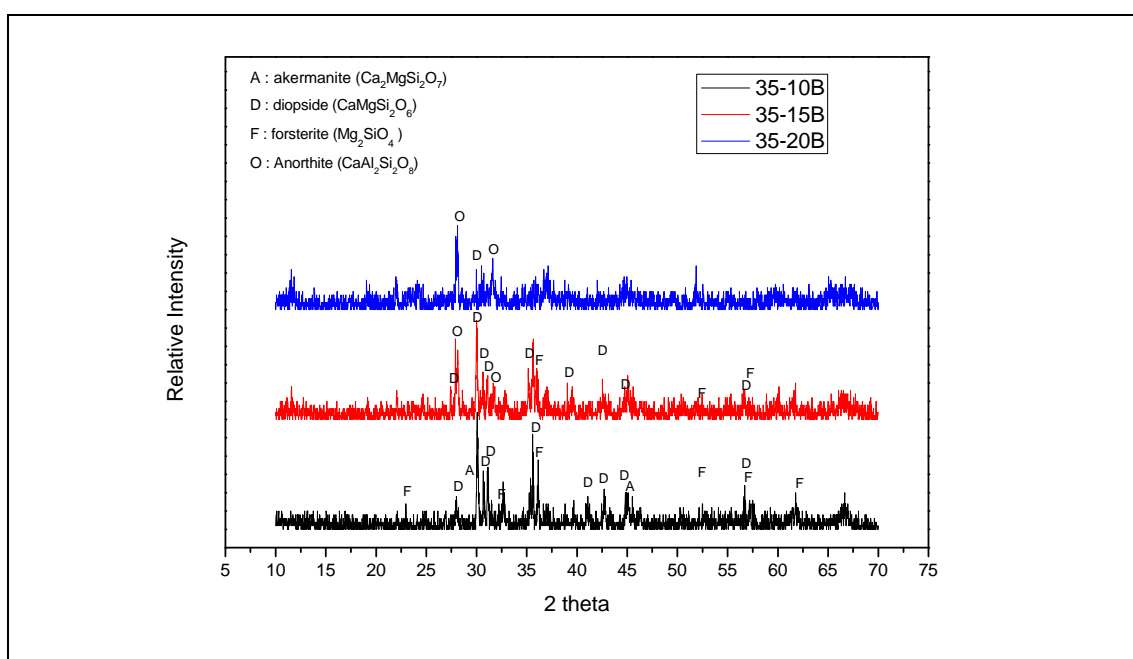


Fig. 4.43 XRD-patterns of glass-ceramics 35 series after heat treated at 900 °C, 2 h and continue heat treated at 800 °C, 100 h

In order to study the thermal stability on the change of their crystalline phases and CTE, the glass-ceramics were continued heat treated at 800 °C for 100 h. The dilatometric curves are plotted to compare their change in thermal expansion, which are shown in Fig. 4.44 and their CTEs are showed in Table 4.18. The glass-ceramics after heat treated at 900 °C for 2 h are still found softening points because they are not completely crystallization and ratio of glassy phases are still high. When the glass-ceramics were continue heat treated at 800 °C for 100 h, the crystalline phases increase and reach to fully crystallization in glass matrix. The dilatometric curves of glass-ceramics after long term thermal treatment at 800 °C for 100 h are strengthen in linear curves by expansion of major crystalline phases. The increasing amount of boron oxide content performed the effect on decreasing CTE of glass-ceramics from 11.65 to 9.72 x 10⁻⁶ K⁻¹ for glass 34 series and 11.46 to 9.25 x10⁻⁶ K⁻¹ for glass 35 series. The other reasons of decreasing CTE is by decrease amount of åkermanite phases in crystallized glass when boron oxide content increase, then increase ratio of low CTE diopside and anorthite phases.

Table 4.18 CTE of glass-ceramics after heat treated at 900 °C, 2 h and continue heat treated at 800 °C, 100 h

Glass-ceramics	CTE (x10 ⁻⁶ K ⁻¹) (range 50 - 600 °C)	
	900 °C, 2 h	900 °C, 2 h + 800 °C, 100 h
34	11.65	N/A
34 - 5B	11.71	10.57
34 - 10B	10.13	10.26
34 - 15B	9.53	9.47
34 - 20B	9.72	9.50
35	11.46	N/A
35 - 5B	11.38	N/A
35 - 10B	10.12	9.96
35 - 15B	9.20	8.79
35 - 20B	9.25	9.49
37	10.41	N/A
37 - 5B	11.02	N/A
Crofer 22 APU SS		11.9
YSZ		10.8

Note: N/A = not analyzed

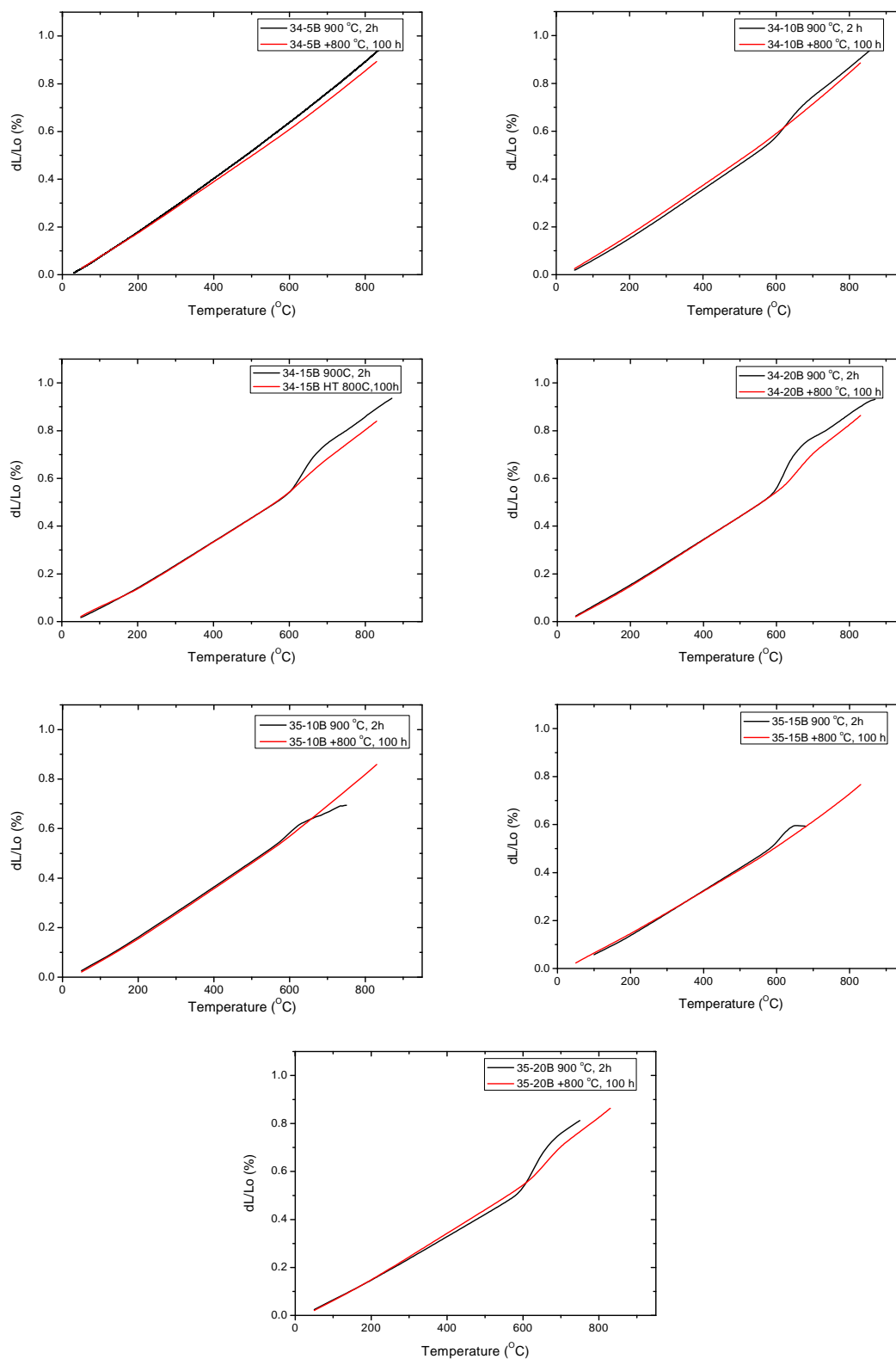


Fig. 4.44 Dilatometric curve of glass-ceramics 34 and 35 series after heat treated at 900 $^{\circ}\text{C}$ for 2 h and continue heat treated at 800 $^{\circ}\text{C}$ for 2h.

4.2.7. Electrical resistivity of glass- ceramics in 34 and 35 series

The glass compositions which were successfully joined with Crofer 22 APU were further studied their electrical properties. The electrical resistivity measurements were followed the same way as the experiment in Part I by using AC-impedance analysis technique. The experiment was started to measure resistance from 600 to 800 °C, unfortunately, the impedance analyzer could measure completely semi-circle at only 800 °C at varied frequency from 5 Hz–13 MHz. It seems the bulk resistivity of the samples in this part is too high to measure at low frequency and low temperature.

Table 4.19 Electrical resistivity of glass-ceramics at 800 °C

Sample	Electrical resistivity, ρ [$k\Omega\cdot\text{cm}$]
34-5B	2,921
34-10B	4,356
34-15B	43
34-20B	75
35-10B	369
35-15B	420
35-20B	892

The impedance spectra of glass-ceramics pellet from glass 34 series are shown in Fig. 4.45. The resistivity of glass-ceramics in this series is divided into two groups, the first group is lower boron oxide glass-ceramics 34-5B and 34-10B, which the electrical resistivity range is $3\text{--}4.5 \times 10^6 \Omega\cdot\text{cm}$. Another group is the electrical resistivity of 34-15B and 34-20B, which in the range of $4.5\text{--}7.5 \times 10^4 \Omega\cdot\text{cm}$. The difference of electrical resistivity of both groups is about 10^2 times different due to difference of microstructure of sintered pellets. The cracks were found in the sintered pellet 34-15B and 34-20B due to phase separation between glass and crystalline phases. The CTE of each phases are mismatch. The conductive electrode paste for preparing conductive surface can penetrate along the crack surface; consequently, the calculated electrical resistivity is lower by distance between electrodes, L is lower than measurement.

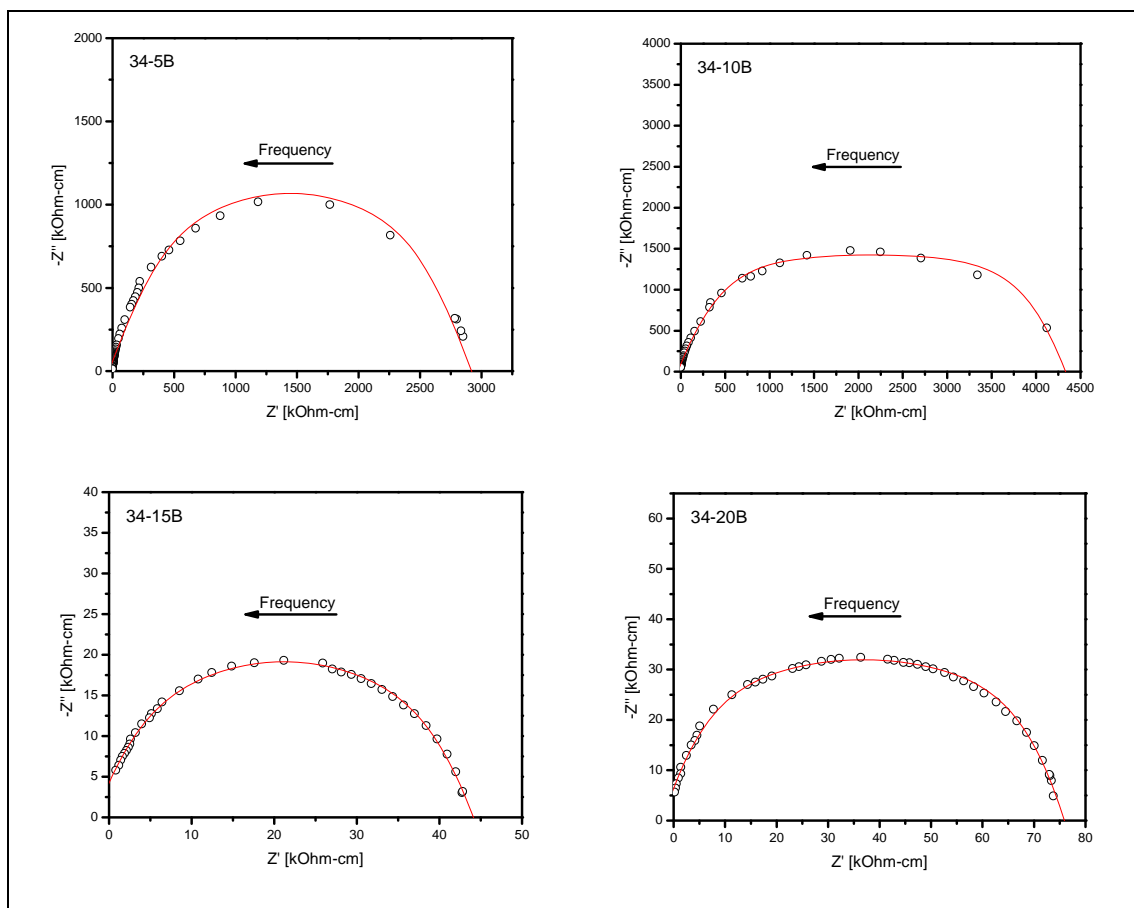


Fig. 4.45 Impedance spectra, in Nyquist diagram form, of glass-ceramics in 34 series at 800 °C

Fig. 4.46 shows impedance spectra of glass-ceramics in 35 series which their resistivity in range from $3.69 - 8.92 \times 10^5 \Omega \cdot \text{cm}$. The major conducting ion of this glass is Mg^{2+} and Ca^{2+} ions. Both ions have lower ionic mobility than major conductive ion in glass composition in Part I, which are Na^+ and K^+ ions. The electrical resistivity of glass-ceramics in this part is very higher than minimum requirement for SOFC sealant application ($> 1 \times 10^4 \Omega \cdot \text{cm}$) [36].

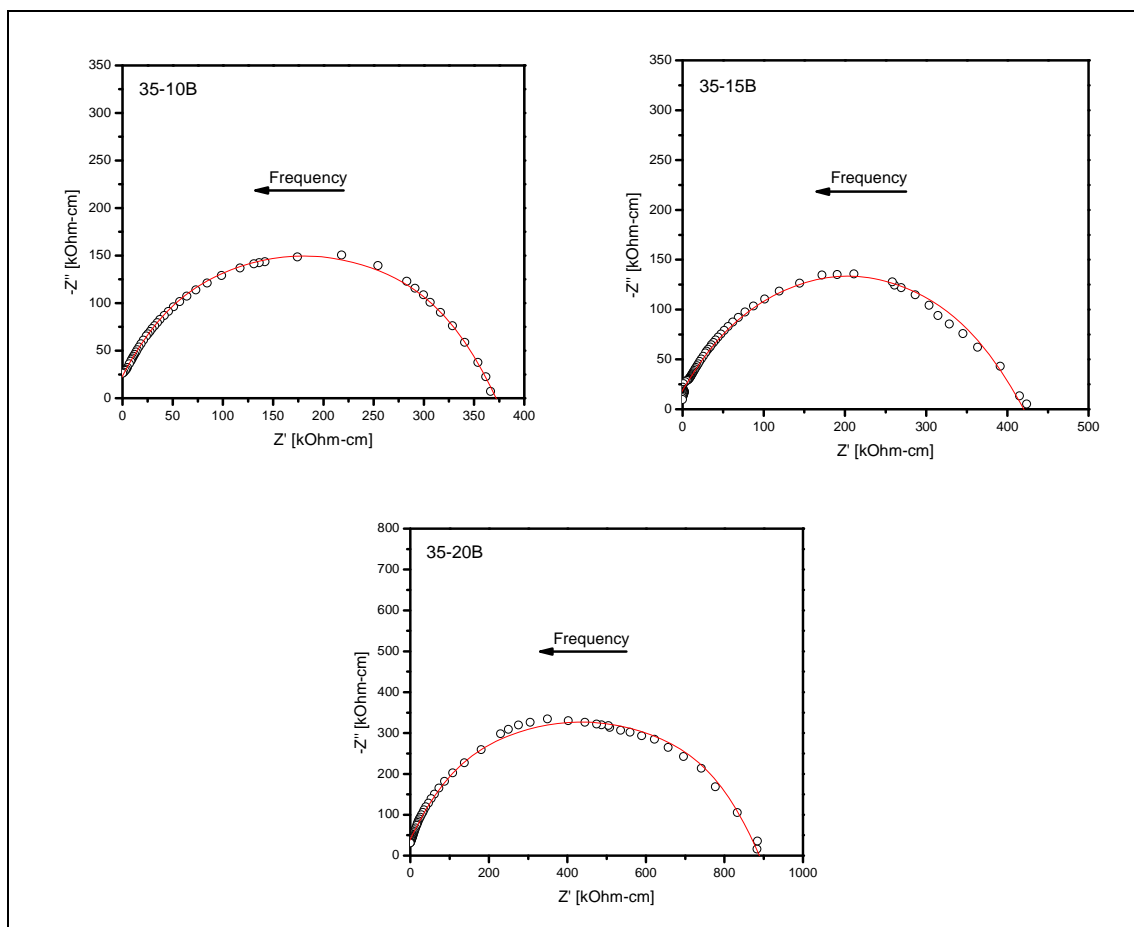


Fig. 4.46 Impedance spectra, in Nyquist diagram form, of glass-ceramics in 35 series at 800 °C

CHAPTER 5

CONCLUSION AND FUTURE WORK

5.1 Conclusion

Glass-ceramic sealants from barium-free silicate glass compositions were successfully developed following the pSOFC sealant requirements.

From the results of experimental procedure in the first part, glass-ceramics CM13 from the system $\text{Na}_2\text{O-MgO-CaO-Al}_2\text{O}_3\text{-SiO}_2$ could be joined with AISI430 stainless steel without any internal cracks after joining at 900 °C, 2 h. Its CTE slightly changed after heat treatment at 800 °C, 10 h from 12.98 to $12.45 \times 10^{-6} \text{ K}^{-1}$; this is still close to the CTE of AISI430 stainless steel. It does, however, not tightly bond to YSZ ceramic, because its CTE is higher than that of YSZ ($10.8 \times 10^{-6} \text{ K}^{-1}$). The electrical resistivity, measured by impedance spectroscopy, is the lowest in the CM1 series; however, this still meets the minimum requirement at 800 °C. The other glass-ceramic samples which could be joined with both AISI430 stainless steel and YSZ are CM22 (containing 5 mol% Na_2O and 5 mol% K_2O) and CM23 (containing 10 mol% Na_2O). Micro-cracks were found inside the glass-ceramics after joining due to a mismatch of CTE. Upon thermal treatment of glass-ceramics at 800 °C for 10 h, the crystallization of kaliophilite (KAlSiO_4) in the glass-ceramics raises the CTE; the effect is higher than with nepheline (NaAlSiO_4). Thus micro-cracks are formed due to the higher CTE mismatch between the stainless steel and the glass-ceramics.

In part II, the glass-ceramics based on the system $\text{MgO-CaO-Al}_2\text{O}_3\text{-SiO}_2$ were prepared; viscosity was adjusted by adding B_2O_3 from 0 to 20%. Glass-ceramics from glass composition 34 and 35 series which contained boron oxide 5–20 wt.% and 10-20 wt.%, respectively, can be joined tightly with Crofer22 APU stainless steel and also with YSZ. The results of thermal cycle test in combination with a helium gas leak test showed that they could pass through 10 thermal cycles (108 h) with leak rates in the order of 10^{-3} - $10^{-4} \text{ cm}^3 \cdot \text{min}^{-1} \cdot \text{cm}^{-1}$ only. The CTEs of glass-ceramics after long term thermal treatment at 800 °C for 100 h is slightly different from the initial glass-ceramics (obtained after

thermal treatment at 900 °C, 2 h). The increase of the boron oxide content in the glass compositions leads to a decrease of CTE after crystallization. This is due to the formation of the low-CTE phases diopside and anorthite. In the case of 20 wt.% boron oxide, an enhanced diffusion of Cr ions at the interface of glass-ceramics and Crofer22 APU stainless steel interface, and the formation of micro-cracks due to CTE mismatch is observed.

5.2 Future work

Barium free glass-ceramics from the system $\text{CaO-MgO-Al}_2\text{O}_3\text{-SiO}_2$ are potential candidate materials and their properties are comparable with BaO base glass and glass-ceramic sealants. Although their CTE is lower than Crofer22 APU stainless steel, it can be tailored by adding functional additives such as transition metal oxides. The chemical stability in both oxidizing and reducing environment needs to be investigated.

REFERENCES

- [1] Iwata, T. and Enami, Y. Analysis of fuel utilization performance of round substrate, planar solid oxide fuel cells. Journal of the Electrochemical Society 145 (1998): 931-935.
- [2] Weil, K. S. The state-of-the-art in sealing technology for solid oxide fuel cells. JOM 58 (2006): 37-44.
- [3] Bahadur, D., Lahl, N., Singh, K., Singheiser, L. and Hilpert, K. Influence of nucleating agents on the chemical interaction of MgO-Al₂O₃-SiO₂-B₂O₃ glass sealants with components of SOFCs. Journal of the Electrochemical Society 151 (2004): A558-A562.
- [4] Zeng, F. R., Gao, R. F., Mao, Z. Q. and Qiu, H. O. Structure and properties of BaO-Al₂O₃-B₂O₃ glass sealants. Chinese Journal of Inorganic Chemistry 24 (2008): 808-812.
- [5] Zheng, R., Wang, S. R., Nie, H. W. and Wen, T. L. SiO₂-CaO-B₂O₃-Al₂O₃ ceramic glaze as sealant for planar ITSOFC. Journal of Power Sources 128 (2004): 165-172.
- [6] Yang, Z., Meinhardt, K. D. and Stevenson, J. W. Chemical compatibility of barium-calcium-aluminosilicate-based sealing glasses with the ferritic stainless steel interconnect in SOFCs. Journal of the Electrochemical Society 150 (2003): A1095-A1101.
- [7] Haanappel, V. A. C., Shemet, V., Gross, S. M., Koppitz, T., Menzler, N. H., Zahid, M. and Quadackers, W. J. Behaviour of various glass-ceramic sealants with ferritic steels under simulated SOFC stack conditions. Journal of Power Sources 150 (2005): 86-100.
- [8] Lessing, P. A. A review of sealing technologies applicable to solid oxide electrolysis cells. Journal of Materials Science 42 (2007): 3465-3476.

- [9] Sohn, S. B., Choi, S. Y., Kim, G. H., Song, H. S. and Kim, G. D. Suitable Glass-Ceramic Sealant for Planar Solid-Oxide Fuel Cells. Journal of the American Ceramic Society 87 (2004): 254-260.
- [10] Fergus, J. W. Sealants for solid oxide fuel cells. Journal of Power Sources 147 (2005): 46-57.
- [11] Duquette, J. and Petric, A. Silver wire seal design for planar solid oxide fuel cell stack. Journal of Power Sources 137 (2004): 71-75.
- [12] Chou, Y. S., Stevenson, J. W. and Chick, L. A. Ultra-low leak rate of hybrid compressive mica seals for solid oxide fuel cells. Journal of Power Sources 112 (2002): 130-136.
- [13] Yang, Z., Stevenson, J. W. and Meinhardt, K. D. Chemical interactions of barium-calcium-aluminosilicate-based sealing glasses with oxidation resistant alloys. Solid State Ionics 160 (2003): 213-225.
- [14] Zhang, T., Zhang, H., Li, G. and Yung, H. Reduction of chromate formation at the interface of solid oxide fuel cells by different additives. Journal of Power Sources 195 (2010): 6795-6797.
- [15] Teng Zhang, W. G. F., Signo T. Reis, and Richard K. Brow. Borate Volatility from SOFC Sealing Glasses. Journal of the American Ceramic Society 91 (2008): 2564.
- [16] Nernst, W. Über die Elektrolytische Leitung Fester Körper bei sehr Hohen Temperaturen. Z. Elektrochem. 6 (1989): 41-43.
- [17] Bauer, E. and Preis, H. Über Brennstoff-Ketten mit Festleitern. Z. Elektrochem. 43 (1937): 727-732.
- [18] Sammes, N. Engineering materials and processes. Fuel cell technology: reaching towards commercialization. London: Springer-Verlag London Limited, 2006.

- [19] Minh, N. Q. Ceramic fuel cells. Journal of the American Ceramic Society 76 (1993): 563-588.
- [20] Du, Y. and Sammes, N. M. Fabrication and properties of anode-supported tubular solid oxide fuel cells. J. Power Sources 136 (2004): 66–71.
- [21] Yakabe, H., Baba, Y., Sakurai, T. and Yoshitaka, Y. Evaluation of the residual stress for anode supported SOFCs. J. Power Sources 135 (2004): 9–16.
- [22] Rohr, F. J. Solid Electrolytes. New York: Academic Press, 1978.
- [23] Weissbart, J. and Ruck, R. A solid electrolyte fuel cell. Journal of the Electrochemical Society 109 (1962): 723–726.
- [24] Singhal, S. C. and Kendall, K. High temperature solid oxide fuel cells: fundamentals, design and applications. Oxford: Elsevier Advanced Technology, 2003.
- [25] Gödickemeier, M. and Gauckler, L. J. Engineering of solid oxide fuel cells with ceria-based electrolytes. Journal of the Electrochemical Society 145 (1998): 414-421.
- [26] Wang, W. G. and Mogensen, M. High-performance lanthanum-ferrite-based cathode for SOFC. Solid State Ionics 176 (2005): 457-462.
- [27] Timurkutluk, B., Timurkutluk, C., Mat, M. D. and Kaplan, Y. Novel structured gadolinium doped ceria based electrolytes for intermediate temperature solid oxide fuel cells. Journal of Power Sources 196 (2011): 9361-9364.
- [28] Izuki, M., Brito, M. E., Yamaji, K., Kishimoto, H., Cho, D. H., Shimonosono, T., Horita, T. and Yokokawa, H. Interfacial stability and cation diffusion across the LSCF/GDC interface. Journal of Power Sources 196 (2011): 7232-7236.
- [29] Akashi, T., Maruyama, T. and Goto, T. Transport of lanthanum ion and hole in LaCrO₃ determined by electrical conductivity measurements. Solid State Ionics 164 (2003): 177-183.

- [30] Jeffrey W, F. Lanthanum chromite-based materials for solid oxide fuel cell interconnects. Solid State Ionics 171 (2004): 1-15.
- [31] Fuel Cell Handbook seventh edition. West Virginia: US Department of Energy (DOE) National Energy Technology Laboratory, 2004.
- [32] Chou, Y. S. and Stevenson, J. W. Novel silver/mica multilayer compressive seals for solid-oxide fuel cells: The effect of thermal cycling and material degradation on leak behavior. Journal of Materials Research 18 (2003): 2243-2250.
- [33] Mahapatra, M. K. and Lu, K. Glass-based seals for solid oxide fuel and electrolyzer cells - A review. Materials Science and Engineering R: Reports 67 (2010): 65-85.
- [34] Lara, C., Pascual, M. J. and Duran, A. Glass-forming ability, sinterability and thermal properties in the systems RO-BaO-SiO₂ (R = Mg, Zn). Journal of Non-Crystalline Solids 348 (2004): 149-155.
- [35] Wang, R., Lü, Z., Liu, C., Zhu, R., Huang, X., Wei, B., Ai, N. and Su, W. Characteristics of a SiO₂-B₂O₃-Al₂O₃-BaCO₃-PbO₂-ZnO glass-ceramic sealant for SOFCs. Journal of Alloys and Compounds 432 (2007): 189-193.
- [36] Lara, C., Pascual, M. J., Keding, R. and Durán, A. Electrical behaviour of glass-ceramics in the systems RO-BaO-SiO₂ (R = Mg, Zn) for sealing SOFCs. Journal of Power Sources 157 (2006): 377-384.
- [37] Tietz, F. Thermal expansion of SOFC materials. Ionics 5 (1999): 129-139.
- [38] Nielsen, K. A., Solvang, M., Poulsen, F. W. and Larsen, P. H., Evaluation of sodium aluminosilicate glass composite seal with magnesia filler, in: E. Lara-Curzio and M. J. Readey '(Ed.)'^(Eds.)', 25, Cocoa Beach, FL, 2004, 309-314.
- [39] Meinhardt, K. D., Kim, D. S., Chou, Y. S. and Weil, K. S. Synthesis and properties of a barium aluminosilicate solid oxide fuel cell glass-ceramic sealant. Journal of Power Sources 182 (2008): 188-196.

- [40] Steele, B. C. H. and Heinzl, A. Materials for fuel-cell technologies. Nature 414 (2001): 345-352.
- [41] Fergus, J. W. Materials challenges for solid-oxide fuel cells. JOM 59 (2007): 56-62.
- [42] Reis, S. T. and Brow, R. K. Designing sealing glasses for solid oxide fuel cells. Journal of Materials Engineering and Performance 15 (2006): 410-413.
- [43] Singh, R. N. Sealing technology for solid oxide fuel cells (SOFC). International Journal of Applied Ceramic Technology 4 (2007): 134-144.
- [44] Kilner, J., Edwards, P. and Kuznetsov, V. Cell-ing future power. Materials World 17 (2009): 36-38.
- [45] Donald, I. W., Mallinson, P. M., Metcalfe, B. L., Gerrard, L. A. and Fernie, J. A. Recent developments in the preparation, characterization and applications of glass- and glass-ceramic-to-metal seals and coatings. Journal of Materials Science 46 (2011): 1975-2000.
- [46] Pascual, M. J., Guillet, A. and Durán, A. Optimization of glass-ceramic sealant compositions in the system MgO-BaO-SiO₂ for solid oxide fuel cells (SOFC). Journal of Power Sources 169 (2007): 40-46.
- [47] Piao, J. H., Sun, K. N., Zhang, N. Q., Chen, X. B. and Zhou, D. R. Sealing glass of barium-calcium-aluminosilicate system for solid oxide fuel cells. Journal of Rare Earths 25 (2007): 434-438.
- [48] Goel, A., Tulyaganov, D. U., Ferrari, A. M., Shaaban, E. R., Prange, A., Bondioli, F. and Ferreira, J. M. F. Structure, Sintering, and Crystallization Kinetics of Alkaline-Earth Aluminosilicate Glass-Ceramic Sealants for Solid Oxide Fuel Cells. Journal of the American Ceramic Society 93 (2010): 830-837.
- [49] Goel, A., Tulyaganov, D. U., Pascual, M. J., Shaaban, E. R., Munoz, F., Lu, Z. and Ferreira, J. M. F. Development and performance of diopside based glass-ceramic sealants for solid oxide fuel cells. Journal of Non-Crystalline Solids 356 (2010): 1070-1080.

- [50] Brochu, M., Gauntt, B. D., Shah, R., Miyake, G. and Loehman, R. E. Comparison between barium and strontium-glass composites for sealing SOFCs. Journal of the European Ceramic Society 26 (2006): 3307-3313.
- [51] Mahapatra, M. K., Lu, K. and Reynolds Jr, W. T. Thermophysical properties and devitrification of SrO-La₂O₃-Al₂O₃-B₂O₃-SiO₂-based glass sealant for solid oxide fuel/electrolyzer cells. Journal of Power Sources 179 (2008): 106-112.
- [52] Laorodphan, N., Namwong, P., Thiemsorn, W., Jaimasith, M., Wannagon, A. and Chairuang Sri, T. A low silica, barium borate glass-ceramic for use as seals in planar SOFCs. Journal of Non-Crystalline Solids 355 (2009): 38-44.
- [53] Sakuragi, S., Funahashi, Y., Suzuki, T., Fujishiro, Y. and Awano, M. Non-alkaline glass-MgO composites for SOFC sealant. Journal of Power Sources 185 (2008): 1311-1314.
- [54] Choi, S. R., Bansal, N. P. and Garg, A. Mechanical and microstructural characterization of boron nitride nanotubes-reinforced SOFC seal glass composite. Materials Science and Engineering A 460-461 (2007): 509-515.
- [55] Brochu, M., Gauntt, B. D., Shah, R. and Loehman, R. E. Comparison between micrometer- and nano-scale glass composites for sealing solid oxide fuel cells. Journal of the American Ceramic Society 89 (2006): 810-816.
- [56] Suda, S., Matsumiya, M., Kawahara, K. and Jono, K. Thermal cycle reliability of glass/ceramic composite gas sealing materials. International Journal of Applied Ceramic Technology 7 (2010): 49-54.
- [57] Deng, X., Duquette, J. and Petric, A. Silver-glass composite for high temperature sealing. International Journal of Applied Ceramic Technology 4 (2007): 145-151.
- [58] Batfalsky, P., Haanappel, V. A. C., Malzbender, J., Menzler, N. H., Shemet, V., Vinke, I. C. and Steinbrech, R. W. Chemical interaction between glass-ceramic sealants and interconnect steels in SOFC stacks. Journal of Power Sources 155 (2006): 128-137.

- [59] Liu, W., Sun, X. and Khaleel, M. A. Predicting Young's modulus of glass/ceramic sealant for solid oxide fuel cell considering the combined effects of aging, microvoids and self-healing. Journal of Power Sources 185 (2008): 1193-1200.
- [60] Chou, Y. S., Stevenson, J. W. and Singh, P. Effect of pre-oxidation and environmental aging on the seal strength of a novel high-temperature solid oxide fuel cell (SOFC) sealing glass with metallic interconnect. Journal of Power Sources 184 (2008): 238-244.
- [61] Mahapatra, M. K. and Lu, K. Interfacial study of Crofer 22 APU interconnect-SABS-0 seal glass for solid oxide fuel/electrolyzer cells. Journal of Materials Science 44 (2009): 5569-5578.
- [62] Peng, L. and Zhu, Q. Thermal cycle stability of BaO-B₂O₃-SiO₂ sealing glass. Journal of Power Sources 194 (2009): 880-885.
- [63] Smeacetto, F., Salvo, M., D'Hérin Bytner, F. D., Leone, P. and Ferraris, M. New glass and glass-ceramic sealants for planar solid oxide fuel cells. Journal of the European Ceramic Society 30 (2010): 933-940.
- [64] Smeacetto, F., Salvo, M., Ferraris, M., Cho, J. and Boccaccini, A. R. Glass-ceramic seal to join Crofer 22 APU alloy to YSZ ceramic in planar SOFCs. Journal of the European Ceramic Society 28 (2008): 61-68.
- [65] Kumar, V., Arora, A., Pandey, O. P. and Singh, K. Studies on thermal and structural properties of glasses as sealants for solid oxide fuel cells. International Journal of Hydrogen Energy 33 (2008): 434-438.
- [66] Smeacetto, F., Chrysanthou, A., Salvo, M., Zhang, Z. and Ferraris, M. Performance and testing of glass-ceramic sealant used to join anode-supported-electrolyte to Crofer22APU in planar solid oxide fuel cells. Journal of Power Sources 190 (2009): 402-407.
- [67] Milhans, J., Khaleel, M., Sun, X., Tehrani, M., Al-Haik, M. and Garmestani, H. Creep properties of solid oxide fuel cell glass-ceramic seal G18. Journal of Power Sources 195 (2010): 3631-3635.

- [68] Liu, W. N., Sun, X., Koepfel, B. and Khaleel, M. Experimental study of the aging and self-healing of the glass/ceramic sealant used in SOFCs. International Journal of Applied Ceramic Technology 7 (2010): 22-29.
- [69] Mahapatra, M. K. and Lu, K. Thermochemical compatibility of a seal glass with different solid oxide cell components. International Journal of Applied Ceramic Technology 7 (2010): 10-21.
- [70] Goel, A., Pascual, M. J. and Ferreira, J. M. F. Stable glass-ceramic sealants for solid oxide fuel cells: Influence of Bi₂O₃ doping. International Journal of Hydrogen Energy 35 (2010): 6911-6923.
- [71] Chou, Y. S., Stevenson, J. W. and Choi, J. P. Alkali Effect on the Electrical Stability of a Solid Oxide Fuel Cell Sealing Glass. Journal of the Electrochemical Society 157 (2010): B348-B353.
- [72] Brow, R. K. and Tallant, D. R. Structural design of sealing glasses. Journal of Non-Crystalline Solids 222 (1997): 396-406.
- [73] Smeacetto, F., Salvo, M., Bytner, F. D. D., Leone, P. and Ferraris, M. New glass and glass-ceramic sealants for planar solid oxide fuel cells. Journal of the European Ceramic Society 30 (2010): 933-940.
- [74] Ghosh, S., Das Sharma, A., Kundu, P., Mahanty, S. and Basu, R. N. Development and characterizations of BaO-CaO-Al₂O₃-SiO₂ glass-ceramic sealants for intermediate temperature solid oxide fuel cell application. Journal of Non-Crystalline Solids 354 (2008): 4081-4088.
- [75] Goel, A., Tulyaganov, D. U., Kharton, V. V., Yaremchenko, A. A. and Ferreira, J. M. F. The effect of Cr₂O₃ addition on crystallization and properties of La₂O₃-containing diopside glass-ceramics. Acta Materialia 56 (2008): 3065-3076.
- [76] Goel, A., Tulyaganov, D. U., Kharton, V. V., Yaremchenko, A. A., Eriksson, S. and Ferreira, J. M. F. Optimization of La₂O₃-containing diopside based glass-ceramic sealants for fuel cell applications. Journal of Power Sources 189 (2009): 1032-1043.

- [77] Chou, Y. S., Stevenson, J. W. and Meinhardt, K. D. Electrical stability of a novel refractory sealing glass in a dual environment for solid oxide fuel cell applications. Journal of the American Ceramic Society 93 (2010): 618-623.
- [78] Zhang, T., Fahrenholtz, W. G., Reis, S. T. and Brow, R. K. Borate volatility from SOFC sealing glasses. Journal of the American Ceramic Society 91 (2008): 2564-2569.
- [79] Goel, A., Tulyaganov, D. U., Kharton, V. V., Yaremchenko, A. A. and Ferreira, J. M. F. Electrical behavior of aluminosilicate glass-ceramic sealants and their interaction with metallic solid oxide fuel cell interconnects. Journal of Power Sources 195 (2010): 522-526.
- [80] Ghosh, S., Sharma, A. D., Mukhopadhyay, A. K., Kundu, P. and Basu, R. N. Effect of BaO addition on magnesium lanthanum alumino borosilicate-based glass-ceramic sealant for anode-supported solid oxide fuel cell. International Journal of Hydrogen Energy 35 (2010): 272-283.
- [81] Wang, S. F., Wang, Y. R., Hsu, Y. F. and Chuang, C. C. Effect of additives on the thermal properties and sealing characteristic of BaO-Al₂O₃-B₂O₃-SiO₂ glass-ceramic for solid oxide fuel cell application. International Journal of Hydrogen Energy 34 (2009): 8235-8244.
- [82] Sun, T., Xiao, H., Guo, W. and Hong, X. Effect of Al₂O₃ content on BaO-Al₂O₃-B₂O₃-SiO₂ glass sealant for solid oxide fuel cell. Ceramics International 36 (2010): 821-826.
- [83] Widgeon, S. J., Corral, E. L., Spilde, M. N. and Loehman, R. E. Glass-to-Metal seal interfacial analysis using electron probe microscopy for reliable solid oxide fuel cells. Journal of the American Ceramic Society 92 (2009): 781-786.
- [84] Stephens, E. V., Vetrano, J. S., Koepfel, B. J., Chou, Y., Sun, X. and Khaleel, M. A. Experimental characterization of glass-ceramic seal properties and their constitutive implementation in solid oxide fuel cell stack models. Journal of Power Sources 193 (2009): 625-631.

- [85] Donald, I. W. Preparation, properties and chemistry of glass- and glass-ceramic-to-metal seals and coatings. Journal of Materials Science 28 (1993): 2841-2886.
- [86] Story, C., Lu, K., Reynolds Jr, W. T. and Brown, D. Shape memory alloy/glass composite seal for solid oxide electrolyzer and fuel cells. International Journal of Hydrogen Energy 33 (2008): 3970-3975.
- [87] Jiang, S. P., Zhen, Y. D. and Zhang, S. Interaction between Fe-Cr metallic interconnect and (La, Sr) MnO₃/YSZ composite cathode of solid oxide fuel cells. Journal of the Electrochemical Society 153 (2006): A1511-A1517.
- [88] Yang, Z., Weil, K. S., Paxton, D. M. and Stevenson, J. W. Selection and Evaluation of Heat-Resistant Alloys for SOFC Interconnect Applications. Journal of the Electrochemical Society 150 (2003): A1188-A1201.
- [89] Geasee, P. Development of crystallizing glass sealants for high temperature planar solid oxide fuel cells. Doctoral Thesis, Fakultät für Bergbau, Hüttenwesen und Geowissenschaften, Aachen, Germany, RWTH Aachen, 2003.
- [90] Volf, M. B. CHEMICAL APPROACH TO GLASS. Elsevier, 1984.
- [91] Scholze, H. and Nature, G. Glass Nature, Structure, and Properties. New York: Springer Verlag, 1991.
- [92] Shelby, J. E. Introduction to Glass Science and Technology. Cambridge: The Royal Society of Chemistry, 2005.
- [93] Yang, Z. G., Weil, K. S., Paxton, D. M. and Stevenson, J. W. Selection and evaluation of heat-resistant alloys for SOFC interconnect applications. Journal of the Electrochemical Society 150 (2003): A1188-A1201.
- [94] Smeacetto, F., Salvo, M., Ferraris, M., Casalegno, V., Asinari, P. and Chrysanthou, A. Characterization and performance of glass-ceramic sealant to join metallic interconnects to YSZ and anode-supported-electrolyte in planar SOFCs. Journal of the European Ceramic Society 28 (2008): 2521-2527.

- [95] Sohn, S. B., Choi, S. Y., Kim, G. H., Song, H. S. and Kim, G. D. Stable sealing glass for planar solid oxide fuel cell. Journal of Non-Crystalline Solids 297 (2002): 103-112.
- [96] Chou, Y. S., Stevenson, J. W. and Singh, P. Effect of aluminizing of Cr-containing ferritic alloys on the seal strength of a novel high-temperature solid oxide fuel cell sealing glass. Journal of Power Sources 185 (2008): 1001-1008.
- [97] Smeacetto, F., Salvo, M., Ferraris, A., Casalegno, V., Asinari, P. and Chrysanthou, A. Characterization and performance of glass-ceramic sealant to join metallic interconnects to YSZ and anode-supportbd-electrolyte in planar SOFCs. Journal of the European Ceramic Society 28 (2008): 2521-2527.
- [98] Chou, Y. S. and Stevenson, J. W. Phlogopite mica-based compressive seals for solid oxide fuel cells: Effect of mica thickness. Journal of Power Sources 124 (2003): 473-478.
- [99] Ghosh, S., Das Sharma, A., Kundu, P. and Basu, R. N. Glass-ceramic sealants for planar IT-SOFC: A bilayered approach for joining electrolyte and metallic interconnect. Journal of the Electrochemical Society 155 (2008): B473-B478.
- [100] Chou, Y. S., Stevenson, J. W. and Gow, R. N. Novel alkaline earth silicate sealing glass for SOFC - Part II. Sealing and interfacial microstructure. Journal of Power Sources 170 (2007): 395-400.
- [101] Kingery, W. D., Bowen, H. K. and Uhlmann, D. R. Introduction to Ceramics, 2nd ed. John Wiley and Sons Inc., 1976.
- [102] Lara, C., Pascual, M. J. and Duran, A. Glass and glass-ceramic sealants for solid oxide fuel cells (SOFC). Boletin De La Sociedad Espanola De Ceramica Y Vidrio 42 (2003): 133-143.
- [103] ASTM E 1356-03. Standard Test Method for Glass Transition Temperatures. ASTM International, 2000.

- [104] Merlini, M., Gemmi, M. and Artioli, G. Thermal expansion and phase transitions in akermanite and gehlenite. Physics and Chemistry of Minerals 32 (2005): 189-196.
- [105] Tulyaganov, D. U., Agathopoulos, S., Ventura, J. M., Karakassides, M. A., Fabrichnaya, O. and Ferreira, J. M. F. Synthesis of glass-ceramics in the CaO-MgO-SiO₂ system with B₂O₃, P₂O₅, Na₂O and CaF₂ additives. Journal of the European Ceramic Society 26 (2006): 1463-1471.
- [106] Ventura, J. M. G., Tulyaganov, D. U., Agathopoulos, S. and Ferreira, J. M. F. Sintering and crystallization of akermanite-based glass-ceramics. Materials Letters 60 (2006): 1488-1491.
- [107] Conradt, R. Modeling of the thermochemical properties of multicomponent oxide melts. Zeitschrift fuer Metallkunde/Materials Research and Advanced Techniques 92 (2001): 1158-1162.
- [108] Verma, S. P., Torres-Alvarado, I. S. and Velasco-Tapia, F. A revised CIPW norm. Schweizerische Mineralogische und Petrographische Mitteilungen 83 (2003): 197-216.
- [109] Pruseth, K. L. MATNORM: Calculating NORM using composition matrices. Computers and Geosciences 35 (2009): 1785-1788.
- [110] Bale, C. W., Chartrand, P., Degterov, S. A., Eriksson, G., Hack, K., Ben Mahfoud, R., Melançon, J., Pelton, A. D. and Petersen, S. FactSage thermochemical software and databases. Calphad: Computer Coupling of Phase Diagrams and Thermochemistry 26 (2002): 189-228.
- [111] Pascual, M. J., Duran, A. and Prado, M. O. A new method for determining fixed viscosity points of glasses. Physics and Chemistry of Glasses 46 (2005): 512-520.
- [112] Eldin, F. M. E. and El Alaily, N. A. Electrical conductivity of some alkali silicate glasses. Materials Chemistry and Physics 52 (1998): 175-179.

- [113] Ota, T., Yamai, I. and Zhang, S. High-thermal-expansion NaAlSiO₄ ceramics. Nippon Seramikkusu Kyokai Gakujutsu Ronbunshi/Journal of the Ceramic Society of Japan 100 (1992): 1361-1365.
- [114] Ota, T., Yamai, I. and Suzuki, H. THERMAL-EXPANSION OF NEPHELINE SOLID-SOLUTIONS IN THE SYSTEM OF Na₁₋₂XCaXAlSiO₄. Journal of Materials Science Letters 13 (1994): 393-394.
- [115] Ota, T., Takebayashi, T., Takahashi, M., Hikichi, Y. and Suzuki, H. High thermal expansion KAISiO₄ ceramic. Journal of Materials Science 31 (1996): 1431-1433.
- [116] Wang, S.-f., Wang, Yun-ruey, Chuang, Ching-chin, Yeh, Chun-ting Glass-Ceramic Composite Encapsulation Material. United States Patent Application, Paten Application Publication, United States, 20100273632, 2010
- [117] Bauerle, J. E. Study of solid electrolyte polarization by a complex admittance method. Journal of Physics and Chemistry of Solids 30 (1969): 2657-2670.
- [118] Guo, X. and Zhang, Z. Grain size dependent grain boundary defect structure: Case of doped zirconia. Acta Materialia 51 (2003): 2539-2547.
- [119] Lanfredi, S. and Rodrigues, A. C. M. Impedance spectroscopy study of the electrical conductivity and dielectric constant of polycrystalline LiNbO₃. Journal of Applied Physics 86 (1999): 2215-2219.

APPENDICES

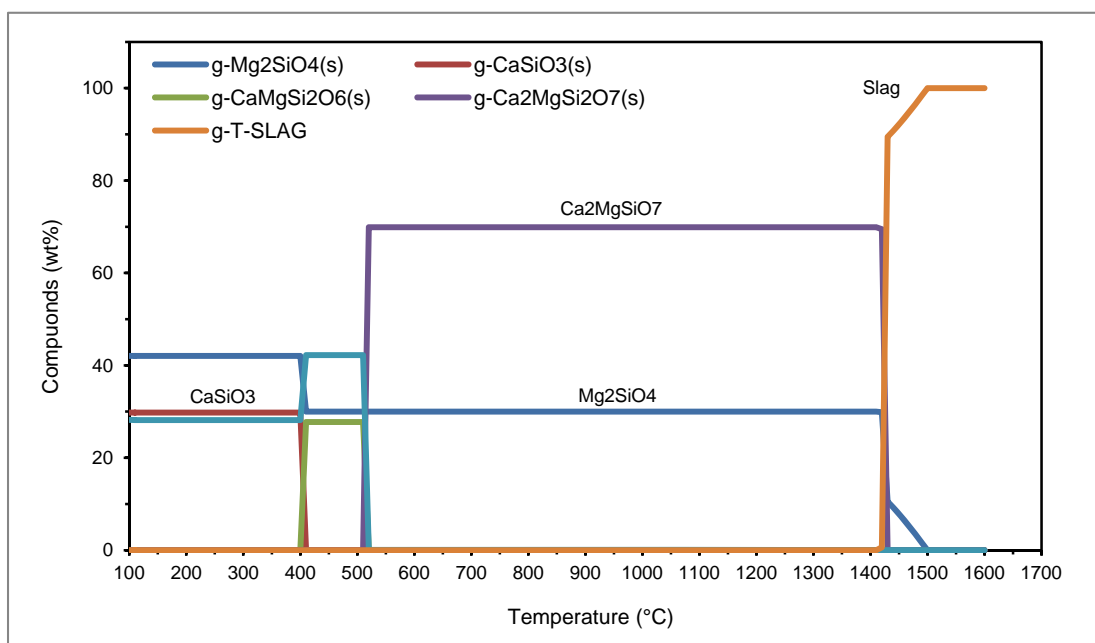
APPENDIX A

Detail of batch chemicals used in glass preparation

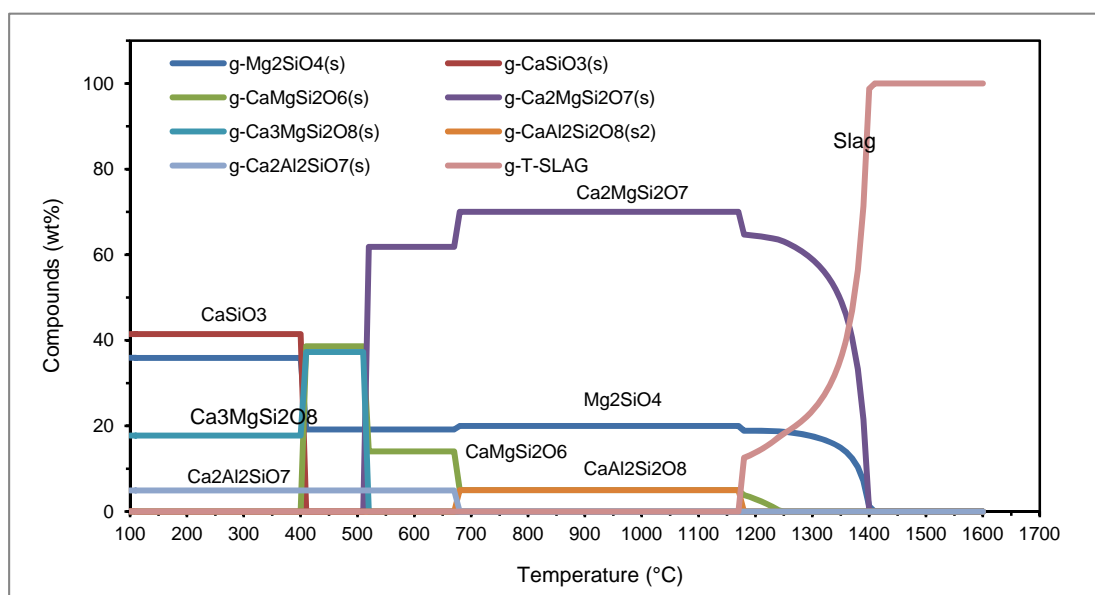
Chemicals	Suppliers	Purity (%pure)
SiO ₂ (pure precipitated)	Ajex Finechem Pty, New Zealand	≥98
Silica sand	Commercial grade	≥95
Al ₂ O ₃ (calcined)	APS, Australia	≥95%
Al ₂ O ₃ (calcined)	Merk, Germany	≥99%
HB ₂ O ₃	Fisher, United Kingdom	99.99
MgCO ₃	Fluka, Switzerland	40.0% MgO
MgCO ₃ Mg(OH) ₂ 5H ₂ O	Merk, Germany	≥40% MgO
CaCO ₃	Fluka, Switzerland	≥99%
CaCO ₃	Merk, Germany	≥99%
ZnO	Fluka, Switzerland	≥99
Bi ₂ O ₃	Fluka, Spain	
Na ₂ CO ₃	Fluka, Switzerland	≥99%
K ₂ CO ₃	APS, Australia	≥99%
Ethyl Cellulose	Wako Pure Chemical Industries, Japan	abt.49% ethoxy 45
Polyvinyl Alcohol BF17W	Ajex Finechem Pty, New Zealand	
Terpineol	Sigma-Aldrich, Singapore	>60% alpha- terpineol, ≤0.5% water

APPENDIX B

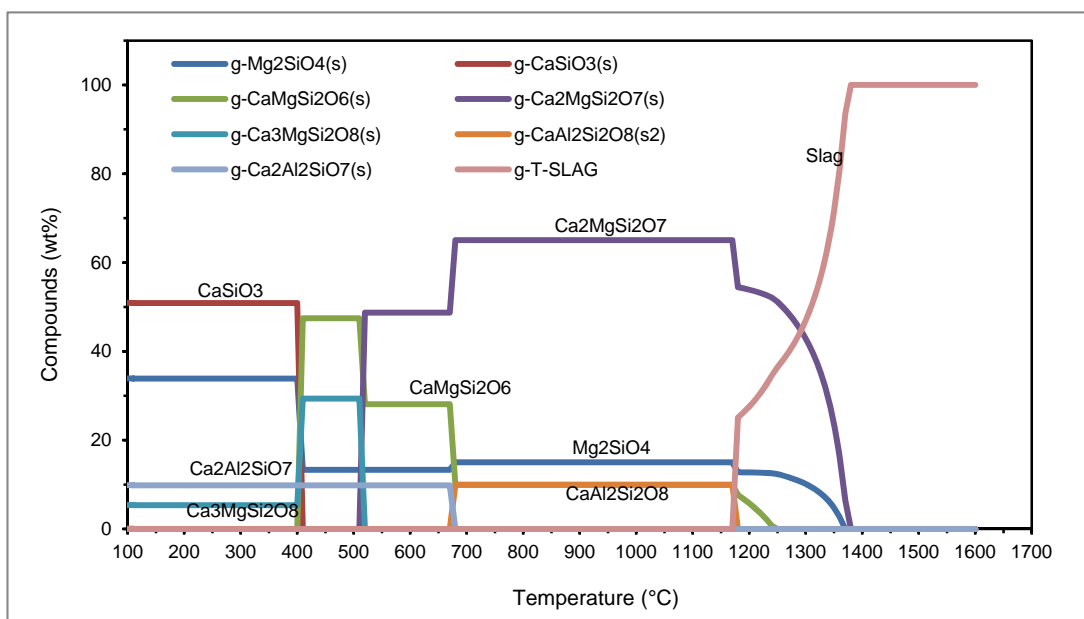
Equilibrium plot of Constitutional Compounds of glass 31-37 calculated by FactSage software.



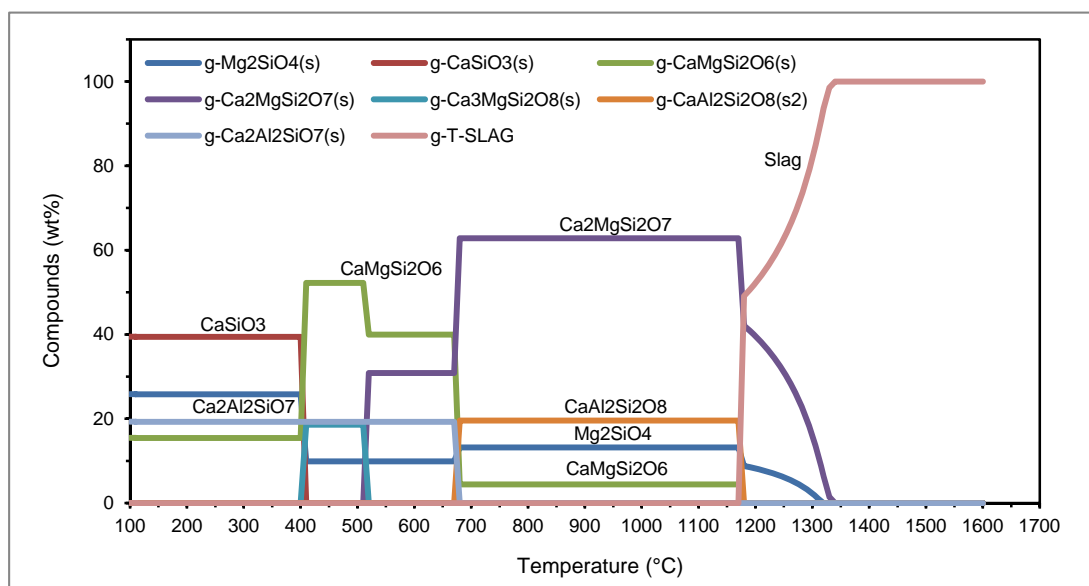
Equilibrium plot of Constitutional Compounds of glass 31 composition calculated by FactSage



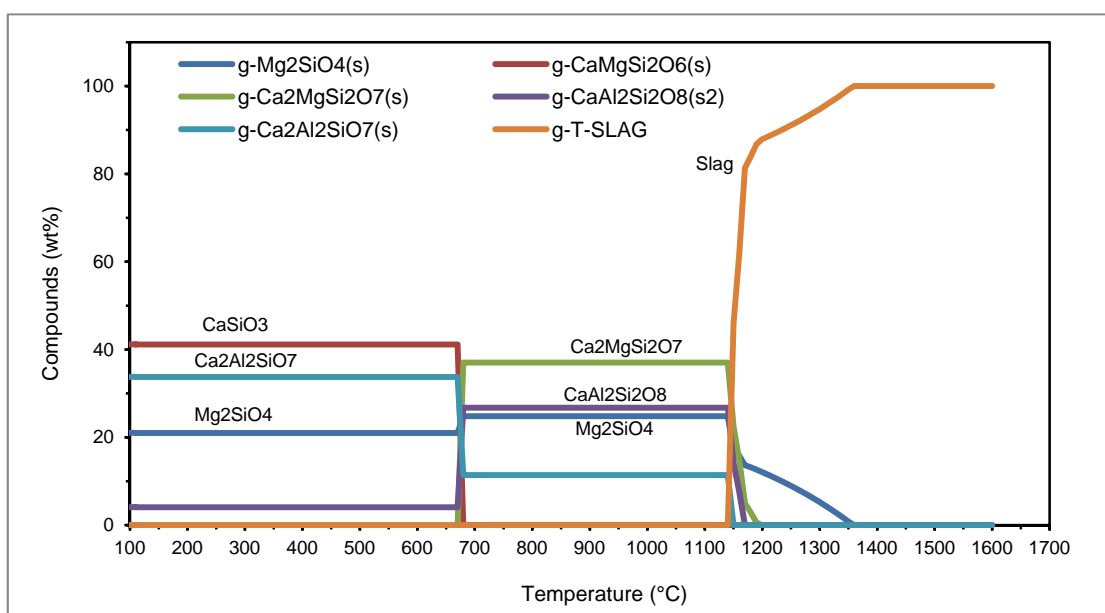
Equilibrium plot of Constitutional Compounds of glass 32 calculated by FactSage



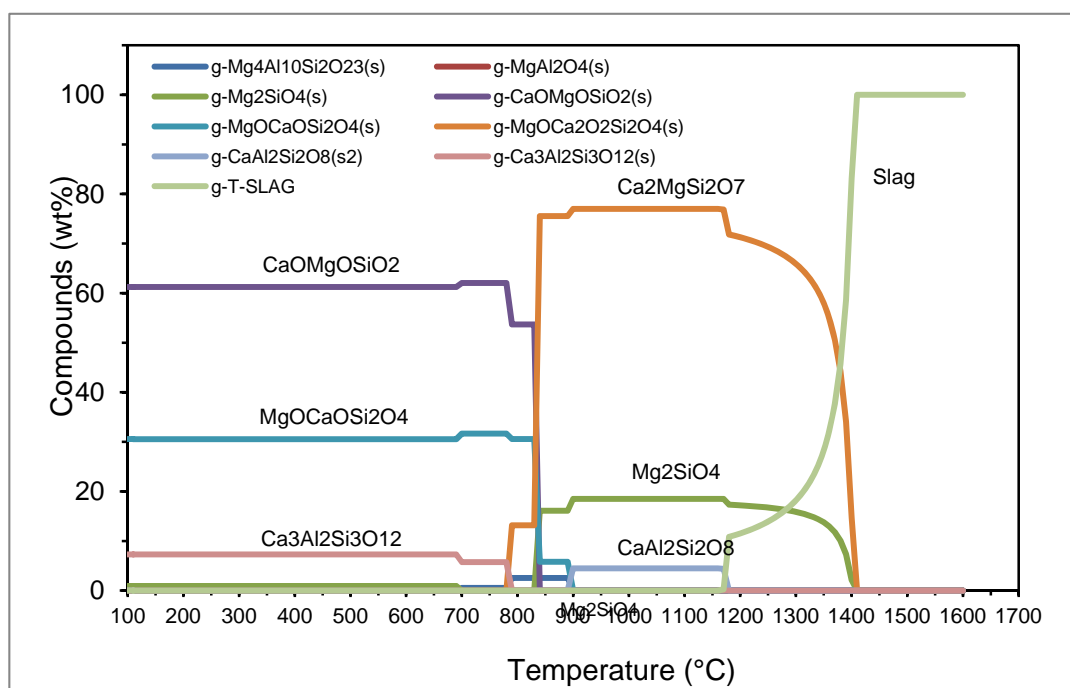
Equilibrium plot of Constitutional Compounds of glass 33 calculated by FactSage



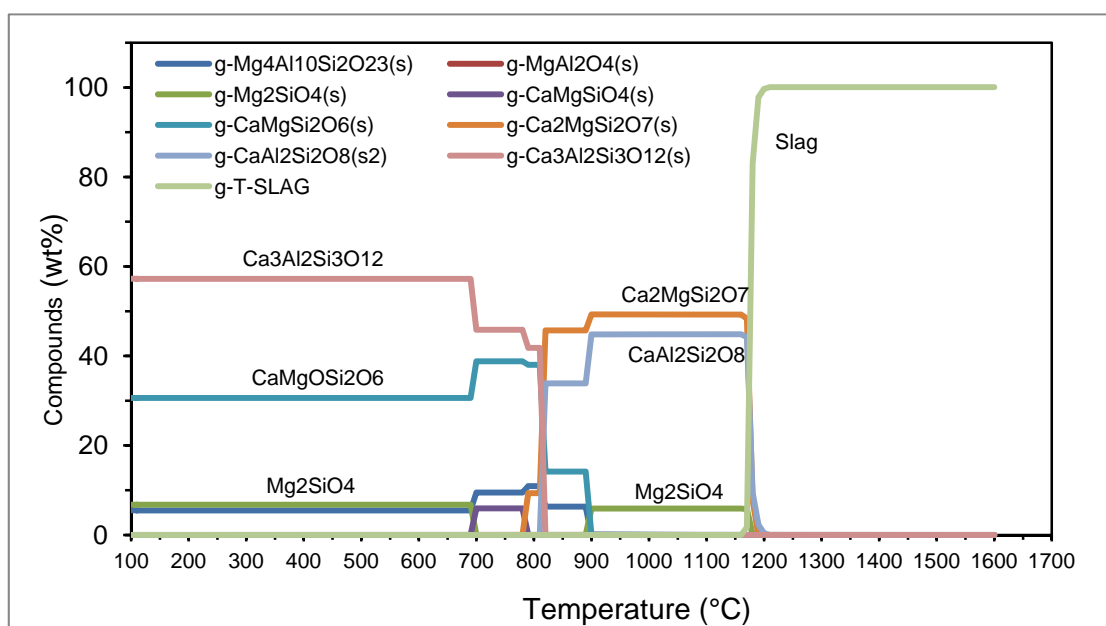
Equilibrium plot of Constitutional Compounds of glass 34 calculated by FactSage



Equilibrium plot of Constitutional Compounds of glass 35 calculated by FactSage



Equilibrium plot of Constitutional Compounds of 36 calculated by FactSage



Equilibrium plot of Constitutional Compounds of 37 calculated by FactSage

APPENDIX C

Description and some specifications of AISI 430 stainless steel or TNX SC17
(product of Thainox Stainless Public Company Limited, Thailand)

TISI (THAILAND)	SST 430
JIS (JAPAN)	SUS 430
AISI (USA)	430
EURONORM (EUROPE)	X6Cr17 - 1.4016

CHEMICAL COMPOSITION

According to ASTM A240 / A240M - 04a⁶¹

Alloys	C	Mn	Si	Cr	Ni
%	< 0.12	< 1.0	< 0.75	16 - 18	< 0.75

CORROSION RESISTANCE

- TNX SC17 offers a good resistance to corrosion in many applications:
 - domestic environments, although cleaning is required from time to time to preserve the initial attractive appearance
 - food products for domestic uses
 - soaps, detergents and cold alkaline solutions
 - numerous organic substances such as phenol, petroleum, alcohols
- care must however be taken to prevent pitting corrosion in case of halides (chlorides, fluorides...): limit of temperature, duration of contact, cleaning and rinsing after use should be observed.
- TNX SC17 has acceptable resistance to nitric acid up to 65 % and 50 °C, weak organic acids at 20 °C (oxalic, formic < 5 %), caustics solutions (10 % up to boiling point, 50 % at 20 °C.)
- the use of strong acids (sulphuric, hydrochloric...) in service or as cleaning agents is not recommended.
- TNX SC17 is not sensitive to stress corrosion cracking.
- TNX SC17 is able to withstand oxidation under conditions of continuous service up to 800 °C.



Thainox Stainless Public Company Limited

Head Office:
31/F Unit 3101-3 CRC Tower, All Seasons Place,
87/2 Wireless Road, Lumpini, Pathumwan, Bangkok 10330, Thailand
Tel. (66 2) 250 7621-32 Fax (66 2) 250 7633

Rayong Plant:
324 Moo 8, Highway No. 3191 Road, Tambol Mabkha,
Ging Amphor Nikompattana, Rayong 21180, Thailand
Tel. (66 38) 636 125-32 Fax (66 38) 636 099
Website: www.thainox.com

APPENDIX D

Description and some specifications of Crofer 22 APU stainless steel (product of ThyssenKrupp VDM GmbH, Germany)

Designations and standards

Country	Material designation	Spezifikation			
		Chemical composition	Sheet & Plate	Strip	Wire
National standard					
D	W.-Nr. 1.4760				
DIN EN	X1CrTiLa22				
USA	UNS S44535				
ASTM		A 240	A 240		

Table 1 - Designations and standards.

Chemical composition

	Cr	Fe	C	Mn	Si	Cu	Al	S	P	Ti	La
min.	20,0	bal.		0,30						0,03	0,04
max.	24,0		0,03	0,80	0,50	0,50	0,50	0,020	0,050	0,20	0,20

Table 2 - Chemical composition (wt.-%).

* ThyssenKrupp VDM GmbH produces Crofer 22 APU (APU = Auxiliary Power Unit) under licence from Forschungszentrum Jülich.

Physical properties

Density	7.7 g/cm ³	0.278 lb/in. ³
Melting range	1510 (Solidus) - 1530 °C (Liquidus)	2750 (Solidus) - 2786 °F (Liquidus)

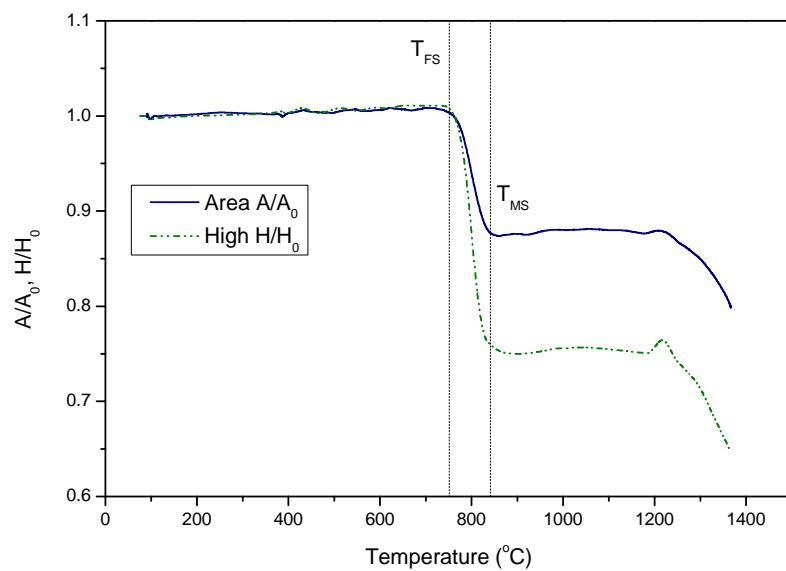
Temperature (T)		Specific heat		Thermal conductivity		Electrical resistivity		Modulus of elasticity		Coefficient of thermal expansion between 20 °C/68 °F and T	
°C	°F	$\frac{J}{kg \cdot K}$	$\frac{Btu}{lb \cdot ^\circ F}$	$\frac{W}{m \cdot K}$	$\frac{Btu \cdot in.}{ft^2 \cdot h \cdot ^\circ F}$	$\mu\Omega \cdot cm$	$\Omega \cdot circ \cdot mil$ ft	$\frac{kN}{mm^2}$	10 ³ ksi	$\frac{10^{-4}}{K}$	$\frac{10^{-4}}{^\circ F}$
25	77	470	0.112	26	180	55	330	220	31.9		
200	392	520	0.124	23	160	70	421	210	30,5	10,3	5,7
400	752	610	0.146	23	160	90	541	195	28,3	10,8	6,0
500	932							183	26,5	11,2	6,2
600	1112					105	632			11,4	6,3
700	1292									11,6	6,4
800	1472	660	0.158	24	166	115	692			11,9	6,6
900	1652									12,3	6,8
1000	1832	650	0.155	27	187	120	722			12,7	7,1

ThyssenKrupp VDM GmbH
 Plettenbergerstrasse 2
 58791 Werdohl
 P.O. Box 18 20
 58778 Werdohl
 Germany
 Phone: +49 23 92 55-0
 Fax: +49 23 92 55-22 17
 EMail: vdm@thyssenkrupp.com
 www.thyssenkruppvdm.com

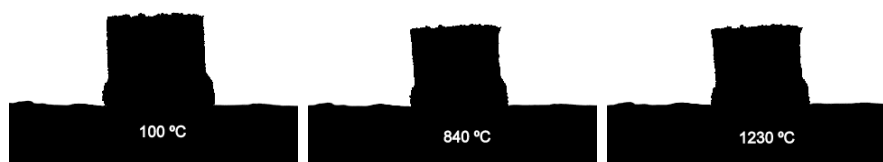
APPENDIX E

Results from hot-stage microscope measurements of compact glass powder on platinum support

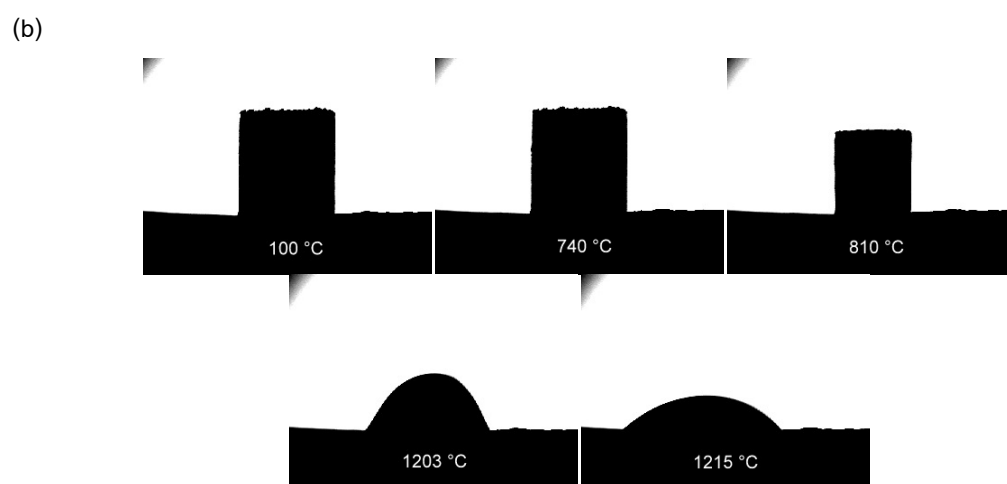
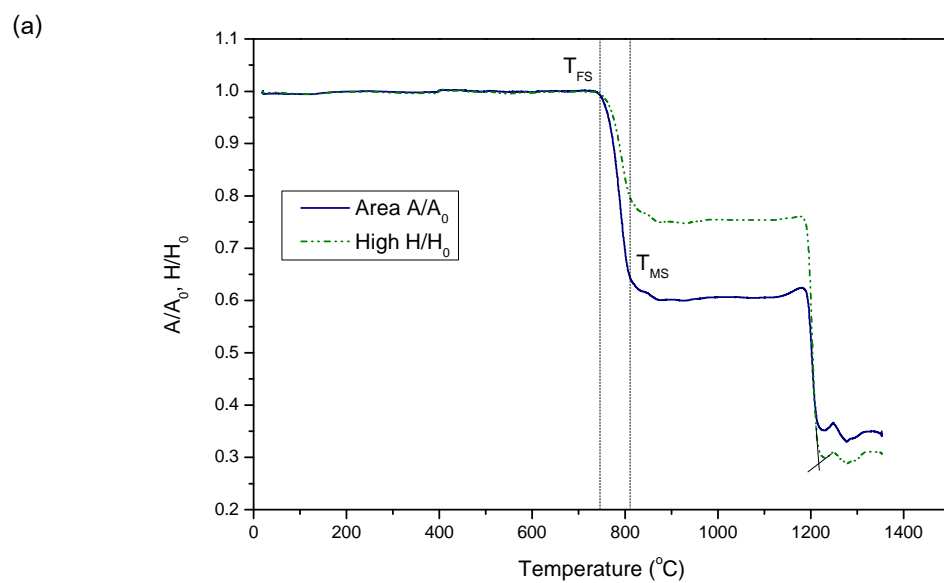
(a)



(b)

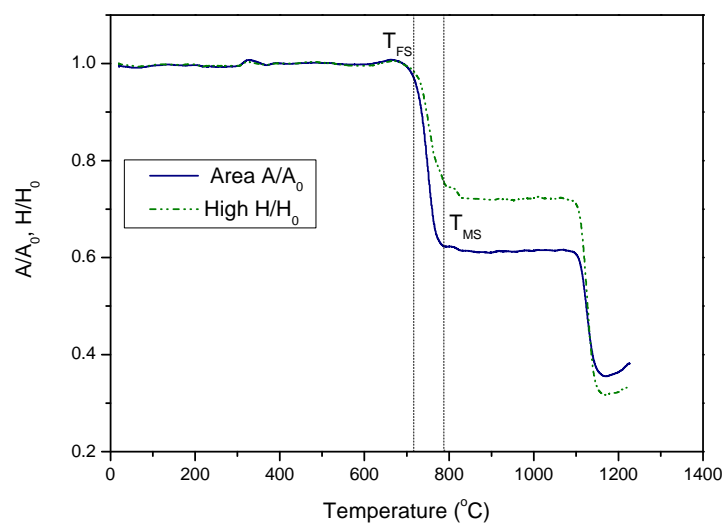


(a) Variation in area and height of powder sample of glass 34 during hot stage microscope measurement (b) Geometric shapes of the sample associated to (a)

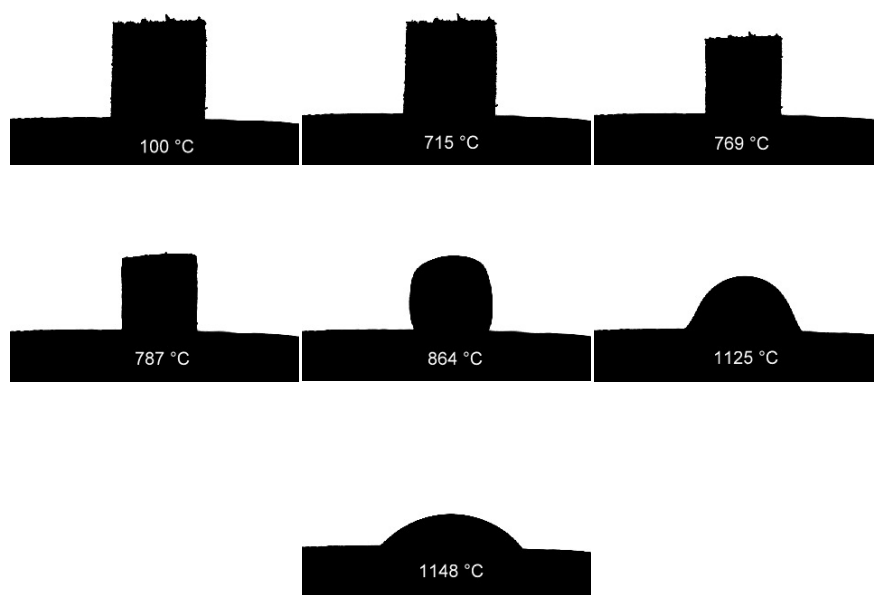


(a) Variation in area and height of powder sample of glass 34 – 5B during hot stage microscope measurement (b) Geometric shapes of the sample associated to (a)

(a)

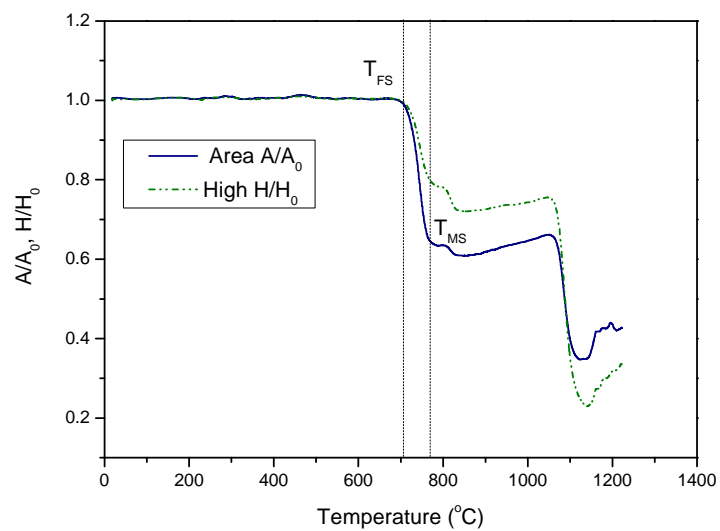


(b)

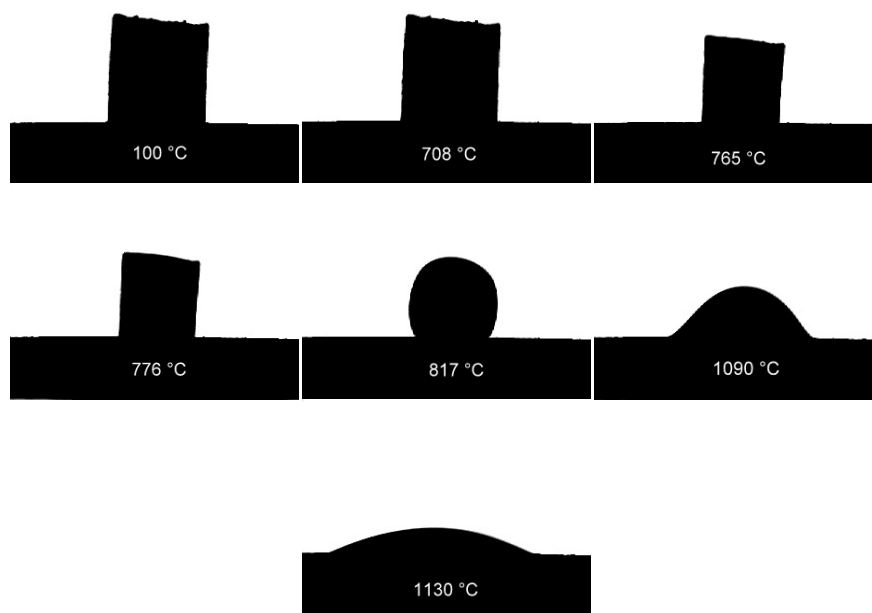


(a) Variation in area and height of powder sample of glass 34 – 10B during hot stage microscope measurement (b) Geometric shapes of the sample associated to (a)

(a)

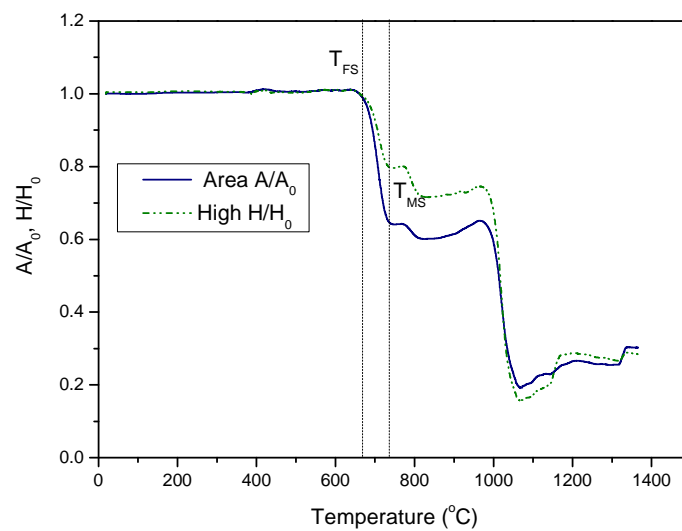


(b)

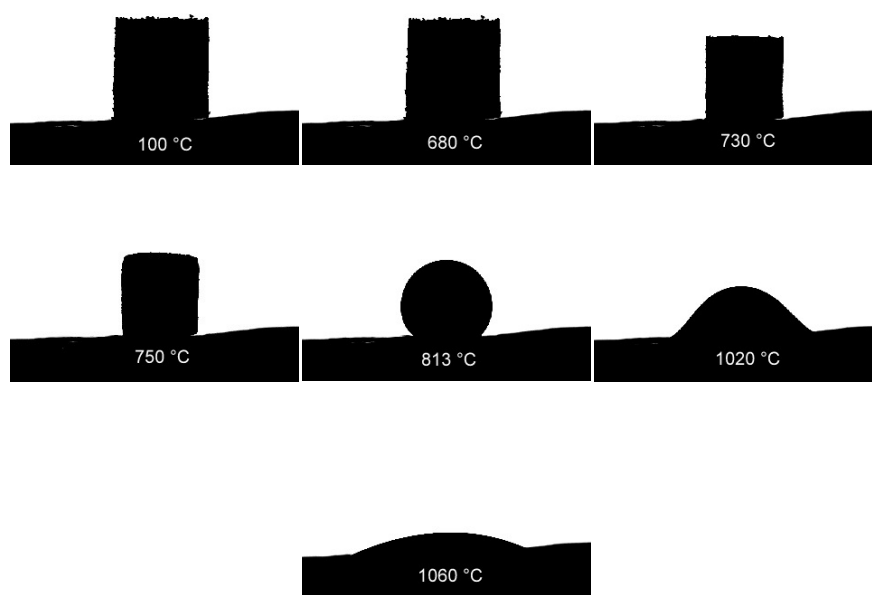


(a) Variation in area and height of powder sample of glass 34 – 15B during hot stage microscope measurement (b) Geometric shapes of the sample associated to (a)

(a)

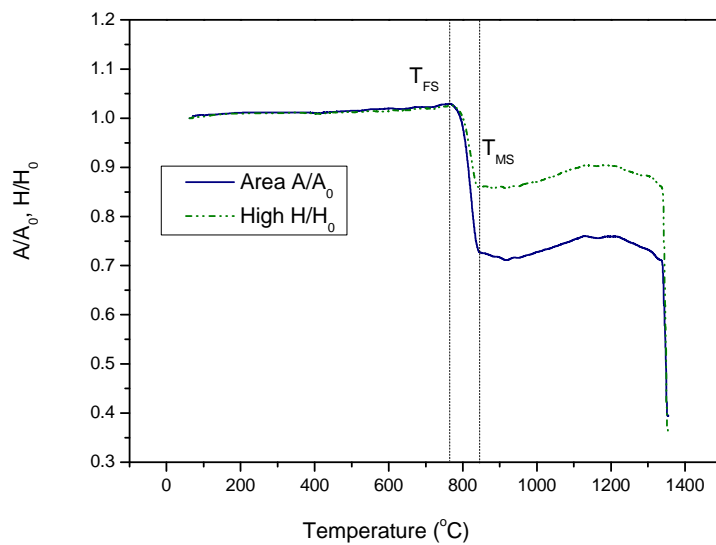


(b)

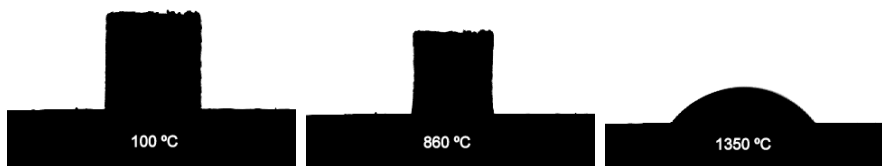


(a) Variation in area and height of powder sample of glass 34 – 20B during hot stage microscope measurement (b) Geometric shapes of the sample associated to (a)

(a)

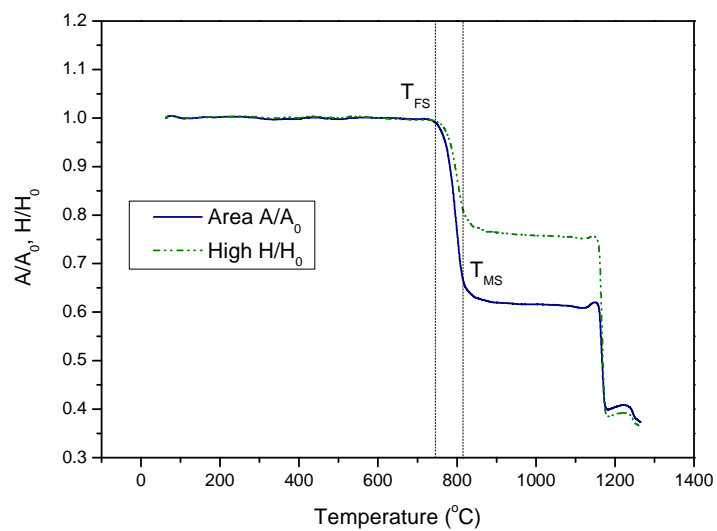


(b)

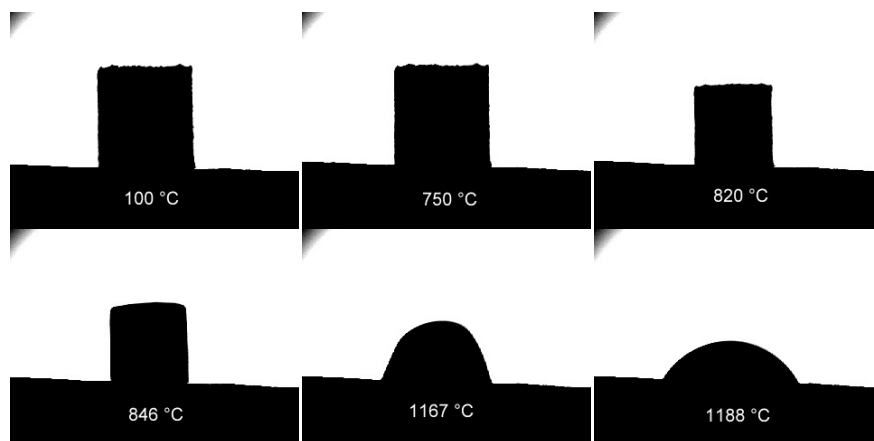


(a) Variation in area and height of powder sample of glass 35 during hot stage microscope measurement (b) Geometric shapes of the sample associated to (a)

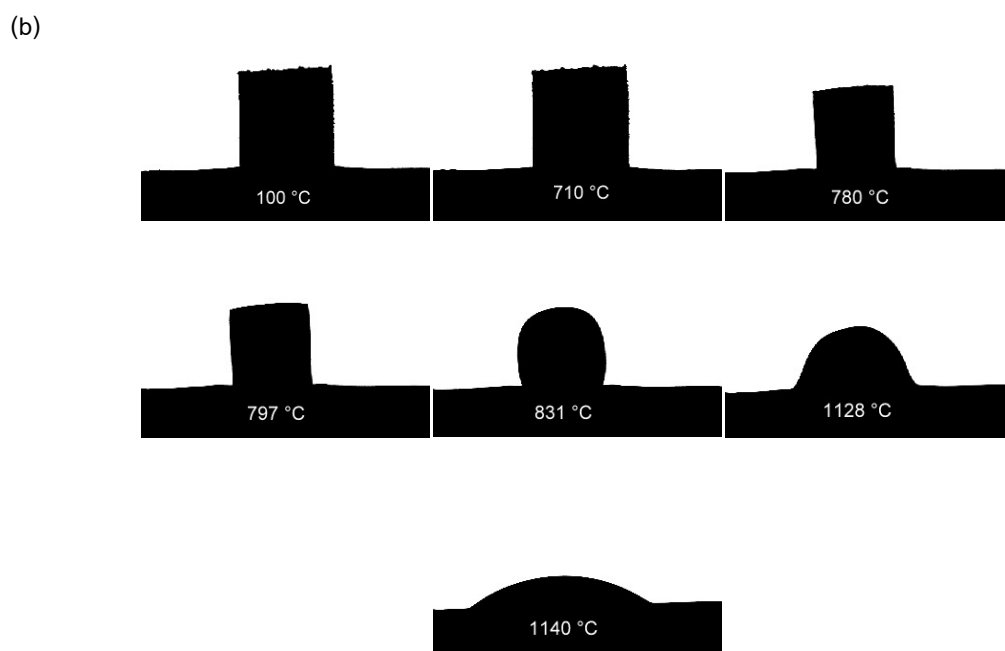
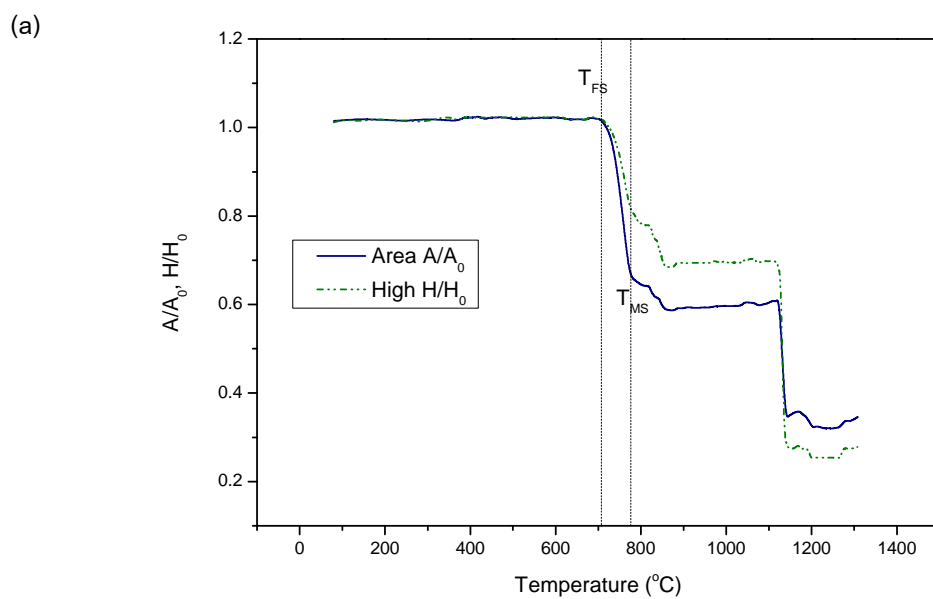
(a)



(b)

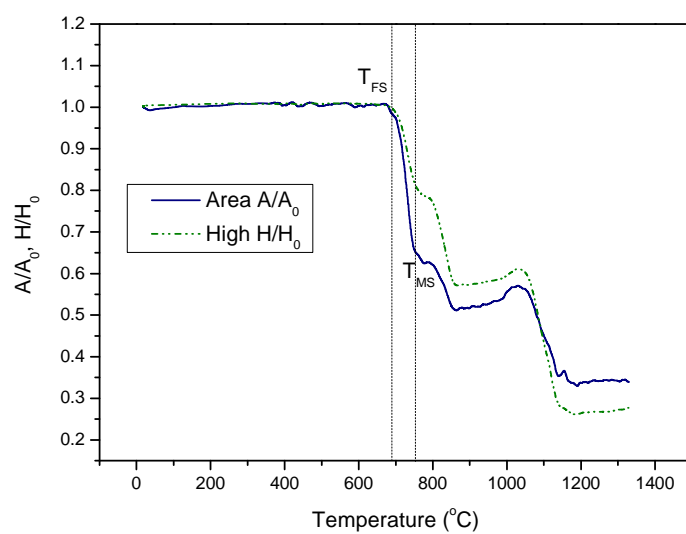


(a) Variation in area and height of powder sample of glass 35 – 5B during hot stage microscope measurement (b) Geometric shapes of the sample associated to (a)

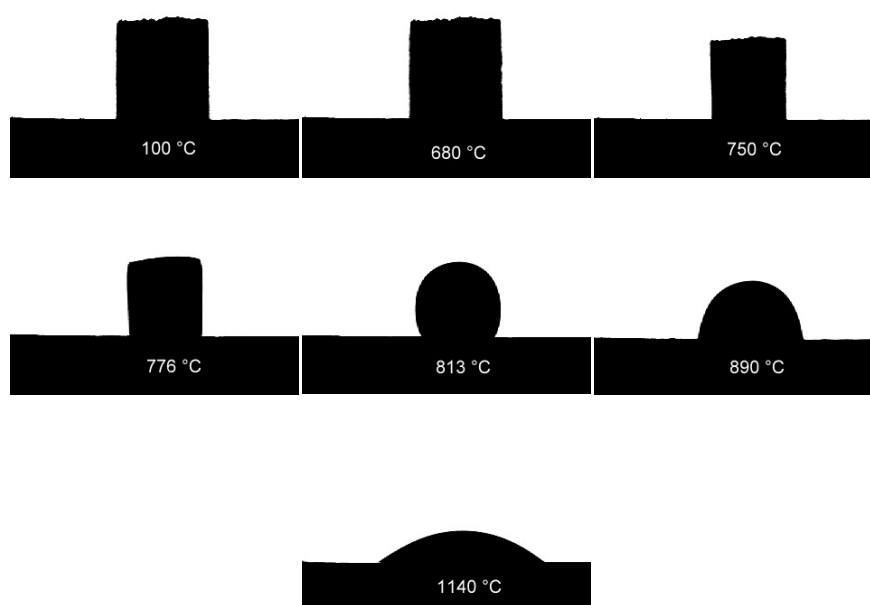


(a) Variation in area and height of powder sample of glass 35 – 10B during hot stage microscope measurement (b) Geometric shapes of the sample associated to (a)

(a)

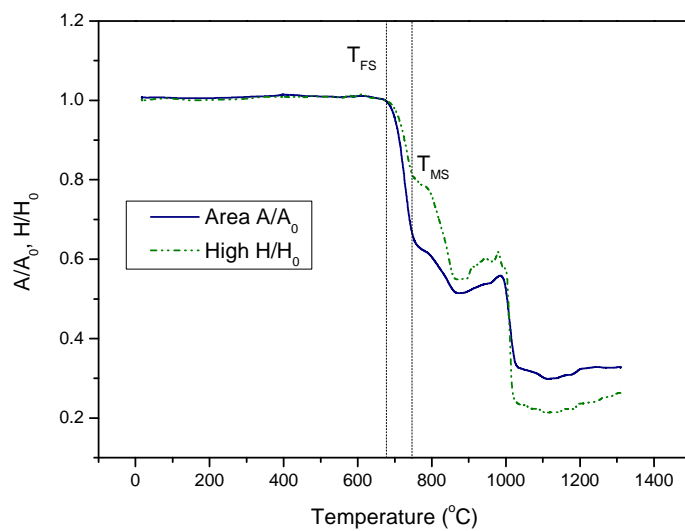


(b)

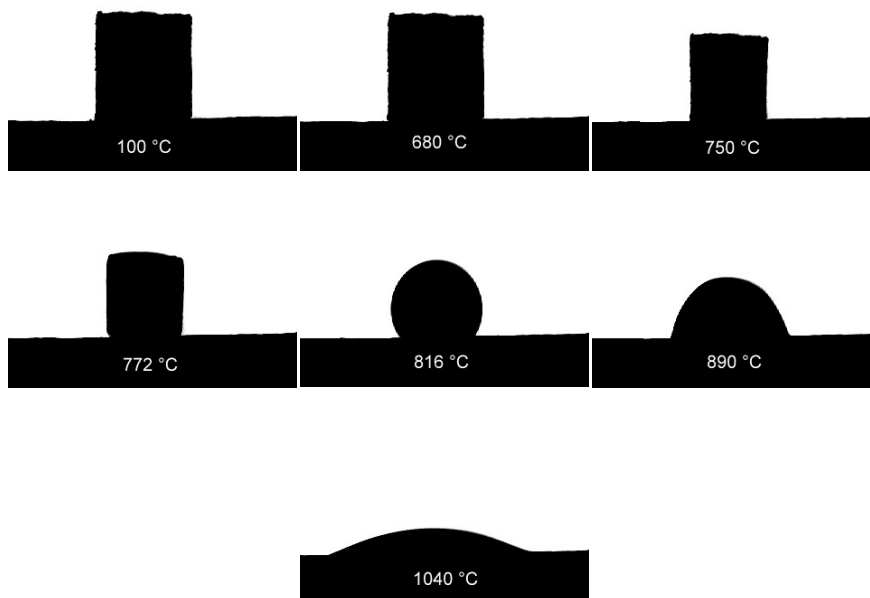


(a) Variation in area and height of powder sample of glass 35 – 15B during hot stage microscope measurement (b) Geometric shapes of the sample associated to (a)

(a)

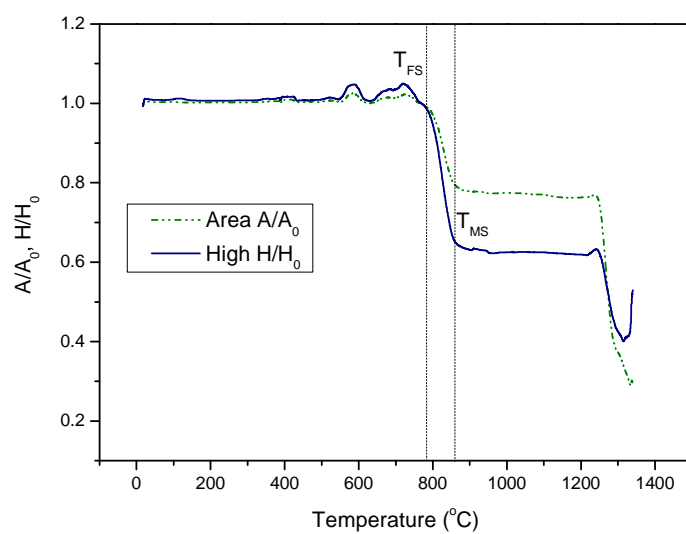


(b)

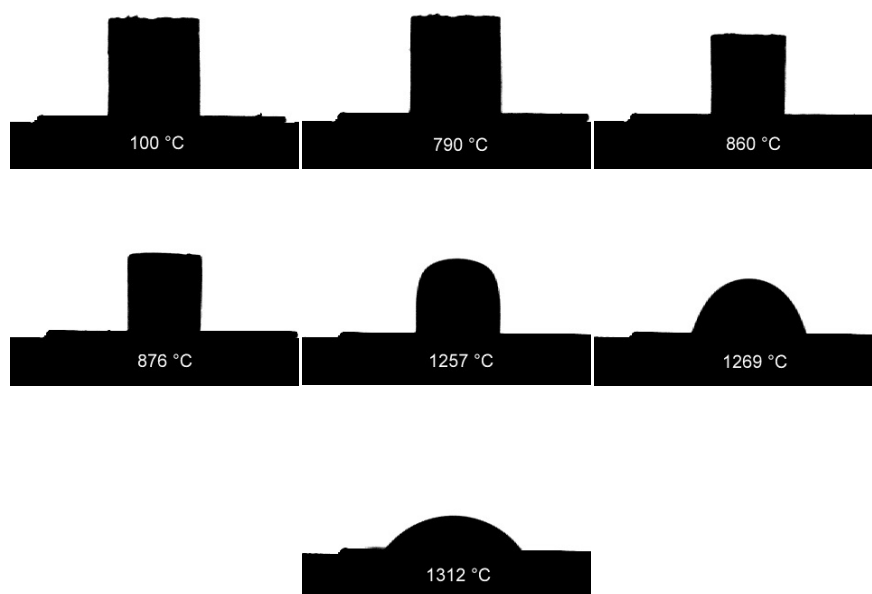


(a) Variation in area and height of powder sample of glass 35 – 20B during hot stage microscope measurement (b) Geometric shapes of the sample associated to (a)

(a)

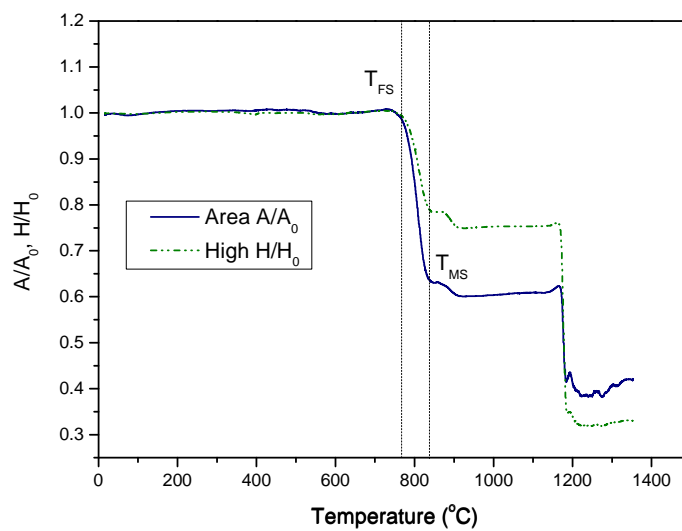


(b)

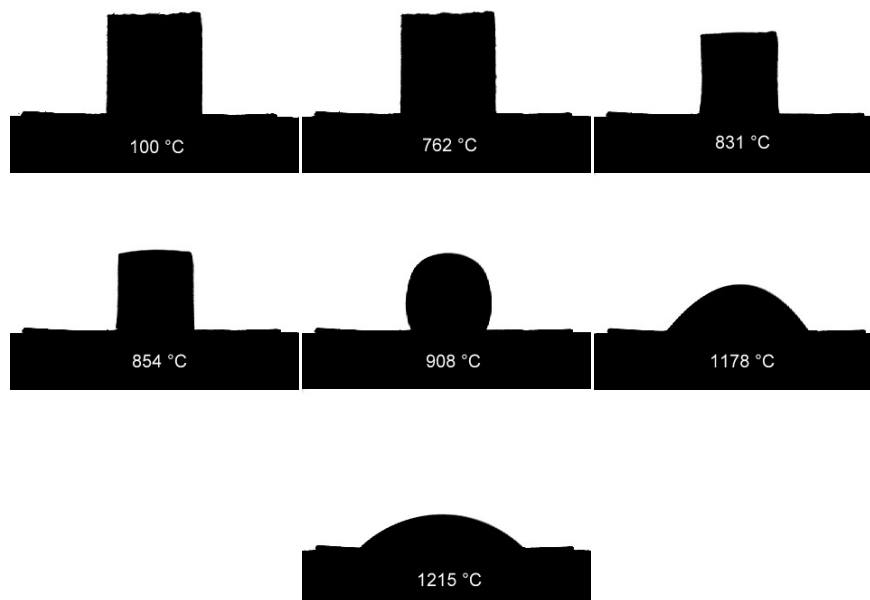


(a) Variation in area and height of powder sample of glass 37 during hot stage microscope measurement (b) Geometric shapes of the sample associated to (a)

(a)



(b)



(a) Variation in area and height of powder sample of glass 37 – 5B during hot stage microscope measurement (b) Geometric shapes of the sample associated to (a)

BIOGRAPHY

Mr. Apirat Theerapapvisetpong was born in Nan on May 4th, 1978. In 2001, he finished his Bachelor's Degree in Materials Science from the Department of Physics, Faculty of Science, Chiang Mai University. He started working as a scientist at the Department of Mineral Resources in the same year. Because of internal reorganization in 2003, his office name has been changed to the Department of Primary Industries and Mines. In 2003, he left to study for Master's Degree in the field of Ceramic Technology at Chulalongkorn University and graduated in 2006. Then, he continued his education at the same department and earned Ph.D. in Materials Science in 2011.

Publication paper

- **Theerapapvisetpong, A.**, Jiemsirilers, S., Thavorniti, P. and Conradt, R. Barium-Free Glass-Ceramic Sealants from the System CaO-MgO-B₂O₃-Al₂O₃-SiO₂ for Application in the SOFC. Materials Science Forum 695 (2011): 1-4.

Academic Conference presentations

- **Apirat Theerapapvisetpong**, Sirithan Jiemsirilers and Parjaree Thavorniti. Development of barium-free glass-ceramic seal for p-SOFC joining with AISI 430 stainless steel. The 8th Pacific Rim Conference on Ceramic and Glass Technology. Vancouver, Canada (May 31 - June 5, 2009).
- **Apirat Theerapapvisetpong**, Sirithan Jiemsirilers and Parjaree Thavorniti. Effect of alkali oxides on thermal properties of MgO-CaO-Al₂O₃-SiO₂ glass ceramic base for p-SOFC sealant application. International Symposium in Science and Technology at Kansai University 2009. Kansai University, Osaka, Japan (August 23-25, 2009).
- **Apirat Theerapapvisetpong**, Sirithan Jiemsirilers and Parjaree Thavorniti. Characterization of Na₂O - K₂O - CaO - MgO - Al₂O₃ - SiO₂ Glass Ceramic Sealants for Planar Solid Oxide Fuel Cells. Thailand, 35th Congress on Science and Technology of Thailand, Bangsan, Thailand (October 15–17, 2009).